Ministry of Higher Education and Scientific Research

Hassiba Benbouali University of Chlef

Faculty of Exact Sciences and computer science

Department of Chemistry

THESIS

Presented for obtaining the diploma of

DOCTORAT

Field: Chemistry

Specialty: Security, Reliability and Enhancement Of Gas Pipelines

By

BOUKORTT Hocine

Topic:

Influence of geometrical defects of the blades of turbine and pipelines: numerical study

---

Defended on / / , in front of the examining committee:

Mr. Khaled El-Miloudi	Pr. UHB-Chlef	President
Ms. Bailiche Zohra	MCA. UHB-Chlef	Examiner
Ms. Chahinez Fares	MCA. UHB-Chlef	Examiner
Ms. Razika Mehdaoui	MCA. Université de Blida	Examiner
Mr. Abdelmoumen Guedri	Pr. Universite de Souk Ahres	Examiner
M. Mustapha Allouti	Dr. Chef de dép. TRC, Sonatrach	Invited
M. Mohammed Hadj Meliani	Pr. Université HHB-Chlef	Supervisor
M. Ali khelil	Pr. Université HHB-Chlef	Co-supervisor

Scholar Year 2020-2021

Abstract

Withstanding of the gas turbine for the elongations is a major consideration in their design because they are subjected to high tangential, axial and centrifugal forces during their working conditions. Several authors have been suggested for the better enhancement of conception, thermal, mechanical and metallurgic properties of blades to withstand these extreme conditions. The damage severely of gas turbine due to the failure of blade, the observation showed that a serious pitting was occurred on the blade surfaces and there were evidences of fatigue marks in the fracture surface We also studied the corrosion of the gas pipe caused by the hydrogen from the high pressure of the turbine. The failure of the blade in a gas turbine was investigated a fracture mechanical study by a numerical analysis. In this study, we used a blade of a gas turbine, with a same shape, and we modified the crack size. In this analysis, the applied pressure is not constant, whereas is imported with an interaction between structure/fluid.

So, we used ANSYS® Workbench 16.0 software with the computational fluid dynamics Software (CFD section), a steady state gas flow analysis was carried out, and the pressure distributions. This pressure across the blade is obtained and we mapped these results on the other section of it APDL (ANSYS® Parametric Design Language) section. In the structural analysis a node coordinate where we have the maximum principal stresses were explored. In this node, we have created a semi-elliptical crack and we have compared between them with the Stress Intensity Factors and T-stress values. The second parameter in the Williams' equation give a good information’s on the estimation and the direction of the crack path in the part two we will study Hydrogen play a decisive role in many future energy systems. For these reasons, many researchers have been performed to see the effect of hydrogen on natural gas network.

Keywords: Blade, Integrity of structure, Hydrogen Embrittlement, Inconel 718 alloy, Gas Turbine, Crack failure, Interaction between Structure/Fluid(S-F), ANSYS®. Crack path Integrity of structure.

الملخص

إن تحمل التوربينات الغازية للاستطالة هو أحد الاعتبارات الرئيسية في تصميمها لأنها تتعرض لقوى مماسية ومحورية وطرد مركزي عالية خلال ظروف عملها. وقد اقترح العديد من المؤلفين لتحسين خصائص الحمل،حرارية والميكانيكية والمعدنية من الشفرات لتحمل هذه الظروف القاسية. الأضرار الشديدة من توربينات الغاز بسبب فشل شفرة، وأظهرت الملاحظة أن تأليب خطيرة وقعت على السطوح شفرة وكانت هناك أدلة على علامات التعب في سطح الكسر كما قمنا بدراسة تآكل انبوب الغاز الناجم عن مادة الهدروجين الآتية من جراء الضغط العالي للتوربين ،و اخذنا كمثال انبوبAPI 5L X52 . تم فحص فشل شفرة في توربينات الغاز دراسة ميكانيكية كسر من خلال التحليل العددي. في هذه الدراسة، استخدمنا شفرة من توربينات الغاز،

مع نفس الشكل، وقمنا بتعديل حجم الصدع. في هذا التحليل، الضغط المطبق ليس ثابتا، في حين يتم استيراده مع التفاعل بين هيكل السوائل. لذلك، استخدمنا ANSYS® workbench 16.0 البرمجيات مع ديناميات السوائل الحسابية البرمجيات (قسم CFD)، تم إجراء تحليل تدفق الغاز حالة مستقرة بها، وتوزيعات الضغط. يتم الحصول على هذا الضغط عبر شفرة وقمنا بتعيين هذه النتائج على القسم الآخر منه قسم APDL (أنسيستم باراميتريك لغة التصميم). في التحليل الهيكلي عقدة تنسيق حيث لدينا أقصى الضغوط الأساسية تم استكشافها. في هذه العقدة، أنشأنا الصدع شبه بيضاوي الشكل، ولقد قارنا بينها مع عوامل كثافة الإجهاد والقيم الإجهادT . المعامل الثاني في معادلة ويليامز يعطي معلومات جيدة عن تقدير واتجاه مسار صدع .في المرحلة الثانية يلعب الهيدروجين دورا حاسما في العديد من أنظمة الطاقة المستقبلية. لهذه الأسباب ، تم إجراء العديد من الباحثين لمعرفة تأثير الهيدروجين على شبكة الغاز الطبيعي..

كلمات البحث : شفرة، توربينات الغاز، سلامة الهيكل ، التقصف بالهيدروجين، فشل ، التفاعل بين هيكل/ السوائل- ، inconel 718 alloy .ANSYS® cfd

Acknowledgements

I would like to extend thanks to the many people, who so generously contributed to the work presented in this thesis.

The accomplishment of this thesis benefits of the help and direction from my dear supervisor— Prof. HADJ MELIANI is always happy and willing to help me solve the confusions and direct me approach to the final result of the thesis. On top of that, he is an easy-going and open-minded person. Without his encouragement, I want to thank all the jurors; I would not finish this final work in my doctorat study. Thank you very much.

Finally, but by no means least, thanks go to mum, dad, my family and prof.khlil ali for almost unbelievable support. They are the most important people in my world and I dedicate this thesis to them. Thank you.

BOUKORTT Hocine

UHBC

23/05/2019

Dedication to the spirit of my dear brother Fouad

Table of contents

Chapter III : Results and Discussions

List of Figures

CHAPTER I :

CHAPTER II : Computational Fluid Dynamics (CFD) and Structural Analysis

Chapter III : Results and Discussions

List of Tables

CHAPTER II : Computational Fluid Dynamics (CFD) and Structural Analysis

Chapter III : Results and Discussions

List of Abbreviations

a Notch length

a The crack length,

B The thickness of the specimen&

B The thickness of the body

E Young's modulus,

U_T Total energy

U_{strain} Strain energy

U_L The potential energy of the loading system,

U_E The strain energy of the body,

G The strain energy release rate,

G_c Critical strain energy value,

r Radial distance a head of the crack tipe

θ Angle defining position along the crack front of a surface crack

K Stress intensity factor

$K_{I, II, III}$ Stress intensity factor for Mode I, Mode II and Mode III

K_{IC} Fracture toughness for Mode I

K_t Stress concentration factor that the notch stress concentration factor

Keq The equivalent stress intensity factor

T T-stress (the 2nd parameter in Williams expansion)

P_{midd} the middling apply pressure

P Pressure

ρ The radius of curvature,

σ The applied stress,

σ_{ij}The stress tensor

σ_x,σ_y are normal stresses

σ_c The Griffith fracture stress

$\sigma_{\theta\theta}$ The circumferential (tangential) stress

σ_{rr} The radial stress

$\sigma_{r\theta}$ The shear stress

v Poisson's ratio

ε_x,ε_y normal strains

$\varepsilon_{\theta\theta}, \varepsilon_{rr}$ The normal strains

$\varepsilon_{r\theta}$ The shear strains

γ_s The surface energy associated with the creation of the crack faces

γ_p Plastic energy term

χ Measure of deformation

λ Scaling coefficient

f_{ij} Dimensionless function of θ in the leading term

τ_{xy}, τ_{yx} shear stresses

γ_{xy} shearing strain

u,v infinitesimal displacements

L linear differential operator

f (x) a function of x,

u_a , u_b the values of a function u(x) of interest at the endpoints,

e denotes the element number,

x_i the global coordinate of the nodal point,

N (e) i_e the value of the interpolation function at the nodal point i_e

1_e , 2_e the number of two nodal points of the eth element.

ξ the local coordinate of an arbitrary point in the eth element

h(e) the length of the e^{th} element

$w_i(x)$ weighting functions

$N_i(x)$ interpolation functions

Φ angle of front crack

T Second term of William's equation (T-stress)

Crack opening displacement (COD)

J J Integral

Contour integral

KIC Critical stress Intensity factor

GIC Critical elastic strain energy

JIC Critical J-integral

t Pipeline wall thichness

D External diameter of pipeline

P Applied pressure

MAOP Maximum allowable operating pressure

SMYS Minimum yield strength

fF Design factor

FE Joint factor

FT Temperature deration factor

XIV

Pf Failure pressure

d Crack depth in pipeline

M Bulging factor

Q Correction factor

L Defect length of pipeline

R Pipeline radius

Di Internal Diameter of pipeline

Kr Non dimensional crack driving force

Lr Non dimensional applied stress

PL Limit load

Effective crack length

fs Probability of failure

A Alongation at fracture

Kv Charpy energy

Reference fracture toughness

fs Safety factor

Q Spatially uniform hydrostatic stress

Inconel 718 alloy

Abbreviations

SIF Stress Intensity Factor

LEFM Linear Elastic Fracture Mechanics

FEM Finite Element Method

CAD Computer Aided Design

BC Boundary Conditions

APDL ANSYS® Parametric Design Language

CFD Computational Fluid Dynamics

CTOD Crack Tip Opening Displacement

HCF High Cycle Fatigue

LCF Low Cycle Fatigue

General Introduction

It is well known that, the oil and gas sector is the backbone of Algeria economy accounting for up to 85 per cent of total exports. According to the 2018 annual statistical bulletin of OPEC, the country's proven reserves are about 12,200 million barrels for crude oil and 4,500 billion cubic meters for natural gas. The crude oil production reached 1,039 million barrels/day and the marketed production of natural gas reached 94,778 billion cubic meters. The liquids and gaseous hydrocarbons transport network consists of a set of pipelines, pumping stations, compressor stations, storage yards, transporting effluents from production fields, a storage center or dispatching, to the industrial centers of processing and liquefaction, export and supply of the national industry. For that reason, the pipeline network is a vital link in the hydrocarbons chain. It ensures the transportation, for the benefit of the users, of all hydrocarbon production from upstream to downstream. It also feeds the domestic market, LNG and LPG separation complexes and crude oil and condensate refineries. The gas surplus is intended for export via GEM, GPDF and MEDGAZ and the surplus in crude oil and condensate is intended for export via the ports of Arzew, Bethioua, Béjaïa and Skikda [Soudani thesis].

Generally, this thesis examines the numerical and experimental investigations on gas turbine blades and pipeline defects according to the hydrogen of natural gas. It is divided into three chapters including the general introduction and general conclusion.

- In the first chapter, the literature review of gas turbine blade defects will be discussed. Based on the recent and previous researches, the accidents of turbine blades are briefly summarized and performed. A general information on the turbines are presented. In particular, it gives some basis on the main part of this project which is the blade of gas turbine. Consequently, the critical points of the blade defects are indicated to confirm our numerical study.
- The second chapter talks about the Computational Fluid Dynamics (CFD) and structural analysis. The governing equations of the fluid mechanics are demonstrated and presented in order to explain the boundary conditions of numerical analysis of Fluid-Structure Interaction (FSI).
- The last chapter is divided into two parts;

- First part is talking about the numerical study and software analysis of CFD which applied on the turbine blades. In this part, two types of numerical analysis are subjected. Extracting the pressure distributions by CFD software. In the other hand, the obtained results of CFD are transformed to the APDL data to perform the structural investigation using semi-elliptical cracks. In order to assess and evaluate the operating work of turbine blades, different methods and mathematical analysis of fracture mechanics are used. Stress intensity factor (SIF) and its equivalent are used on the crack distribution. In additional, Validation with the Wastergard equations are conducted to verify the SIFs. Volumetric method is considered an important to calculate T-stress on the blade. The results of the numerical software are demonstrated and are confused with the experimental investigation. A semi-elliptical crack with changing the crack's depth are created in the critical area. Results and discussions are conclude this part of this chapter.
- The second part is presenting the hydrogen embrittlement impact on pipeline steel. Due to the complexity of finding the same material of turbine blade steel (Inconel 718 ALLOY) which used in the station of natural gas, API X52 pipeline steel was used to investigate the experimental and numerical analysis of hydrogen embrittlement. API X52 steel is available in the Algerian industry and has the same characteristics of Inconel 718 ALLOY. For this reason, the hydrogen is one the component elements for natural gas. It is a serious problem for turbine blades which create the cracks in their structure. Different analysis such as optical microscopic, scanning electron SEM, tensile tests and fracture toughness are used to perform the experimental investigation. The second section of this part is presenting the numerical hydrogen embrittlement on the corroded pipeline. The assessment and integrity of pipeline is also presented using the limit pressure calculations. The conventional repair according to literature review are conclude this chapter because it is not available to complete this part in our university.

  Finally, this thesis is ended by general conclusions and perspectives.

CHAPITER I

Literature review of gas turbine blade defects

I.1 Introduction:

Almost all commercial electrical power on earth is generated with a turbine, driven either by wind, water, steam or burning gas. Turbine blades are subjected to very strenuous environments inside a gas turbine. They face high temperatures, high stresses, and a potentially high vibration environment. All these factors can lead to blade failure, resulting in catastrophic failure of turbine. In the event of turbine blade failure, turbine does not work and this leads to shutdown of power plant from one to four weeks or longer, depending on the extent of the damage and the procedure used to make the machine operational again, which results in economic loss and service to mankind also stops. For each day of a forced outage, a utility could lose hundreds of thousands of dollars in electrical power.

The external and internal surface damages include corrosion, oxidation, crack formation, erosion, foreign object damage and fretting. The internal damage of microstructure include γ' phase, CoNi3 [(Al, Ti)] phase aging (rafting), grain growth, brittle phases formation, carbides precipitation, creep and grain boundary void formation. These damages produce dimensional change which results in increase in operational stress that leads to deterioration in turbine efficiency. The deterioration of blade material is related to the high gas temperature, high steady state load levels (centrifugal load) and high thermal transient load (trips, start-ups, start downs).

I.2 Types of gas turbine and main Uses

Gas turbines are divided into two groups on the basis of design differences although there is now some convergence in design; these include:

- ✓ **Aeroderivative gas turbine**: It is a turbine derived from aircraft engines, lightweight, simplified in form, low fuel consumption and high levels of reliability but its cost is relatively high [5].This turbine use not gas as fuel source. Actually, they are designed so that fuel and air are mixed and then ignited to achieve the desired output [2]. This turbine requires high quality fuel and is experiencing a drop in power and efficiency after a relatively long period of operation
- ✓ **Industrial gas turbine**: It is a turbine of robust construction for stationary use and continuous operation. It is less effective than aerodynamics, but generally maintains its

performance over a longer period of operation. Its maintenance can easily be carried out on site [3].

The gas turbine has many applications by their specific definition parameters: fuel type, operating hours per year, outdoor temperatures extremes, mounting, nuisances, etc, to get the operational condition they must customized the installation. There are three principal main uses:

- ✓ **Electricity production**

This application is extremely common: the turbine shaft drives a gearbox whose low speed shaft drives an alternator. The mechanical system is simple and can be compared to a steam turbo-generator group. Only producing electricity with a gas turbine is interesting that for operating conditions imposing this system. For these two cases, we will indicate the favorable and Unfavorable to the gas turbine compared to the diesel group

- ✓ **Combined heat-force production**

Combined heat-force production based on the basic combined cycle that's consists of two machines gas turbine and the other is steam turbine .This application allow as to save petroleum and their products more then that the energy**.**

- ✓ **Pumping and compression**

In this case we replace the alternator by pump, by compressor or a blower. On the type of our machine we can chose between single or two-shaft turbine [4].

I.3 Principles of operation

As the principle of the gas turbine, a working gas (air) is compressed by a compressor and heated by combustion energy of the fuel at the first. The working gas becomes the high temperature and high pressure. The engine converts the energy of working gas into the rotating energy of the blades, making use of the interaction between the gas and blades [5].

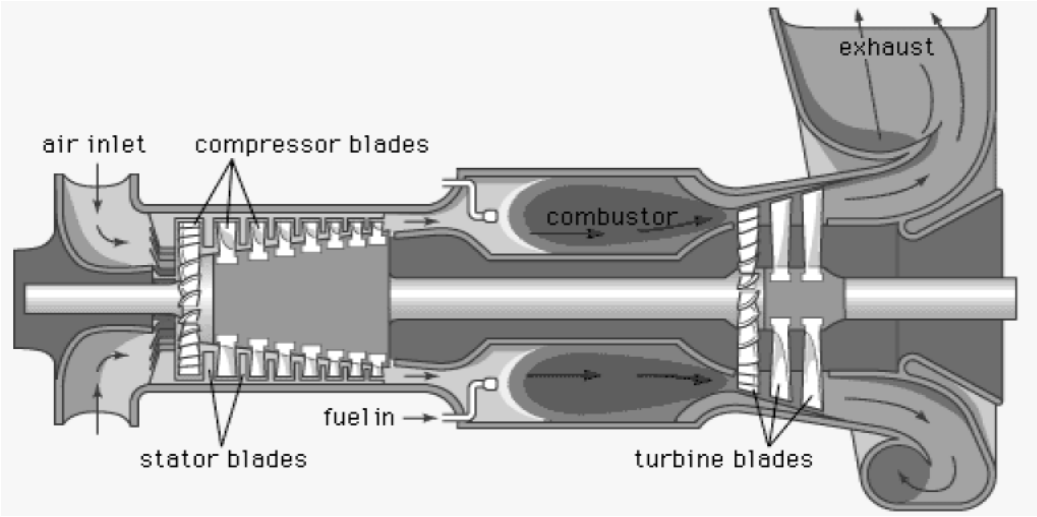

Figure.I.1. Operation of gas turbines [3].

The Brayton cycle is a thermodynamic process that allow to converts the chemical energy to mechanical energy in the gas turbine presses (Fig.I.1 and I.2)

- ✓ Compression: the entered air has been compressed without any thermal transfer between the system studied and the external environment by the axial compressor to 1 to 7 bars.
- ✓ Combustion: the pressure stays constant, the fuel and the compressed air will mix and make a mixture that ignited and causing rapid expansion of the hot gases.
- ✓ Expansion: There is no thermal transfer between the system studied and the external environment, the expand hot gases in the turbine will Causing a rotating torque in the process.
- ✓ Exhaust: With constant the pressure the Burned gases will evacuated to the atmosphere after having almost all their energy to the section [5].

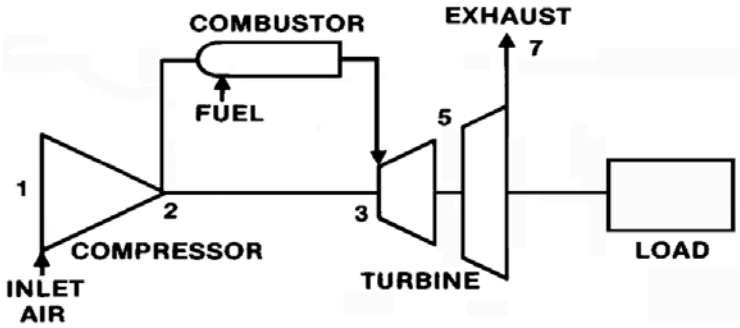

Figure.I.2. gas turbine diagram [6].

I.4 Gas Turbine Components

The gas turbine identified in three major components, compressor, combustor and turbine (Fig.I.3). The shaft turn when the turbine provide the driving power to it that as well turn the compressor in this case we can say the shaft connect between the turbine and the compressor.

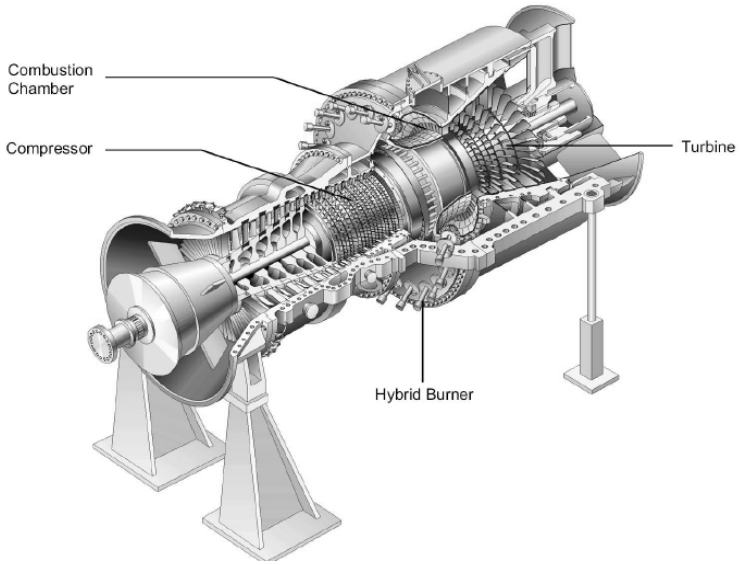

Figure.I.3.gas turbine sections [7].

- Compressor: is machine for compressing a fluid (compressible) at a desired pressure.
- Combustion chamber: Is an enclosure which is resistant to sudden changes in pressure and temperature, that's come from expansion. And combustor architecture, make it achieve the maximum efficiency while maintaining the highest reliability.
- Turbine: Is a rotary device for using the kinetic energy of a liquid fluid such as water or gas (vapor, air, combustion gas) to rotate a shaft supporting the blades of the turbine
- Exhaust: is the phase of the cycle where the heat transfer fluid is released into the atmosphere [8].

I.5. Turbine

The turbine depends for its operation on the transfer of energy on the impacts with the blades that's rotate the wheel of turbine that provide a driving power for the shaft and the compressor at the high speed and produce (Fig.I.4).

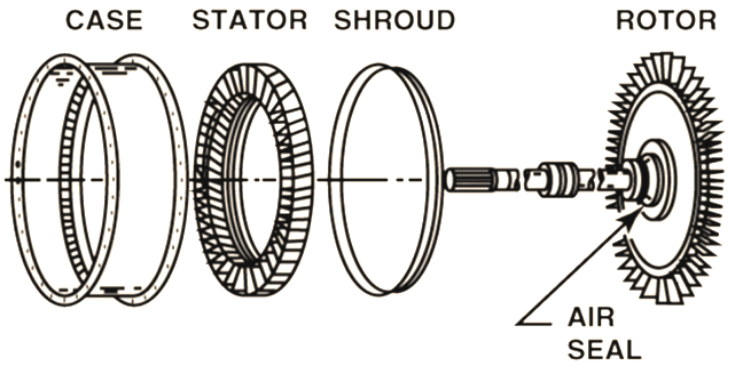

Figure.I.4.description of the turbine parts [9]

Like any machinery the turbines have four main components that are we can define below:

- ✓ **Turbine casing**

The casing contains the blades and controls the working fluid. Can reduces stress risers to minimize joint maintenance issues. The barrel design uniformly controls thermal expansion, permitting rapid load changes and a structural supports the rotating elements [10].

- ✓ **Turbine stator**

Stators, are fixed and do not rotate. The job of the stators is to keep the flow from spiraling around the axis by bringing the flow back parallel to the axis and direct the energy that produced form the combustors to impact with the turbine rotor at the right angle.

- ✓ **Turbine shroud**

The shrouds have important role it serve to seal against tip leakage and dampen vibration and improve blade tip sealing characteristics blades incorporating tip shrouds to dampen vibration and improve blade tip sealing characteristics . The turbine shrouds' secondary function is to provide a high thermal resistance between the hot gases and the comparatively cool shell

- ✓ **Turbine rotor**

The rotors are connected to the central shaft and rotate at high speed and it's a device consisting of blades attached to a rotating disk; this blade will be rotated to produce energy after the expansion of the mixture (Fig.I.4). And there is many engines use multiple turbine stages to absorb sufficient energy to drive the compressor [1].

I.6. Blades

Turbine blade design was, and still is a function of the performance match between the turbine and the compressor, in a gas turbine engine; a single turbine section is made of a disk or hub that holds many turbine blades. The blades are responsible for extracting energy from the high temperature, high pressure gas produced by the combustor. Turbine blades are subject to stresses resulting from high temperatures, high centrifugal forces, and thermal cycling. These stresses accelerate the growth of defects. That's make turbine blades are the parts which undergo the most damaging solicitations.

The turbine blade is the rotating component within the turbine which presents many challenges to the design and manufacturing communities. This component leads the way in terms of future technology. Below are some of the key technologies to be implemented on to the turbine blade.

The turbine blades composed form the body of the blade are fixed with platform (Fig.I.5.a), it seen that the nozzle guide vanes and blades of the turbine are 'twisted' that twist shape makes the gas flow from combustion system equal the work at all positions along the length of the blade and ensure that's the exhaust gases have uniform axial velocity. The blades have a stagger angle which is greater at the tip than the root like that's showed in Fig.I.5.b. [12]

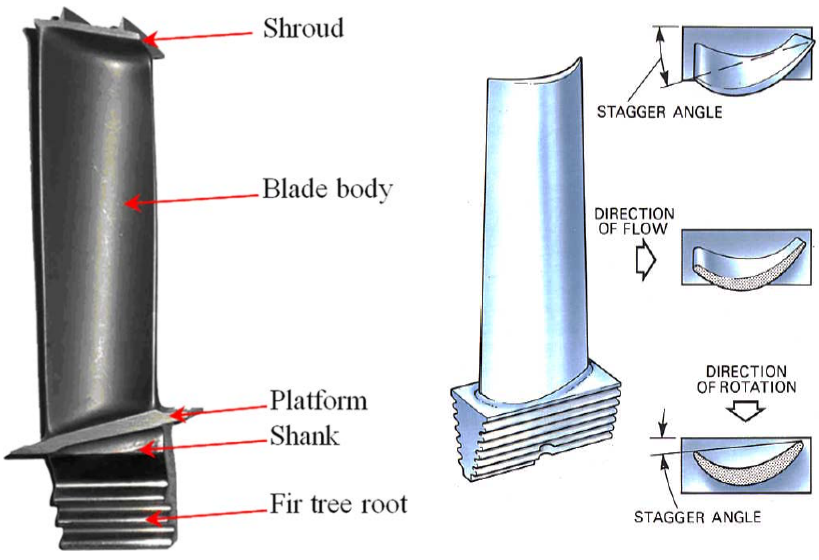

(a) (b)

Figure.I.5. blade shape and section: (a) blade parts, (b) blade stagger angle [11, 12].

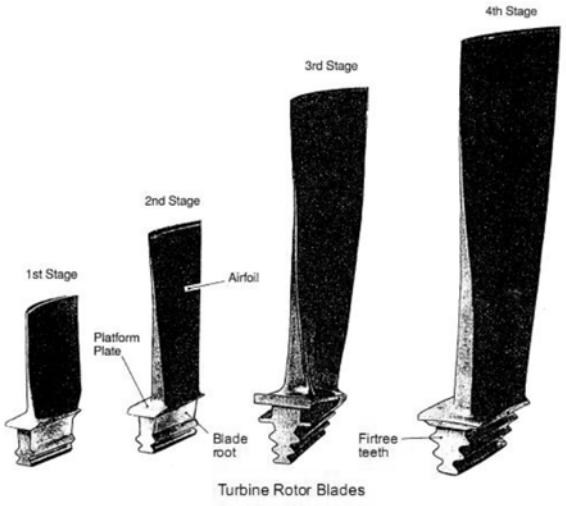

Figure**.I.6.** Turbine blade structure from the first stage to fourth stage [7].

To determine the stage in gas turbine we must know the two types of blades one fixed and the other mobile. And the number of stages has effects on the blade structure and design (Fig.II.9).

I.6.1. Gas turbine blade manufacturing process

Competitive manufacturing blades for steam and gas turbines is challenging with machining containing most of the demanding factors in metal cutting:

- Part materials have varying machinability (some of them poor, needing dedicated inserts),
- Considerable amounts of material have to be removed and good surface finish has to be achieved (without affecting the blade negatively, for example in terms of residual stress),
- Component form is complex (some needing advanced CAM-programs with the best methods),
- Blades are prone to vibration during machining (long, slender, thin parts that need light-cutting tools and dampening abilities),
- Production efficiency is important (large volumes are made),
- Several different tools have to be used and applied correctly (straightforward face milling to 4- to 5-axis profiling).[13].

I.6.1.1 Milling of turbine blades

Turbine blade manufacturing is a varied field from engine compressor and turbo-pumps, rotors and stators of large steam and gas turbines, to the world of blades and vanes. Many of these precision, high temp alloy part designs require milling machine (5-axis machining) and also advanced cutting tool designs to be successfully manufactured.

Because the blades of the turbines are milled with a precision of the order of hundredth of a millimeter. This operation is for the machining of mechanical attachment features and the milling of special blade geometries and provides many automation for simple machining definition and incredibly short programming times.

- ✓ **3D arbitrary stock roughing**

On the basis of a freely-definable stock, the turbine blades are ma - chined from various directions. The strategy automatically prevents redundant movements during undercuts.

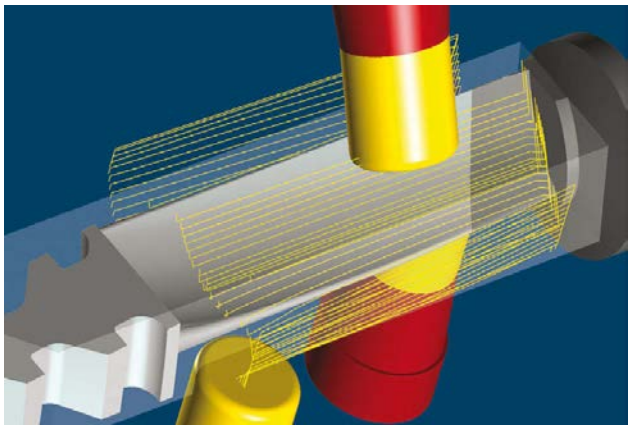

Figure**.I.7.** Rough blank any 3D[14]

Constant cutting depths and a feedrate independent of the rotary axes guarantee constant cutting conditions. Clamping of the rotary axes enables the use of larger tools and leads to a high stock removal rate. [14]

- ✓ **5axis blade top milling**

In this cycle, top milling is used for the finishing of blade surfaces. It is pos - sible to generate spiral tool paths either as 5axis or 4axis simultane - ous machinings.

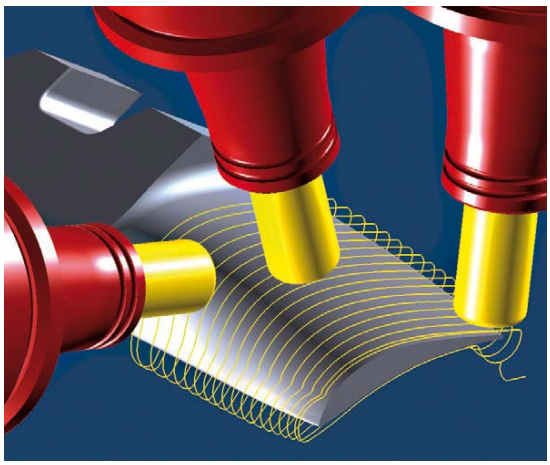

Figure**.I.8.** Turbine blade end machining 5 axes[17]

With end mills and bull nose end mills, the lead angle is always automatically corrected to prevent surfaces from being damaged and to make sure the tools are always cutting on the front edge. [14]

- ✓ **5axis blade swarf cutting**

With 5axis flank machining, it is possible to machine the transition between the blade and side surfaces that cannot be milled using 5axis top milling.

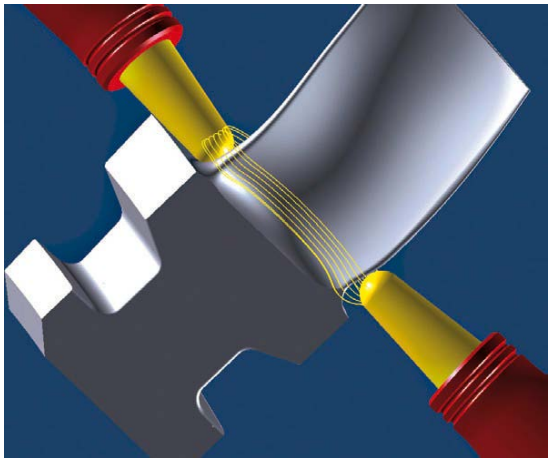

Figure.I.9. Rolling milling of turbine blades5 axes[14]

Lead and side slope angles ensure optimal cutting conditions. In addition, 5axis flank machining makes it possible to create slightly curved side surfaces quickly using swarf cutting[14]

- ✓ **5axis blade fillet milling**

This function optimizes the finishing along the intersection between a blade and the side surfaces from the shroud and the hub. The crossfade paths to the blade machining ensure very high quality surfaces. [14]

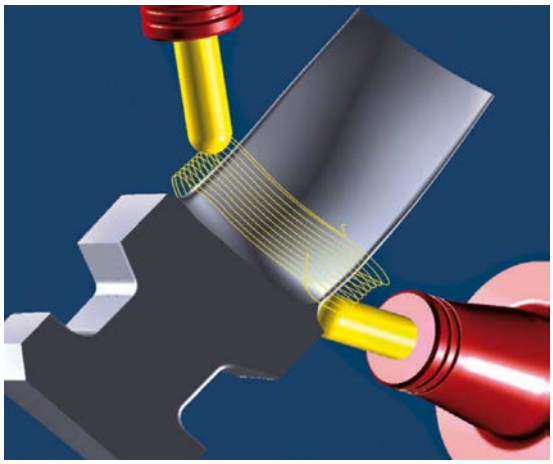

Figure.I.10. Machining of the 5-axis blade root fitting[14]

As an option, a “rolling ball” radius can be generated automatically. The tool simultaneously maintains contact with the blade and the optimally smoothed boundary to the side surface. In this way, a perfect transition is achieved, also with regard to the neighboring blades. In many other CAD systems this type of machining cannot be configured

- ✓ **Additional strategies for the ma - chining of mechanical attachment features**

A series of 2D and 3D strategies are available for machining the base of the blade. The 2D strategies include drilling, face milling, curve and pocket milling. Roughing cycles.

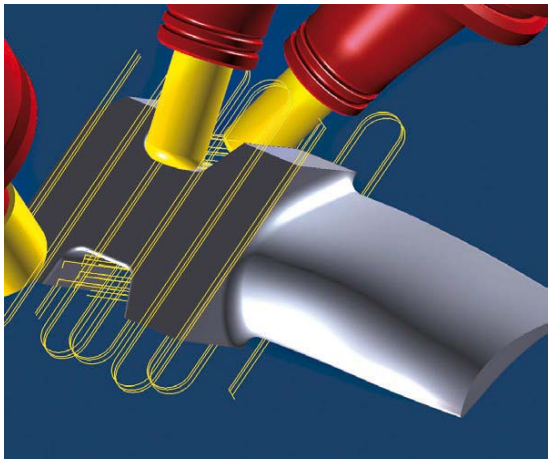

Figure.I.11. Additional strategies for the machining of the foot [14]

Finishing operations for base geometry and strategies for trimming, deburring or the sharpening of curved surfaces are included in the 3D operations. [14].

I.7. Gas turbine blade failure

The process of gas turbine operation is associated with various failures to structural components of gas turbines, Analysis of the literature and own experience show that only a small portion of damages/failures to turbine vanes and blades are caused by material defects, structural and/or engineering process attributable defects; most damages/failures are service attributable (Fig.I.12) [15].

During the service, gas turbine components may be subject to failures resulting from the following processes [16]:

- ✓ Low-cycle and high-cycle fatigue due to thermal and thermo-mechanical factors,
- ✓ Corrosion and fatigue cracking
- ✓ Overheating and melting;
- ✓ Monotonic cracks (Creeping);

- ✓ Chemical and intercrystalline corrosion;
- ✓ Erosion;
- ✓ Other factors of less importance

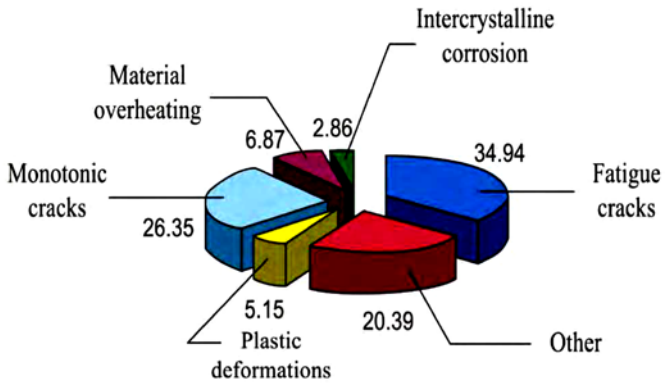

Figure.I.12. Causes of failures gas turbine engines during service [15].

I.8. State of the art:

Salehnasab et al. [1 7] have presented the mechanism and modeling of fatigue crack initiation and propagation in CM186 LC directional solidified material of afirst-stage gas turbine blade. To investigate the crack initiation point, afinite element study was carried out using ABAQUS software package. The stress distribution of the blade was calculated in accordance with engine conditions and the fatigue crack growth was then predicted by using ZENCRACK fracture mechanics code. Moreover, the Paris model was used in this study to estimate the fatigue life. The stress intensity factors (KI & KII) of individual mode and fracture mechanics quantities were calculated from CTOD and JIntegral methods, followed by the computation of crack growth direction on the basis of maximum energy release rate criterion.

Jiaxi Xia et al [18]Have work of the system optimization of ORC by means of genetic algorithm is conducted for different mixtures to obtain the optimal mixture working fluid and initial design parameters of turbine. The thermal design of the mixture ORC radial inflow turbine is carried out, and the CFD simulation is performed to investigate the threedimensional flow characteristic of the designed turbine. Meanwhile, the helical groove seal of the turbine shaft is designed and analyzed through CFD method. Results show that the mixture ORC radial inflow turbine is well designed with an isentropic

efficiency of 83.71%, and CFD results basically match with the thermal design results. What's more, the CFD simulation result for the differential pressure of the helical groove seal has an only −5.83% deviation compared with the designed one, and the helical groove seal is well designed with desirable sealing performance.

Rani et al [19] Have Studied evaluation of tip crack at the trailing edge and further degradation of blade coating. The investigations included the visual observations, material composition analysis, scanning electron microscopy (SEM)and energy dispersive spectroscopy (EDS).During examination of the failed blade, it is found that the blade surface is completely degraded due to overheating. Corrosion pits are formed on the blade surface, these pits act as a notch to produce stress concentrations and cracks is initiated due to fatigue which further propagate due to hot corrosion. It is also reported that the Al-Pt coating iscompletely degraded, heavily oxidized. From these investigations, it is concluded that the failure of gas turbine blade takes place due to the combined effect of surface degradation caused by overheating, oxidation, hot corrosion and degradation of coating heavily oxidized(fig I.13)

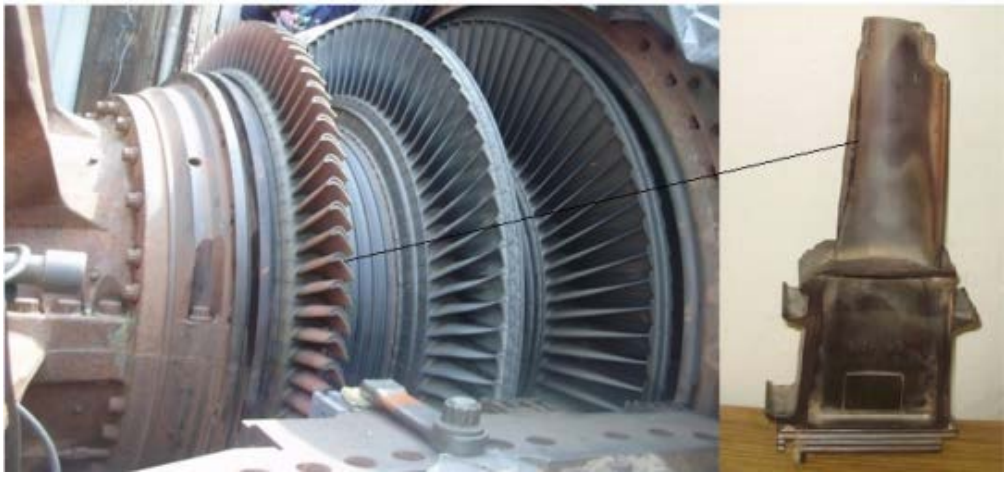

Figure.I.13.(1) Internal view of 30 MW Gas Turbine. (2) First stage Gas Turbine Blade.

Swain et al [20] investigates afirst stage turbine blade failure in a 6.5 MW gas turbine. The blade is made of nickel-based superalloy,and the failure occurred in the airfoils after 6500 h of operation. Several examinations were carried out in order to identify potential failure reasons such as: visual examination, fractography and microstructural characterization used by optical and scanning electron microscopes (SEM) and energy dispersive X-ray (EDX). The precipitated phases morphology (carbides andγ′(Ni3Al)) changed in the airfoil for exampleγ′ resolved and re-deposited in addition to decomposition of carbides.

Furthermore, the fracture surface exhibits the local melting occurred and re-solidified in the leading edge. From analysis and experimental results of this study, overheating is shown to be the main reason of blade failure(fig I.14).

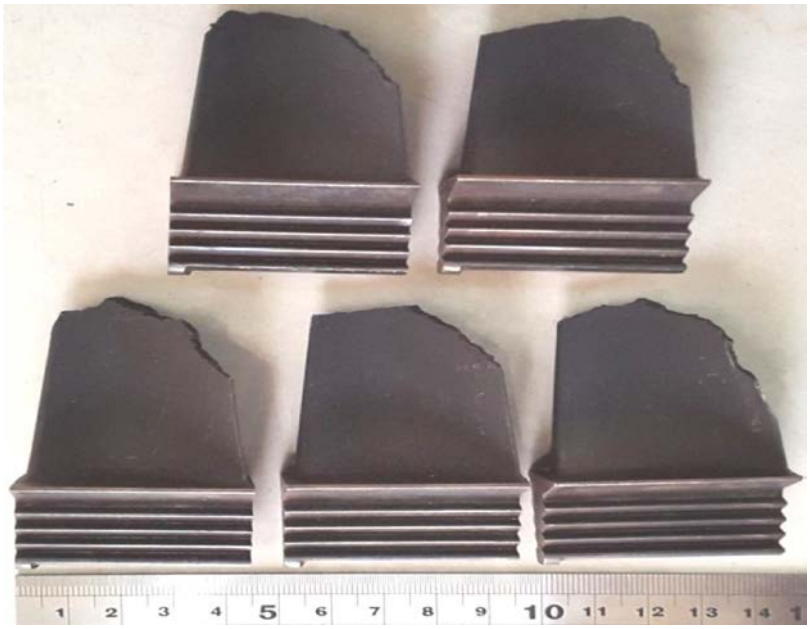

Figure.I.14. Damaged rotor blades of first-stage turbine blades after 6500 h of operation at about 750–800 °C a 6.5 MW gas turbine.

Naga et al [21] investigated of High pressure temperature (HPT) turbine blade is the most important component of the gas turbine and failures in this turbine blade can have dramatic effect on the safety and performance of the gas turbine engine. This paper presents the failure analysis made on HPT turbine blades of 100 MW gas turbine used in marine applications. The gas turbine blade was made of Nickel based super alloys and was manufactured by investment casting method. The gas turbine blade under examination was operated at elevated temperatures in corrosive environmental attack such as oxidation, hot corrosion and sulphidation etc. The investigation on gas turbine blade included the activities like visual inspection, determination of material composition, microscopic examination and metallurgical analysis. Metallurgical examination reveals that there was no micro-structuraldamage due to blade operation at elevated temperatures. It indicates that the gas turbine was operated within the designed temperature conditions. It was observed that the blade might have suffered both corrosion (including HTHC & LTHC) and erosion. LTHC was prominent at the root of the blade while the regions near the tip of the blade were affected by the HTHC. It could be concluded that the turbine blade failure might be caused by multiple failure mechanisms such as hot corrosion, erosion and fatigue. Hot

corrosion could have reduced the thickness of the blade material and thus weakened the blade. This reduction of the blade thickness decreases the fatigue strength which ultimately led to the failure of the turbine blade(fig I.15).

Figure I.15 HPT Gas turbine blade

Aust et al [22] investigate to The maintenance of aero engines is intricate, time-consuming, costly and has significant functional and safety implications. Engine blades and vanes are the most rejected parts during engine maintenance. Consequently, there is an ongoing need for more effective and efficient inspection processes. Purpos defines engine blade defects, assigns root-causes, shows causal links and cascade effects and provides a taxonomy system. Approach Defect types were identified from the literature and maintenance manuals, categorisations were devised and an ontology was created. Results Defect was categorised into Surface Damage, Wear, Material Separation and Material Deformation. A second categorisation identified potential causes of Impact, Environmental causes, Operational causes, Poor maintenance, Poor manufacturing and Fatigue.These two categorisations were integrated with an ontology. Originality The work provides a single comprehensive illustrated list of engine blade defects, and a standardised defect terminology, which currently does not exist in the aviation industry. It proposes a taxonomy for both engine blade defects and root-causes, and shows that these may be related using an ontology.

Carrick et al [23]Presented experience with blade failures on two turbines at ICI's Wilton factory. The history of the failures, the results of investigations into the causes, and the measures adopted to prevent further repetitions are given. Some comments are made about blade failures in general:

This plant had a 10MW steam turbine driving a recycle gas compressor. The machine was commissioned in late 1979.In April 1982 after about 16,000 hours operation on rotor no. 2 the machine suddenly stopped . It was concluded that the vibration following the blade failure had been so violent that it caused the turbine mechanical overspeed trip to operate.

In 1983 after about 15,000 hours operation, turbine rotor no. 1 (the original spare) was removed from service and the 4th stage blades removed for examination. A number of blades were found to be cracked, but this time in different locations in the packets . One of these cracks was over 75% through the critical root section of the blade (see figure 5). Once again the cracks were caused by fatigue. Obviously we had been very lucky to avoid another failure in service.

In Oct 1984 after about 12,000 hours operation the first modified (Mk2) rotor experienced a blade failure, of the single (unique) closing blade. No other cracks were found. This rotor had operated at significantly higher speed and load than either of the Mk1 rotors. The blade manufacturer's consultant suggested that the failure was due to vibration in the 1st tangential out of phase mode. However it was subsequently discovered that there were also some manufacturing anomalies with this blade (the serrated teeth had been re-machined during manufacture).

MAZUR et al [24] investigated toThe first typical failure mechanism occurs when the blade develops coating degradation (Figure I.16), this happens mostly because of the high operating temperatures of the gas turbine. The second stage of failure is when the base alloy gets degraded, and in this stage blades are usually hard to repair and in most times must be replaced.

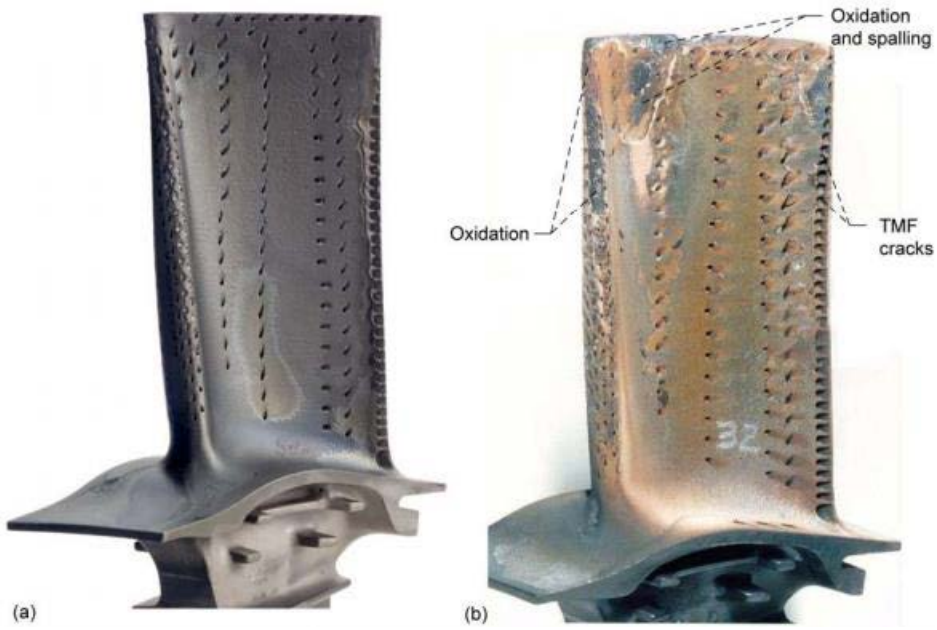

Figure I.16. Comparison of unfailed (a) and failed (b) T-1 turbine blades [16]

Kaung et al [25] stadied An optimal design is found in three design iterations. The optimization history graphs for objective,selected constraints, and design variables are shown in fig(I.17), respectively. The history graphs show that the objective function starts from 15,300 mm3 and reduces to 14,500 mm3 at the firstdesign iteration. During last two iterations, the objective function converges to an optimum criteriondefined in the DOT. Note that at the initial design (infeasible), objective function reduction is possiblebecause the design search direction that corrects the constraint violation (stress at element 171) also

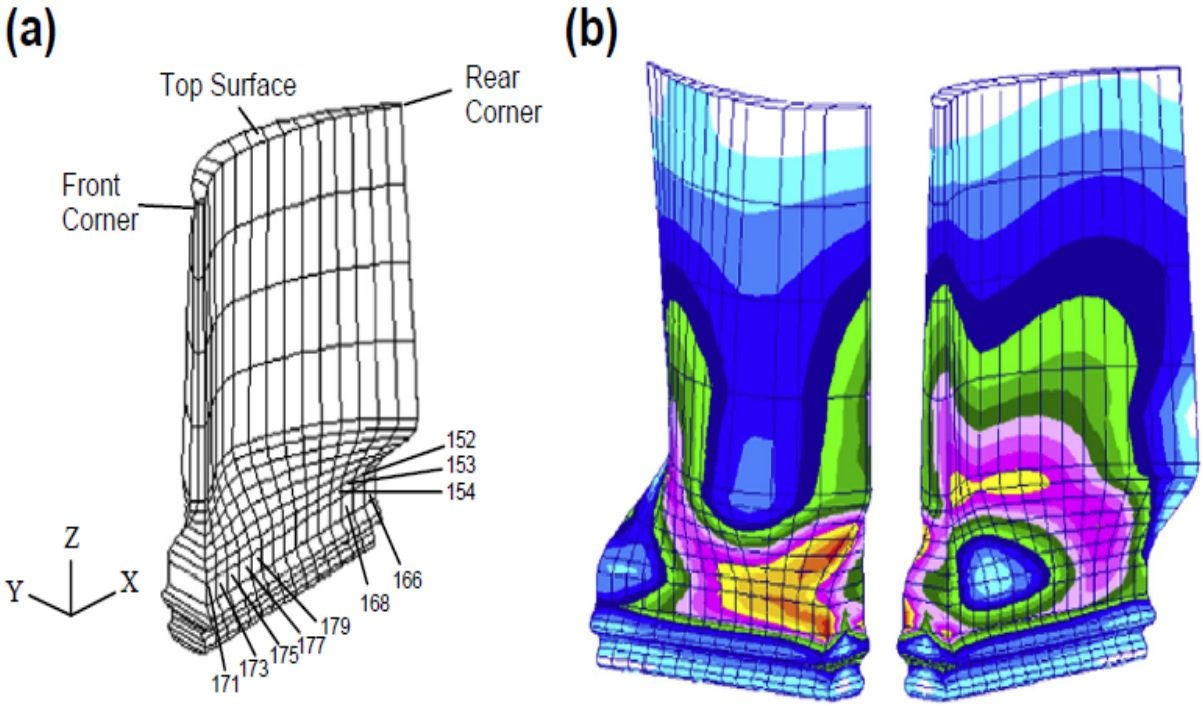

Figure .I.17- Turbine blade model: (a) finite element mesh with elements of high stresses and (b) stress fringe plots.

Dewangan et al [26] investigated of the failure analysis of first and second stage turbine blade,where in the First Stage 90% of the first stage blades were damaged(fig I.18).

Most of the damages are on the tip of the leading edge and also, bulk separation is obvious in this region. There are some signs of Foreign Objects Damage (FOD) on top of the leading edge and convex side (suction side) of the airfoil. Figure 1 shows the general view of the first stage blade. Similar conditions were observed in other stages.

Figure I.18: The General View of the First Stage Blade

A damaged turbine blade which was retrieved from the accident site is shown in Figure. The

firtree joint is also separately presented in the above mentioned figure. The remaining

portion of the main fractured turbine lade under investigation which only includes the firtree root region, due to complete separation of the airfoil section of the blade in the fracture process, is shown in Figure(I.19).

Figure I.19.Blade Geometry and the Firtree Joint of a Damaged Turbine Blade

Rani et al [27] worked of A case study is presented in order to detect failure mode and locate cracks on a 30 MW first stage gas turbine blade made of nickel based super alloy IN738LC, which has failed after rendering a useful life of 72000 h. The root causes of failure are detected by comparing the failed blade experimental model with the failed blade computational model. It is observed that the frequencies of the real failed blade experimental model are lesser than the computational model of the failed turbine blade. This is due to the metallurgical defects, which result in loosening of stiffness at the leading and trailing edges of the blade. Further, the stress concentration areas noticed on leading and trailing edges in computational model of the failed blade at the sixth mode are well corroborated with the cracked zone seen on leading and trailing edges of a real case failed turbine blade, collected from the site. It is concluded that the blade has failed due to that the resonance at sixth modal frequency. Scanning electron microscope (SEM) images reveal the presence of corrosion pits on the surfaces of the turbine blade that lead to surface degradation, which results in crack initiation and its propagation with high-cycle fatigue. It is concluded that the failure of turbine blade occurs due to high cycle fatigue(fig I.20).

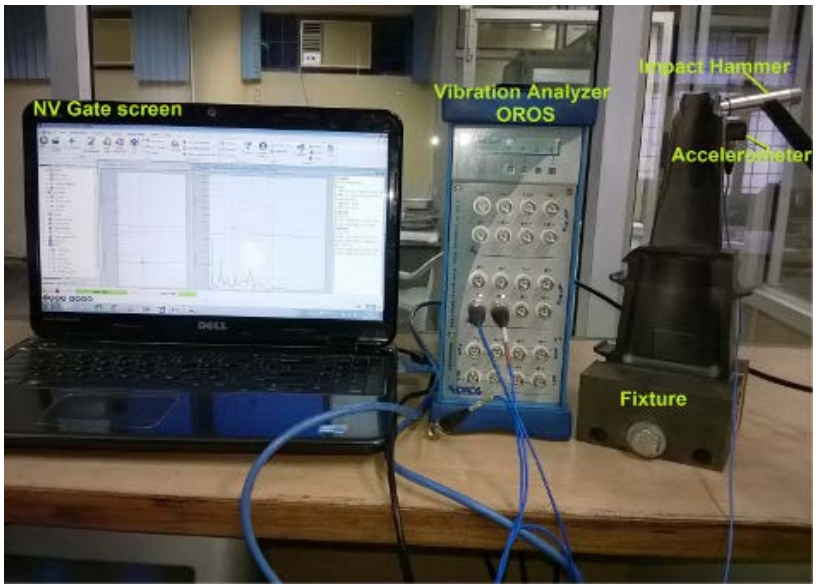

Figure I.20.Experimental modal analysis of failed gas turbine blade.

Yoon et al [28] analysed the failure of the gas turbines of a cogeneration plant is analyzed by focusing mainly on the crack initiation mechanism of blade fracture. Damage of several blades of the compressor was observed after a gas turbine was disassembled, and the root causes of the damage were investigated in detail by scanning electron microscopy as well as optical microscopy. The defects observed at the crack initiation site have been

characterized by comparison with previous studies. The fracture of the blade was supposed to be initiated by a crack due to concentrated stresses around a preexisting defect which was possibly formed before the turbine was operated, e.g., a forging defect during the three-step forging process for blades manufacture(fig I.21).

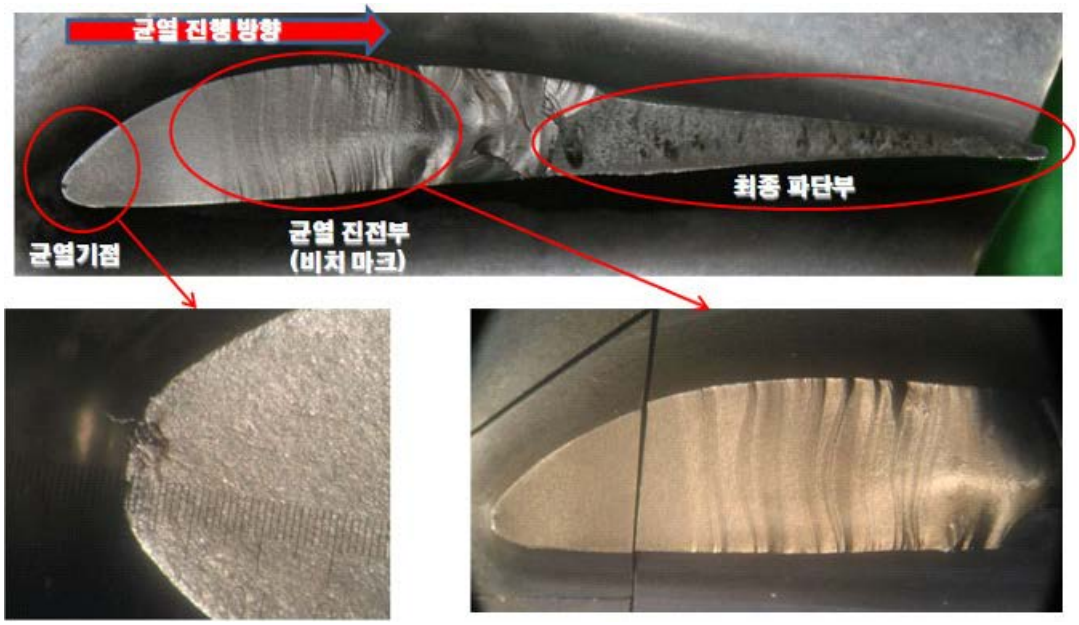

Figure I.21. Observation of the fractured blade

FRIJA et al [29] presented finite elements modeling of aerofoil-shaped Ti-6Al-4V leading edge specimens fig (I.22). The behavior of the subjected material is supposed to be elasto-viscous-plastic coupled with damage using the Johnson Cook law with his shear failure model. The model was used to predict the residual stress profiles in agreement with the experimental investigations. The results of the simulations have also predicted profiles of plastic strain, as well as levels of surface damage and surface roughness. This is a great advantage for better prediction of polycyclic fatigue life.

we can assess the rate of improvement or deterioration in the fatigue life induced by the LSP treatment (fig I.23).

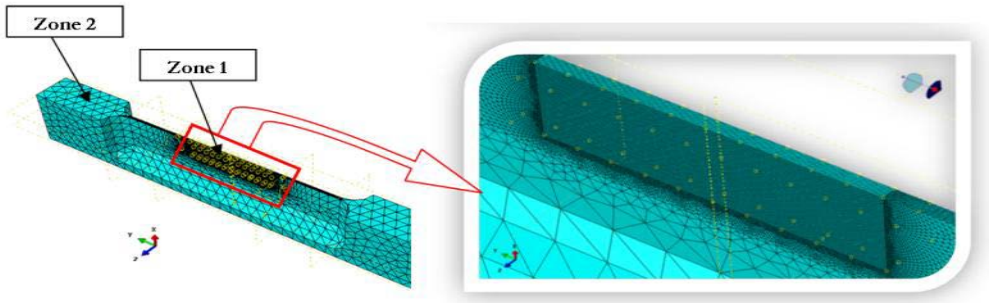

Figure I.22. Dimensional specifications of the test piece representative of the turbine blade

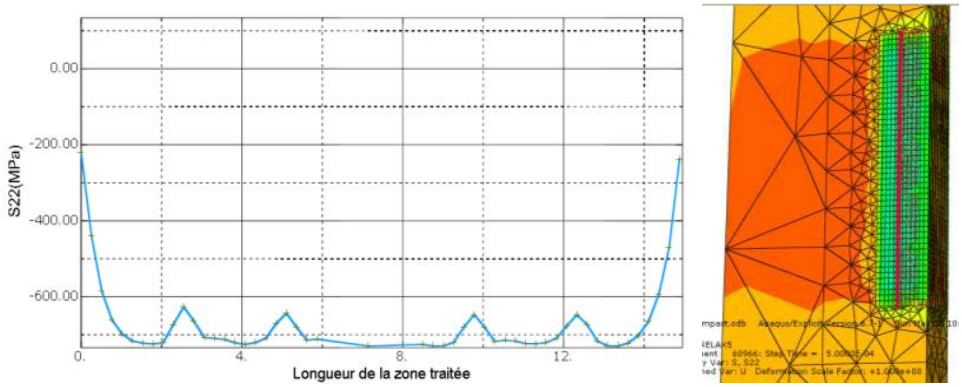

Figure I.23. Profile of residual stresses on the surface of the blade following the treatment of the leading edges

Krasovs'kyi et al. [30] study the causes of the service fracture of turbine rotor blade of compressor station gas-turbine unit, comprehensive structural and fracto-graphic investigations of the service fracture (Fig.II.16) of a rotor blade of the second stage of the GTK-10-2 gas-turbine unit LPT of a compressor station have been carried out to ascertain the cause of its fracture.

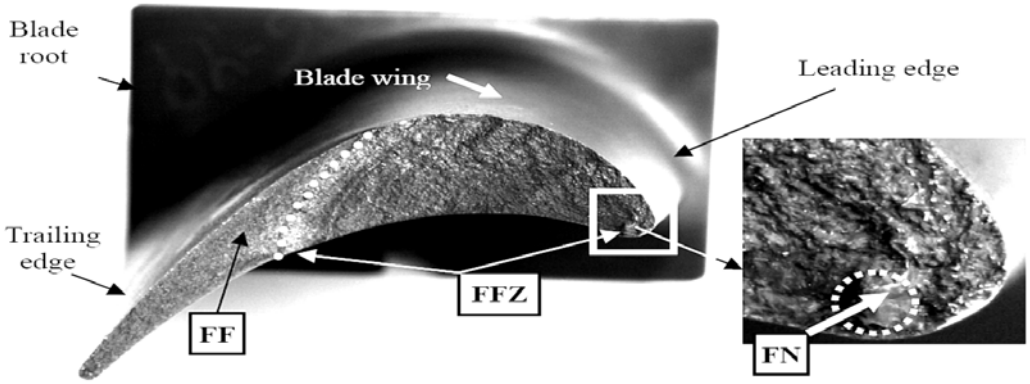

Figure.I.24. A part of the service fracture of the blade wing of the second stage of a low-pressure turbine rotor (FN=fracture nucleus, FFZ=fatigue fracture zone, and FF=final fracture) [30].

A.sadikouhanjani et al. [31] has study the failure investigation of a blade in a heavy duty land-base gas turbine, The objective of this work is to determine the root cause of the blade failure, has found that there is three distinct regions denoted by I, II, and III in Fig.II.17 can be identified at the fracture surface.

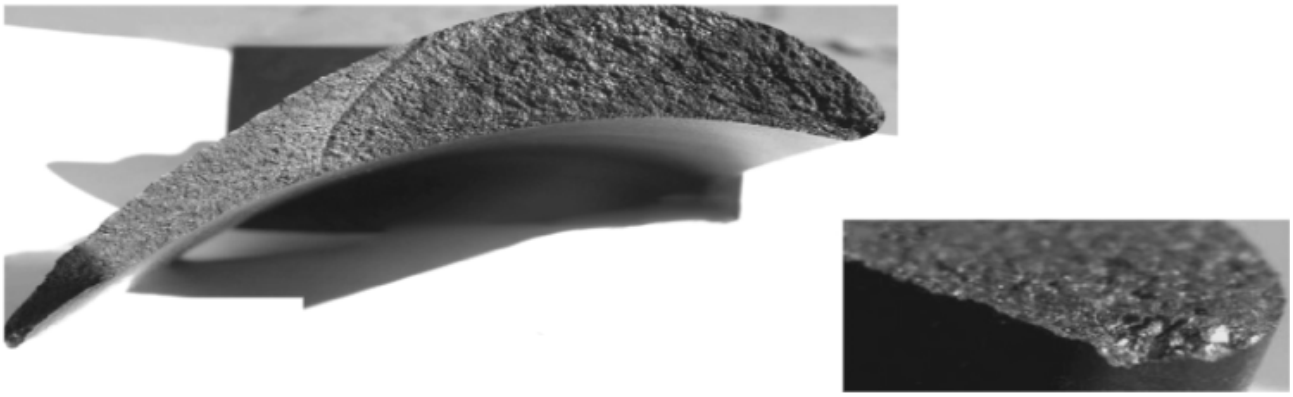

Figure**.I.25.** General view of the fracture surface of the three regions [31].

Fig.I.25 showed no visible crack is observed, but a cave-in area is formed linearly (~800μm in length) with a partially exposed inclusion. There is no visible evidence of corrosion [32].

I.9. Critical position of gas turbine blade :

Several studies confirm our results of the simulation on the maximum stress caused by the pressure and the foreign bodies which pass with the gas and here is some research in this direction :

Jiaxi Et al [33] worked of the system optimization of ORC by means of genetic algorithm is conducted for different mixtures to obtain the optimal mixture working fluid and initial design parameters of turbine. The thermal design of the mixture ORC radial inflow turbine is carried out, and the CFD simulation is performed to investigate the threedimensional flow characteristic of the designed turbine. Meanwhile, the helical groove seal of the turbine shaft is designed and analyzed through CFD method. Results show that the mixture ORC radial inflow turbine is well designed with an isentropic efficiency of 83.71%, and CFD results basically match with the thermal design results. What's more, the CFD simulation result for the differential pressure of the helical groove seal has an only −5.83% deviation compared with the designed one, and the helical groove seal is well designed with desirable sealing performance(fig I.26).

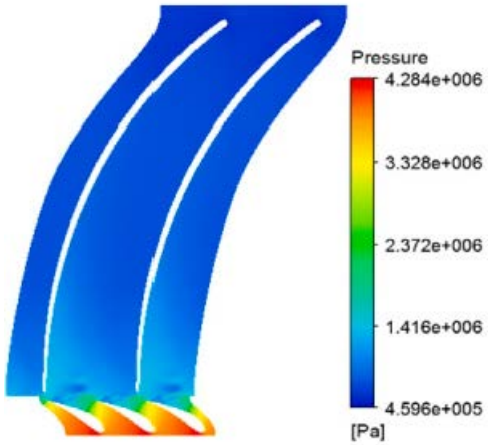

Figure I.26 .Pressure in the blade turbine

Wan et al[34] statied The fracture of the blade was supposed to be started by a crack due to concentrated stresses around a preexisting defect.fig(I.28)

Figure I.27.defect found in the row 5 blades

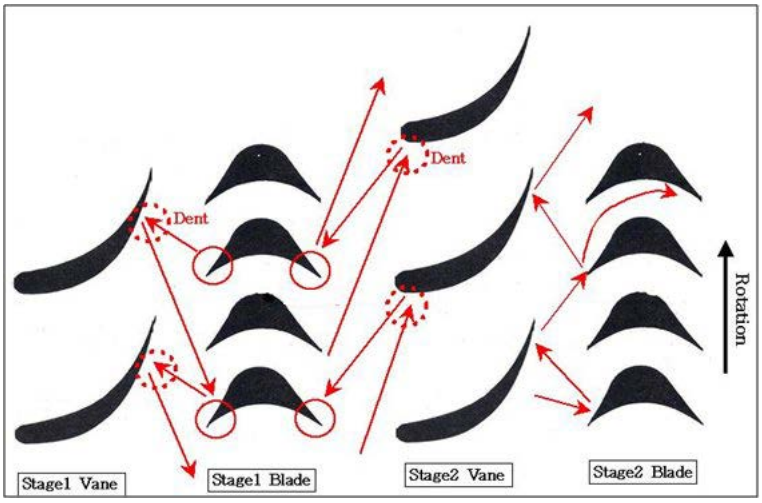

Figure I.28 .Schematics of the damage due to foreign particles moved from a compressor in the turbine

I.10.Conclusion

Blades may be considered to be the heart of turbine. Without blades there would be no power and the slightest fault in blading would mean a reduction in efficiency and costly repairs. In the gas turbine the transformation of energy reborn from the impacts of the exhausts gases with the blades that's rotate the wheel of turbine that provide a driving power for the shaft that turn with them the compressor . The Air is compressed and the pressure and temperature will rise. In each single turbine section there are blades holded by a disk or hub, and this last are connected with compressor with a shaft to determine the stage in gas turbine we must know the two types of blades one fixed and the other mobile. And the number of stages has effects on the blade structure and design. Turbine blades are the parts which undergo the most damaging solicitations. Because they are subjected to high temperature, high pressure and centrifugal forces that's make the defects grow rapidly.

Reference :

[1] https://fr.slideshare.net/GE_India/power-lifemax-solutions-forbe-gas-turbine-fleet (PowerGen India & Central Asia, Power LifeMax* - Solutions for B/E Gas Turbine Fleet, Ajay Gupta) consulted in 25/01/2020

[2] https://turbinetechnics.com/understanding-aeroderivative-gas-turbines. consulted in 25/01/2020

[3]. http://www.turbinetechnics.com/about-us/understanding-aeroderivative-gas-turbines. consulted in 25/01/2020

[4]. Zohuri, Bahman, and Patrick McDaniel. Combined cycle driven efficiency for next generation nuclear power plants: An innovative design approach. Springer, 2017

[5]. http://petrowiki.org/Gas_turbine_engines. consulted in 26/01/2020

[6].https://www.understandingchp.com/chp-applications-guide/4-3-gas-turbines/. Consulted in 26/01/2020

[7].http://airplanegroundschools.com/Transition-to-Turbopropeller-Powered-Airplanes/. Consulted in 26/01/2020

[8] http://www.slideshare.net/ZaibAmjad/turbine-engine-1. Consulted in 26/01/2020.

[9].http://www.energy.siemens.com/us/pool/hq/power-generation/steam turbines/downloads/Big%20SST_overview.pdf. Consulted in 26/01/2020

[10]http://gasturbinespower.asmedigitalcollection.asme.org/article.aspx?articleid=1886135 Consulted in 26/01/2020

[11] Rolls-Royce plc.The jet egine, Rolls-Royce plc 1986, Fifth edition Reprinted 1996 with revisions .England. ISBN 0902121 235.

[12]http://www.sandvik.coromant.com/engb/industrysolutions/condensing_power/gas_turbines/ pages/turbine-blade.aspx Consulted in 26/01/2020

[13]http://www.openmind-tech.com/uploads/tx_bcpageflip/BRO-hyperMILL-5AXIS-Aubes-de-Turbine-fr_013.pdf. Consulted in 26/01/2020

[14] Błachnio, Józef, and W. Pawlak. "Damageability of gas turbine blades-evaluation of exhaust gas temperature in front of the turbine using a non-linear observer." Advances in Gas Turbine Technology (2011): 435-464. DOI: 10.5772/29546

[15] Walls, D.P., Delaneuville, R.E., and Cunningham, S.E., “Damage Tolerance Based Life Prediction in Gas Turbine Engine under Vibratory High Cycle Fatigue,” Journal of

Engineering for Gas Turbines and Power, vol. 119, 1997, pp. 143–6 doi.org/10.1115/1.2815538.

[16] Hahn, George T., and Alan R. Rosenfield. "Local yielding and extension of a crack under plane stress." Acta Metallurgica 13.3 (1965): 293-306. doi.org/10.1016/0001-6160(65)90206-3

[17] Salehnasab, B., and E. Poursaeidi. "Mechanism and modeling of fatigue crack initiation and propagation in the directionally solidified CM186 LC blade of a gas turbine engine." Engineering Fracture Mechanics 225 (2020): 106842. doi.org/10.1016/j.engfracmech.2019.106842

[18] Xia, J., Zhou, K., Guo, Y., Wang, J., Lou, J., & Dai, Y. (2020). Preliminary design and CFD analysis of a radial inflow turbine and the turbine seal for an organic Rankine cycle using zeotropic mixture. Energy Conversion and Management, 209, 112647. doi.org/10.1016/j.enconman.2020.112647

[19] Rani, S., Agrawal, A. K., & Rastogi, V. (2017). Failure analysis of a first stage IN738 gas turbine blade tip cracking in a thermal power plant. Case studies in engineering failure analysis, 8, 1-10. doi.org/10.1016/j.csefa.2016.11.002

[20] SWAIN, B., MALLICK, P., PATEL, S., et al. Failure analysis and materials development of gas turbine blades. Materials Today: Proceedings, 2020. doi.org/10.1016/j.matpr.2020.02.859. doi.org/10.1016/j.matpr.2020.02.859

[21] RAO, V. Naga Bhushana, KUMAR, IN Niranjan, et PRASAD, K. Bala. Failure analysis of gas turbine blades in a gas turbine engine used for marine applications. International Journal of Engineering, Science and Technology, 2014, vol. 6, no 1, p. 43-48. doi.org/10.4314

[22] AUST , Jonas et PONS, Dirk. Taxonomy of Gas Turbine Blade Defects. Aerospace, 2019, vol. 6, no 5, p. 58.doi: 10.3390/aerospace6050058

[23]CARRICK, Harald B., AIRD, Graham Robert, et HUMPHRIES, Graeme. Power recovery. U.S. A retrospective review of some troublesome turbine blade failures, 5 mai 2011.

[24] MAZUR, Zdzislaw, LUNA-RAMIREZ, Alberto, JUÁREZ-ISLAS, J. A., et al. Failure analysis of a gas turbine blade made of Inconel 738LC alloy. Engineering failure analysis, 2005, vol. 12, no 3, p. 474-486. doi.org/10.1016/j.engfailanal.2004.10.002

[25] Kuang-HuaChang ,Design Theory and Methods Using CAD/CAE The Computer Aided Engineering Design Serie 2015, Pages 103-210. ISBN:978-0-12-398512-5

[26] DEWANGAN, Rajni, PATEL, Jaishri, DUBEY, Jaishri, et al. Gas turbines blades-a critical review of failure on first and second stages. Int J Mech Eng Robot Res, 2015, vol. 4, no 1, p. 216-223. ISSN 2278 – 0149

[27] RANI, S., AGRAWAL, A. K., et RASTOGI, V. Vibration analysis for detecting failure mode and crack location in first stage gas turbine blade. Journal of Mechanical Science and Technology, 2019, vol. 33, no 1, p. 1-10. DOI 10.1007/s12206-018-1201-x

[28] YOON, Wan No, KANG, Myung Soo, JUNG, Nam Kun, et al. Failure analysis of the defect-induced blade damage of a compressor in the gas turbine of a cogeneration plant.

International Journal of Precision Engineering and Manufacturing, 2012, vol. 13, no 5, p. 717-722. DOI: 10.1007/s12541-012-0093-4

[29] FRIJA, Mounir, BEN SGHAIER, Rabï, et FATHALLAH, Raouf. Modélisation du traitement superficiel par choc laser: Application sur une éprouvette représentative d'un bord d'attaque d'une ailette de turbine en superalliage de titane Ti6Al4V. In : Congrès français de mécanique. AFM, Maison de la Mécanique, 39/41 rue Louis Blanc, 92400 Courbevoie, France (FR), Bordeaux, 26 au 30 août 2013.URI:
http://hdl.handle.net/2042/52194

[30] S. Asadikouhanjani, M. Torfeh, and R. Ghorbanf .” failure analysis of a heavy duty gas turbine blade”,UDC 539.4, Strength of Materials, Vol. 46, No. 5, September, 2014. ISSN 0556-171X. doi.org/10.1007/s11223-014-9589-8

[31]. V. G. Rybalko and al (Analysis of the Causes of Fracture of Turbine Blades in a Gas Compressor) Unit Russian Academy of Sciences 2014 doi.org/10.1134/S0036029515100146

[32]. Wan No Yoon, Myung Soo Kang, Nam Kun Jung1, Jun Sung Kim and Byoung-Ho Choi,” failure analysis of the defect-induced blade damage of compressor in the gas turbine of a cogeneration plant “,DOI: 10.1007/s12541-012-0093-4, international journal of precision engineering and manufacturing vol. 13, No. 5, pp. 717-722.4 may 2012.

doi.org/10.1007/s12541-012-0093-4

[33] XIA, Jiaxi, ZHOU, Kehan, GUO, Yumin, et al. Preliminary design and CFD analysis of a radial inflow turbine and the turbine seal for an organic Rankine cycle using zeotropic mixture. Energy Conversion and Management, 2020, vol. 209, p. 112647.doi.org/10.1016/j.enconman.2020.112647

[34] YOON, Wan No, KANG, Myung Soo, JUNG, Nam Kun, et al. Failure analysis of the defect-induced blade damage of a compressor in the gas turbine of a cogeneration plant. International Journal of Precision Engineering and Manufacturing, 2012, vol. 13, no 5, p. 717-722. doi.org/10.1007/s12541-012-0093-4

CHAPITER II

Computational Fluid Dynamics (CFD) and Structural Analysis

1 Introduction

In order to analyze any problem in the numerical model, it is necessary to take into account the governing equation. One of the complex fields in the research is the Computational Fluid Dynamics (CFD) due to the interaction between fluid and structure. In other hand, finite element, finite volume and finite difference are considered as principal methods to perform the numerical analysis. Their understand with Navier-Stokes equations mean the control of CFD calculations and get out the suitable results. In this chapter, we are going to discuss about CFD from all different sides to take a view of this phenomenon.

II.1 CFD procedure

Due to the difficulties of using experimental analysis, computer software is developed to take a position in the research work. It maintains the money for different applications in short time. In order to solve these mathematical equations, computer scientists using high-level computer programming languages convert the equations into computer programs or software packages. The computational part simply means the study of the fluid flow using numerical simulations, which involves employing computer programs or software packages performed on high-speed digital computers to attain the numerical solutions [1-5]. Figure II.1 represents the procedure of CFD calculation with aid of numerical software. Figure II.2 indicates the main elements within a CFD analysis in software calculation. It must follow the next steps to examine a suitable CFD model,

- Creation of geometry
- Mesh generation
- Selection of physics and fluid properties
- Specification of boundary conditions
- Initialization and solution control
- **Monitoring convergence**
- Result report and visualization

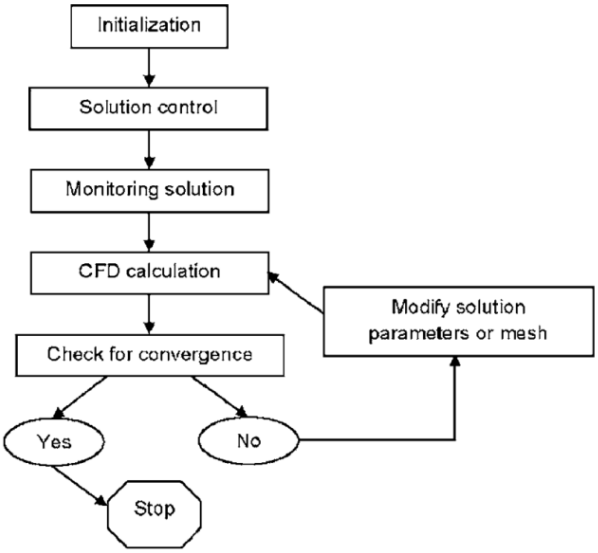

Figure II.1 : An overview of the solution procedure

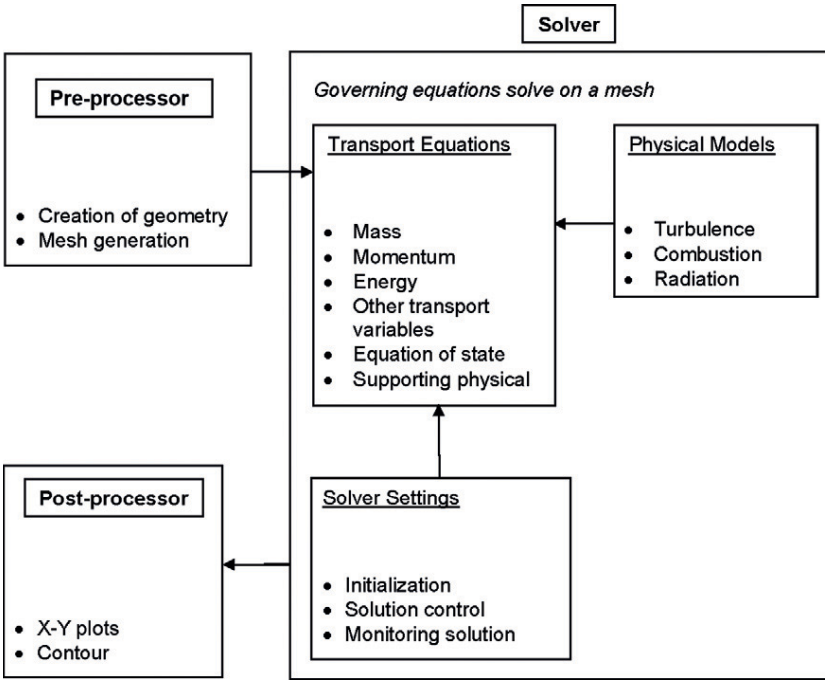

Figure II.2 Schematic diagram of the main elements within a CFD analysis in software calculation

II.2 Governing Equations for CFD

The Mathematical Models of interaction between fluid and solid structure are more complex than they appear. There are two mathematical models in order to study the CFD; rheology models and Navier–Stokes equations [6-13]. In this chapter, N-S equations will be presented. It is difficult to prove by the existing mathematical tools that a unique

solution exists for particular boundary conditions. Experience shows that the Navier–Stokes equations describe the flow of a Newtonian fluid accurately. Only in a small number of cases is possible to obtain an analytical solution of the Navier–Stokes equations. These flows are important for studying the fundamentals of fluid dynamics, but their practical relevance is limited [14].

In all cases in which such a solution is possible, many terms in the equations are zero. For other flows some terms are unimportant and we may neglect them; this simplification introduces an error. In most cases, even the simplified equations cannot be solved analytically; one has to use numerical methods. The computing effort may be much smaller than for the full equations, which is a justification for simplifications.

II.2.1 Equation of continuity

The integral form of the continuity equation follows directly from the Control Volume (CV) equation, by setting φ=1:

$$\frac{\partial}{\partial t}\int_{CV}\rho dV+\int_{S}\rho v.n.dS=0 \qquad \text{(II.1)}$$

$$\frac{\partial \rho}{\partial t}+div(\rho\vec{V})=0 \qquad \text{(II.2)}$$

This form can be transformed into a form specific to a given coordinate system by providing the expression for the divergence operator in that system. The following equation presents the cartesian form in both tensor and expanded notation:

$$\frac{\partial \rho}{\partial t}+\frac{\partial(\rho u_i)}{\partial x_i}=\frac{\partial \rho}{\partial t}+\frac{\partial(\rho u_x)}{\partial y}+\frac{\partial(\rho u_y)}{\partial y}+\frac{\partial(\rho u_z)}{\partial z}=0 \qquad \text{(II.3)}$$

Where x_i *(i=1,2,3)* or *(x,y,z)* are the Cartesian coordinates and u_i or(u_x,u_y,u_z) are the Cartesian components of the velocity vector v. This last formula is the mass conservation equation for compressible flow. While, the mass conservation equation for incompressible flow in cartesian coordinates may expresses as following:

$$\frac{\partial u}{\partial x}+\frac{\partial u}{\partial y}+\frac{\partial u}{\partial z}=0 \qquad \text{(II.4)}$$

For Computational Fluid Dynamic (CFD), the momentum conservation equation is considered as an important approach to use the control volume method. In this method, one uses Eqs. (1.2) and (1.4) and replaces φ by v, e.g., for a fixed fluid-containing volume of space:

$$\frac{\partial}{\partial t}\int_{CV}\rho v dV+\int_{S}\rho v v.n.dS=\sum f \qquad \text{(II.5)}$$

To express the right hand side in terms of intensive properties, one has to consider the forces which may act on the fluid in a CV:

- surface forces (pressure, normal and shear stresses, surface tension etc.);
- body forces (gravity, centrifugal and Coriolis forces, electromagnetic forces, etc.).

The surface forces due to pressure and stresses are, from the molecular point of view, the microscopic momentum fluxes across a surface. If these fluxes cannot be written in terms of the properties whose conservation the equations govern (density and velocity), the system of equations is not closed; that is, there are fewer equations than dependent variables and solution is not possible. This possibility can be avoided by making certain assumptions. The simplest assumption is that the fluid is Newtonian; fortunately, the Newtonian model applies to many actual fluids [14].

For Newtonian fluids, the stress tensor T, which is the molecular rate of transport of momentum, can be written:

$$T=-\left(p+2/3\mu\nabla.v\right)I+2\mu D \qquad \text{(II.6)}$$

where μ is the dynamic viscosity, I is the unit tensor, p is the static pressure and D is the rate of strain (deformation) tensor:

$$D=0.5\left[\nabla v+\left(\nabla v\right)^{T}\right]$$

(II.7)

These two equations may be written, in index notation in Cartesian coordinates, as follows:

$$T_{ij}=-\left(p+(2/3)\mu\frac{\partial u_j}{\partial x_j}\delta_{ij}+2\mu D_{ij}\right) \qquad \text{(II.8)}$$

$$D_{ij} = 0.5\left(\frac{\partial u_i}{\partial x_j} + \frac{\partial u_j}{\partial x_i}\right) \quad \text{(II.9)}$$

where δ_{ij} is Kronecker symbol ($\delta_{ij} = 1$ *if* $i = j$ *and* $\delta_{ij} = 0$ otherwise). For incompressible flows, the second term in the brackets in Eq. (II.8) is zero by virtue of the continuity equation. The following notation is often used in literature to describe the viscous part of the stress tensor:

$$\tau_{ij} = 2\mu D_{ij} - (2/3)\mu\delta_{ij}\nabla.v \quad \text{(II.10)}$$

For non-Newtonian fluids, the relation between the stress tensor and the velocity is often defined by a set of partial differential equations and the total problem is far more complicated. For the class of non-Newtonian fluids which are described using the same kind of constitutive relation as above, but only require a variable viscosity (typically a non-linear function of velocity gradients and temperature) or a stress model comparable to the Reynolds stress model. However, different types of non-Newtonian fluids require different constitutive equations as seen in Bird and Wiest (1995) [15]. With the body forces (per unit mass) being represented by b, the integral form of the momentum conservation equation becomes:

$$\frac{\partial}{\partial t}\int_{CV} \rho v dV + \int_S \rho v v.ndS = \int_S T.ndS + \int_{CV} \rho b dV \quad \text{(II.11)}$$

A coordinate-free vector form of the momentum conservation equation (II.11) is readily obtained by applying Gauss' divergence theorem to the convection and diffusion flux terms:

$$\frac{\partial(\rho v)}{\partial t} + \nabla.(\rho v v) = \nabla.T + \rho b \quad \text{(II.12)}$$

The corresponding equation for the *i* th Cartesian component is:

$$\frac{\partial(\rho u_i)}{\partial t} + \nabla.(\rho u_i v) = \nabla.t_i + \rho b_i \quad \text{(II.13)}$$

Because momentum is a vector quantity, the convection and diffusion fluxes of it through a CV boundary are the scalar products of second rank tensors (*ρvv and T*) with the surface vector *n dS*. The integral form of the above equations is:

$$\frac{\partial}{\partial t}\int_{CV}\rho u_i dV + \int_S \rho u_i v.ndS = \int_S t_i.ndS + \int_{CV}\rho b_i dV \qquad \text{(II.14)}$$

where

$$t_i = \mu\nabla u_i + \mu(\nabla v)^T.i_i - \left(p + (2/3)\mu\nabla.V\right)i_i = \tau_{ij}i_j - pi_i \qquad \text{(II.15)}$$

Here b_i stands for the i the component of the body force, superscript T means transpose and i_i is the Cartesian unit vector in the direction of the coordinate x_i. In Cartesian coordinates one can write the above expression as:

$$t_i = \mu\left(\frac{\partial u_i}{\partial x_j} + \frac{\partial u_j}{\partial x_i}\right)i_j - \left(p + (2/3)\mu\frac{\partial u_j}{\partial x_i}\right)i_i \qquad \text{(II.16)}$$

Equation (II.13) is in strong conservation form. A non-conservative form of this equation can be obtained by employing the continuity equation; because

$$\nabla.(\rho v u_i) = u_i\nabla.(\rho v) + \rho v.\nabla u_i \qquad \text{(II.17)}$$

it follows that:

$$\rho\frac{\partial u_i}{\partial t} + \rho v.\nabla.u_i = \nabla.t_i + \rho b_i \qquad \text{(II.18)}$$

The pressure term contained in t_i can also be written as

$$\nabla.(pi_i) = \nabla p.i_i \qquad \text{(II.19)}$$

The pressure gradient is then regarded as a body force; this amounts to non conservative treatment of the pressure term. The non-conservative form of equations is often used in finite difference methods, as it is somewhat simpler. In the limit of a very fine grid, all equation forms and numerical solution methods give the same solution; however, on coarse grids the non-conservative form introduces additional errors which may become important.

If the expression for the viscous part of the stress tensor, Eq. (II.10), is substituted into Eq. (II.13) written in index notation and for Cartesian coordinates, and if gravity is the only body force, one has:

$$\frac{\partial(\rho u_i)}{\partial t}+\frac{\partial(\rho u_j u_i)}{\partial x_j}=\frac{\partial \tau_{ij}}{\partial x_j}-\frac{\partial p}{\partial x_i}+\rho g_i \qquad \text{(II.20)}$$

II.2.2 Incompressible Flow

The incompressible flow means the density of its fluid is constant in each situation to a high degree of accuracy such as water [16-18]. In other words, for an incompressible fluid, the rate of change of following the motion is zero: that is,

$$\nabla . v = 0 \qquad \text{(II.21)}$$

$$\frac{\partial u_i}{\partial t}+\nabla.(u_i v)=\nabla.(\nu \nabla u_i)-\frac{1}{\rho}\nabla.(\rho i_i)+b_i \qquad \text{(II.22)}$$

II.3 Applications of CFD

The different applications illustrate the importance of CFD and clearly show how it has evolved through rigorous development of numerical techniques. Despite its long-standing use within academic circles, CFD is flourishing in many industrial sectors. This unprecedented occurrence is partly due to the increasing availability and accessibility of multi-purpose commercial computer programs. CFD domain is used in many different applications such as:

- As a Research Tool
- As an Educational Tool in Basic Thermal-Fluid Science
- As a Design Tool
- Aerospace
- Automotive Engineering
- Biomedical Science and Engineering
- Chemical and Mineral Processing
- Civil and Environmental Engineering
- Metallurgy

- Nuclear Safety
- Power Generation
- Sports

II.4 CFD Techniques

Through the history of the technology, the numerical methods are the best factors which have been development including the computers which have led to the growth and augmentation for the use of its realistic mathematical models in science and engineering [19, 20]. Some of the basic computational methods that are required to solve the governing equations of fluid dynamics using numerical analysis are finite difference and finite volume techniques. They are employed to obtain an approximate solution for the governing equations of flow problems with appropriate boundary conditions applied for the specific problem considered. The process of obtaining the computational solution consists of two stages. The first stage involves the conversion of the partial differential equations and auxiliary (boundary and initial) conditions into a system of discrete algebraic equations. This stage is commonly known as the discretization stage. The second stage of the solution process involves the implementation of numerical methods to provide a solution to the system of algebraic equations. In this chapter, Finite Volume method will be discussed due to its usage in our project [21].

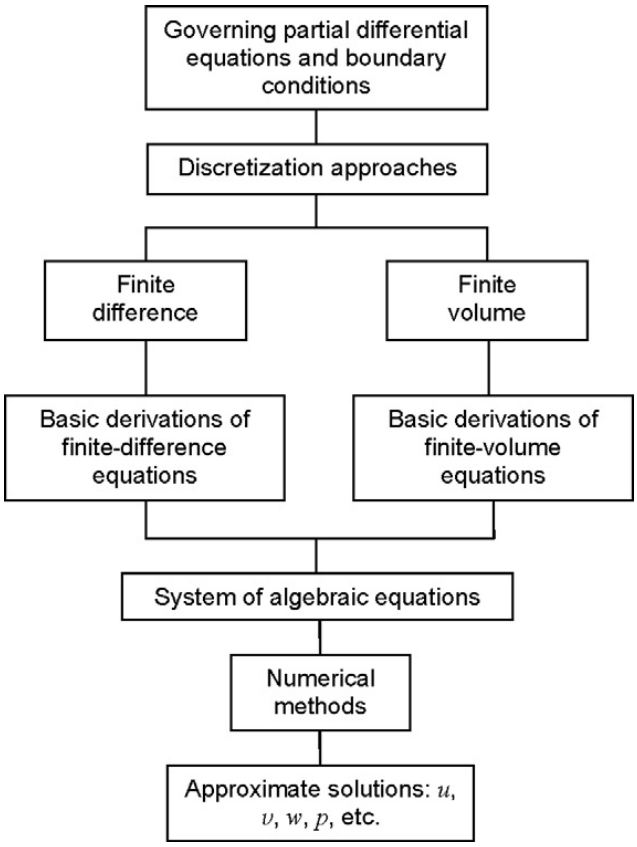

Figure II.3 Schematic diagram for CFD according to numerical methods calculation

II.5 Finite Volume Method (FVM)

Finite Volume Method (FVM) is usually considered as a solution for some complex cases of Computational Fluid Dynamics (CFD). It is among the most powerful means for solving different engineering problems. It is used in fluid mechanics, rheology, aerodynamics of vehicles (lift and drag), hydrodynamics of ships, chemical process engineering (polymer molding), biomedical engineering (blood flow), and many more engineering applications are considered fields [22-24].

II.5.1 Overview

The finite-volume method discretizes the integral form of the conservation equations directly in physical space. It was initially introduced by researchers like McDonald (1971) [25] and MacCormack and Paullay (1972) [26] for the solution of two-dimensional time-dependent Euler equations, and it was later extended to three-dimensional flows by Rizzi and Inouye (1973) [27]. The computational domain is subdivided into a finite number of contiguous control volumes, where the resulting

statements express the exact conservation of relevant properties for each of the control volumes. At the centroid of each of the control volumes, the variable values are calculated. Interpolation is used to express variable values at the control volume surface in terms of the center values, and suitable quadrature formulae are applied to approximate the surface and volume integrals. An algebraic equation for each of the control volumes can be obtained, in which a number of the neighboring nodal values appear.

II.5.2 Diffusion equation

In general, many complex issues need to solutions. Todays, numerical data consider one of the best solutions which depends on numerical methods as basic equations. The basic equation of FV totally depends to control Computational Fluid Dynamic (CFD) domains. Here, the numerical method evolved on the basis of this integration.

$$\mathrm{div}\left(\Gamma \mathrm{grad}\phi\right) + S_{\phi} = 0 \qquad \text{(II.23)}$$

where Γ, S and ∅ are the diffusion coefficient, the source term and Boundary values at boundarypoints, respectively. The control volume integration, which is the fundamental step of the FVM that distinguishes it from all other CFD techniques, equation can be written as the following form:

$$\int_{CV} \mathrm{div}\left(\Gamma \mathrm{grad}\phi\right) \mathrm{dV} + \int_{CV} S_{\phi} \mathrm{dV} = \int_{A} \mathrm{n} \,.\left(\Gamma \mathrm{grad}\phi\right) \mathrm{dA} + \int_{CV} S_{\phi} \mathrm{dV} = 0 \qquad \text{(II.24)}$$

This equation transforms the volume integrals into surface integrals of fluxes all around the control volume. It must take into consideration the next general steps to solve any FV problem:

II.5.3 Grid Generation

The grid generation means to divide the section of problem into small discrete control volumes which is the first step of the FVM. Figure II.4 shows the boundary points of FV for one-dimensional steady state diffusion. To facilitate the solution of a problem, different points which indicate in Figure II.4 can be described as; P, W, E, N, S, B and T are a general nodal point which is defined by its neighbors, west, east, north, south, bottom and top, respectively. The two, four and six faces of the volume control are defined at their sides by (w, e, n, s, b and t) respectively. The distances of these points are given in Figure II.1 and Figure II.5.

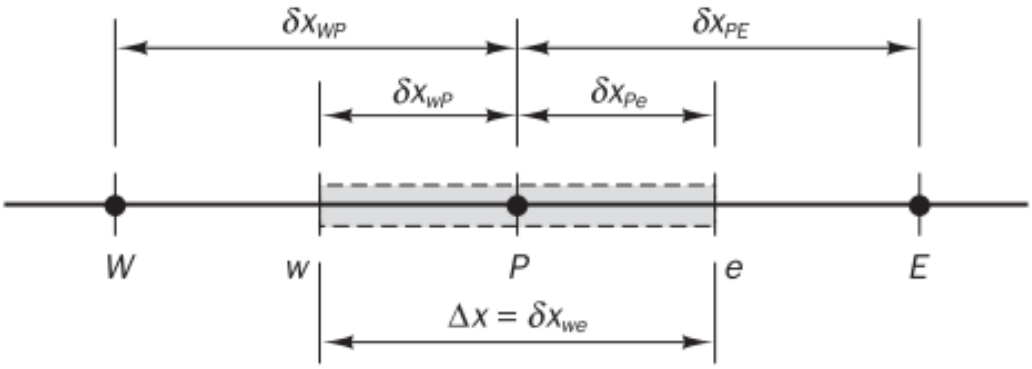

Figure II.4 A part of the one dimensional grid

II.5.4 Discretization

This is the necessary step of the FVM which is the integration of the governing equation over a control volume to yield a discretized equation at its nodal point P. Equation II.6 presents the integration of FV discretization at 1D diffusion along direction X

$$-\int_V \frac{\partial}{\partial X_i}\left(\Gamma \frac{\partial \phi}{\partial X_i}\right) dV = \int_V S dV \rightarrow -\int_A n_X \left(\Gamma \frac{\partial \phi}{\partial X_i}\right) dA = \int_V S dV \tag{II.25}$$

With the above two approximations, the left and right- hand-side terms become

$$\int_A n_X \left(\Gamma \frac{\partial \phi}{\partial X_i}\right) dA = \left(\Gamma A \frac{\partial \phi}{\partial x}\right)_e - \left(\Gamma A \frac{\partial \phi}{\partial x}\right)_w \tag{II.26}$$

$$\int_V S dV = \bar{S}.\Delta V \tag{II.27}$$

For an uniform grid the central difference approximation leads to

$$\Gamma_e A_e \left(\frac{\phi_E - \phi_P}{\delta x_{PE}}\right) - \Gamma_w A_w \left(\frac{\phi_P - \phi_W}{\delta x_{WP}}\right) + \left(S_u + S_p \phi_P\right) = 0 \tag{II.28}$$

Equation (II.28) is often written in the following form

$$a_P \phi_P = a_E \phi_E + a_W \phi_W + S_u \tag{II.29}$$

with coefficients

$$a_W = \frac{\Gamma_w A_w}{\delta x_{WP}}, a_E = \frac{\Gamma_e A_e}{\delta x_{PE}}, a_P = a_E + a_W - S_P \tag{II.30}$$

Equation (II.30) can be simplified to a three-dimensional problem as

$$a_P \phi_P = \sum_{6}^{F=1} a_F \phi_F + S_u \tag{II.31}$$

$$a_P\phi_P = a_E\phi_E + a_W\phi_W + a_N\phi_N + a_S\phi_S + a_T\phi_T + a_B\phi_B + S_u \quad \text{(II.32)}$$

with coefficients

$$a_F = \frac{\Gamma_f A_f}{\delta x_{FP}}, a_P = \sum_{6}^{F=1} a_F - S_P \quad \text{(II.33)}$$

Where F runs over the 6 near- neighbor nodes W, E, S, N, B and T and the small letters represent the corresponding cell-faces (adjacent to cells F and P). $\emptyset_P$ and $\emptyset_F$ represent the unknown values of that need to be numerically determined.

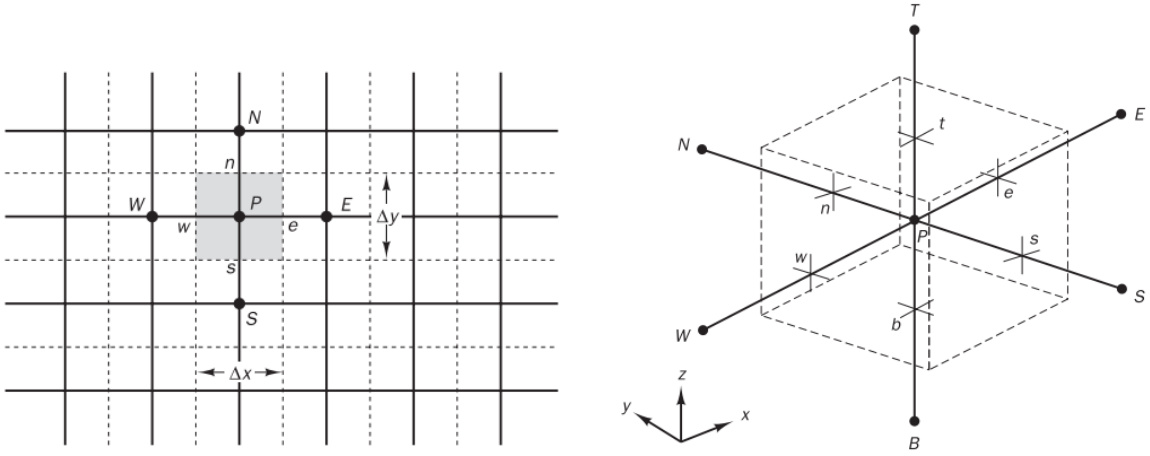

(a) (b)

Figure II.5 FVM Discretization (a) A part of the 2D grid, and (b) A cell in 3D and neighboring nodes.

II.5.5 Physical Boundary Conditions

After discretization over each volume method, we are finding a system of algebraic equation. Which are easily solved by numerical scheme such as Gauss-Siedel method. To study any problem by numerical data, boundary conditions must be identified [28-29]. The next boundary conditions of CFD calculations should taking into consideration

- Inlet boundary
- Outlet boundary.
- Symmetry plane boundary
- Impermeable no-slip walls.

FVM allows handling of complex geometric shapes in large quantities and focus on the nature of conditions (boundary). In the contrary, it is difficult to obtain theoretical results of convergence.

II.6 Tranform from CFD to Structural model

It is not possible to analyze fracture domain in CFD software. To resolve this problem, three different steps must be performed (Figure II.6). In order to study the fracture mechanics based on results of CFD, obtained values from CFD will be imported into structural geometry in presence of defect. In our study, we have used ANSYS Workbench software with the computational fluid dynamics Software (CFD section). A steady state gas flow analysis and pressure distributions were carried out. These pressures across turbine gas blade were obtained by the importation of the other section called APDL (Ansys Parametric Design Language) where the figure II.6 illustrates the methodology of numerical steps. For accurate analysis of structural model, finite element method is used.

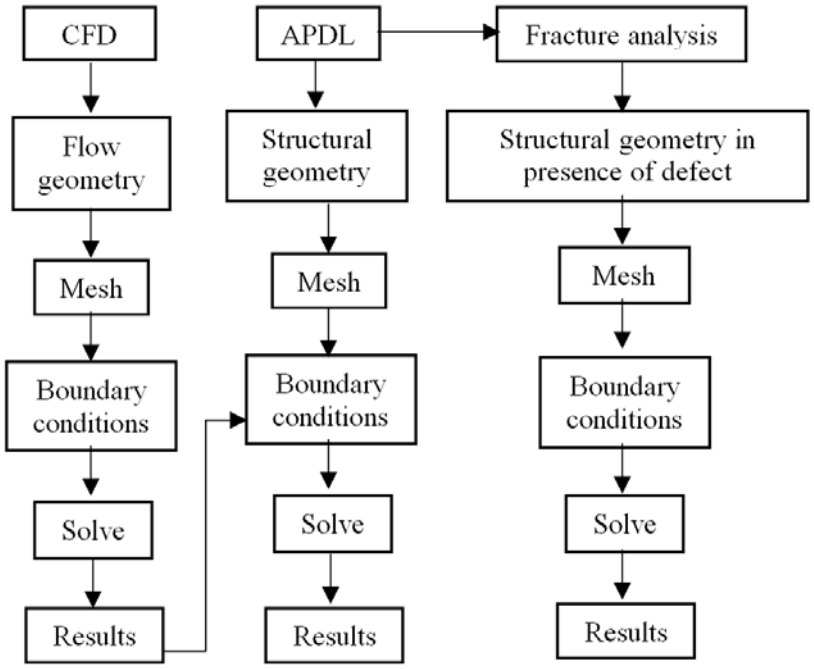

Figure II.6 : Schematic description for numerical methodology

II.6.1 Finite Element Analysis (FEA)

II.6.1.1 Abstract

Finite-element analysis is a powerful numerical analysis process widely used in engineering to analyze and study the functional performance of an object by dividing it into a number of small building blocks, called finite elements. For example, functional

performances of an object or continuum, such as a structure's stresses and deflections, are predicted using FEA. The core of the FEA method is an idealization of the object or continuum by a finite number of discrete variables. For this purpose, the object is first divided into a grid of elements that forms a model of the real object. This process is also called meshing. Each element is a simple shape such as a square, triangle, or cube or other standard shape for which the Finite-element Program has information to write the governing equations in the form of a stiffness matrix. The unknown parameters for each element are the displacements at the node points, which are the points at which the elements are connected. The Finite-Element Program assembles the stiffness matrices for these simple elements to form the global stiffness matrix for the entire model. This stiffness matrix is solved for the unknown displacements, given the known forces and boundary conditions. From the displacement at the nodes, the stresses in each element can then be calculated. The following steps are usually followed in applying FEA:

1. Discretization of the given continuum
2. Selection of the solution approximation
3. Development of element matrices and equations
4. Assembly of the element equations
5. Solution for the unknown at the nodes
6. Interpretation of the result

A number of software packages for engineering analysis have been developed that are capable of covering a wide range of applications [30]. In this section, FEA will be discussed in more details

II.6.1.2 History of FEM

The idea of finite element method has been become very important since 1943. In this period some researchers have been developed basic concepts depending on mathematics and physics theories. In 1960, the word “Finite Element Method” has been announced on the energy principles to the formation of structural analysis by Argyris and Kelsey [31]. Duringtwo decades 1960’s and 1970’s, some important studies showed about the formulation of the finite element method based on the principles of mathematical theories including improving the speed and memory capacity of computers. Thus, lots of computer feature contributed to the development and prosperity of this method.

The importance of the finite element method emerged especially in mechanics field which concentrated on the elastic analysis of aircraft problem. It is necessary to note that this method has been successfully used to the analysis of three dimensional problems for many fields especially in heavy industries, hydrocarbons flow problems, non-linear analysis for different kinds of materials such as the composite material.

II.6.1.3 Discretization of FEA

This method was applied for the first time in problems involved in the analysis of the constraints and since, it was extended in other problems involved in the continuous medium. In all the applications the analyst seeks to calculate a quantity of field, Finite element method (shortened MEF) represents a method to obtain a numerical solution corresponding to a specific problem. This section will explain how to derive the fundamental equations for the FEM based on the Galerkin method. Let us consider again the boundary-value problem stated by Equation:

$$\begin{cases} L\left[u(x)\right] = f(x)\left(a \le x \le b\right) \\ BC\left(Boudaryconditions\right): u(a) = u_a u(b) = u_b \end{cases} \tag{II.34}$$

First, divide the region of interest (a≤x≤b) into n subregions as illustrated in figure II.7 these subregions are called “elements” in the FEM.

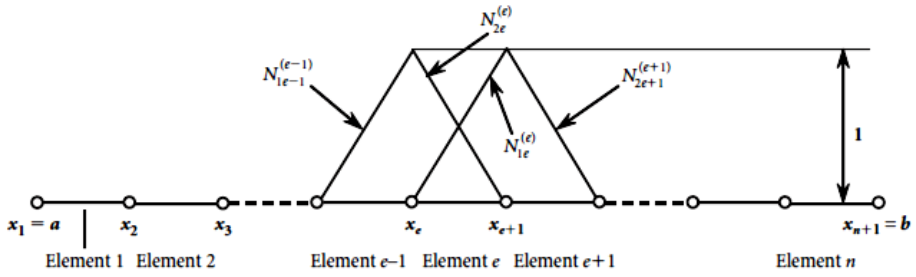

Figure II.7 Discretization of the domain to analyze by finite elements and their interpolation functions.

Now, let us assume that an approximate solution ū of u can be expressed by a piecewise linear function which forms a straight line in each subregion, i.e.,

$$u(x) = \sum_{n+1}^{i=1} u_i N_i(x) \tag{II.35}$$

Where u_i represents the value of u in element "e" at a boundary point, or a nodal point "i" between two one-dimensional elements. Functions Ni(x) are the following piecewise linear functions and are called interpolation or shape functions of the nodal point "i:"

$$\begin{cases} N_{1e}^{(e)} = \dfrac{x_{e+1} - x}{x_{e+1} - x_e} = \dfrac{x_{2e} - x}{x_{2e} - x_{1e}} = \dfrac{h^{(e)} - \varepsilon}{h^{(e)}} \\ N_{2e}^{(e)} = \dfrac{x - x_{e+1}}{x_{e+1} - x_e} = \dfrac{x - x_{1e}}{x_{2e} - x_{1e}} = \dfrac{\varepsilon}{h^{(e)}} \end{cases} \quad \text{(II.36)}$$

where e (e =1, 2, . . . , n) denotes the element number, x_i the global coordinate of the nodal point i (i=1, . . . , e −1, e, . . . n, n+1), N(e) i_e the value of the interpolation function at the nodal point i_e (i_e=1_e, 2_e) which belongs to the eth element, 1_e and 2_e the number of two nodal points of the eth element. Symbol ξ is the local coordinate of an arbitrary point in the eth element, ξ =x −x_e=x −$x1_e$ (0≤ξ ≤h(e)), h(e) is the length of the e^{th} element, and h(e) is expressed as h(e) =x_e+1 −x_e=x2e −$x1_e$. As the interpolation function, the piecewise linear or quadric function is often used. Generally speaking, the quadric interpolation function gives better solutions than the linear one. The Galerkin method-based FEM adopts the weighting functions w_i(x) equal to the interpolation functions N_i(x), i.e.,

$$w_i(x) = N_i(x) \ (i = 1,\ 2, \ldots,\ n+1) \quad \text{(II.37)}$$

Next is the integral equation

$$\int_D N_i R \partial v = 0 \quad \text{(II.38)}$$

In the FEM, a set of simultaneous algebraic equations for unknown variables of u(x) at the ith nodal point ui and those of its derivatives du/dx, (du/dx)i are derived by integrating Equation (II.38) by parts and then by taking boundary conditions into consideration. The simultaneous equations can be easily solved by digital computers to determine the unknown variables ui and (du/dx)i at all the nodal points in the region considered.

II.6.1.4 FEM in two-dimensional elastostatic problems

Generally speaking, elasticity problems are reduced to solving the partial differential equations known as the equilibrium equations together with the stress–strain relations or the constitutive equations, the strain–displacement relations, and the compatibility equation

under given boundary conditions. The exact solutions can be obtained in quite limited cases only and in general cannot be solved in closed forms. In order to overcome these difficulties, the FEM has been developed as one of the powerful numerical methods to obtain approximate solutions for various kinds of elasticity problems. The FEM assumes an object of analysis as an aggregate of elements having arbitrary shapes and finite sizes (called finite element), approximates partial differential equations by simultaneous algebraic equations, and numerically solves various elasticity problems. Finite elements take the form of line segment in one-dimensional problems as shown in the preceding section, triangle or rectangle in two-dimensional problems, and tetrahedron, cuboid, or prism in three-dimensional problems. Since the procedure of the FEM is mathematically based on the variational method, it can be applied not only to elasticity problems of structures but also to various problems related to thermodynamics, fluid dynamics, and vibrations which are described by partial differential equations. Elements of finite-element procedures in the analysis of plane elastostatic problems

Limited to static (without time variation) elasticity problems, the procedure described in the preceding section is essentially the same as that of the stress analyses by the FEM. The procedure is summarized as follows:

• Procedure 1: Discretization Divide the object of analysis into a finite number of finite elements.

• Procedure 2: Selection of the interpolation function Select the element type or the interpolation function which approximates displacements and strains in each finite element.

• Procedure 3: Derivation of element stiffness matrices Determine the element stiffness matrix which relates forces and displacements in each element.

• Procedure 4: Assembly of stiffness matrices into the global stiffness matrix Assemble the element stiffness matrices into the global stiffness matrix which relates forces and displacements in the whole elastic body to be analyzed.

• Procedure 5: Rearrangement of the global stiffness matrix Substitute prescribed applied forces (mechanical boundary conditions) and displacements (geometrical boundary conditions) into the global stiffness matrix, and rearrange the matrix by collecting unknown variables for forces and displacements, say in the left-hand side, and known values of the forces and displacements in the right-hand side in order to set up simultaneous equations.

• Procedure 6: Derivation of unknown forces and displacements Solve the simultaneous equations set up in Procedure 5 above to solve the unknown variables for forces and displacements. The solutions for unknown forces are reaction forces and those for unknown displacements are deformations of the elastic body of interest for given geometrical and mechanical boundary conditions, respectively.

• Procedure 7: Computation of strains and stresses Compute the strains and stresses from the displacements obtained in Procedure 6 by using the strain–displacement relations and the stress–strain relations explained later.

II.6.1.5 Fundamental formulae in plane elastostatic problems

(a) Equations of Equilibrium

Consider the static equilibrium state of an infinitesimally small rectangle with its sides parallel to the coordinate axes in a two-dimensional elastic body as shown in figure II.8. If the body forces F_x and F_y act in the directions of the x- and the y-axes, respectively, the equations of equilibrium in the elastic body can be derived as follows:

$$\begin{cases} \dfrac{\partial \delta_x}{\partial x} + \dfrac{\partial \tau_{xy}}{\partial y} + F_x = 0 \\ \dfrac{\partial \tau_{yx}}{\partial x} + \dfrac{\partial \delta_y}{\partial y} + F_y = 0 \end{cases} \qquad \text{(II.39)}$$

where σ_x and σ_y are normal stresses in the x- and the y-axes, respectively, with τ_{xy} and τ_{yx}shear stresses acting in the x–y plane.

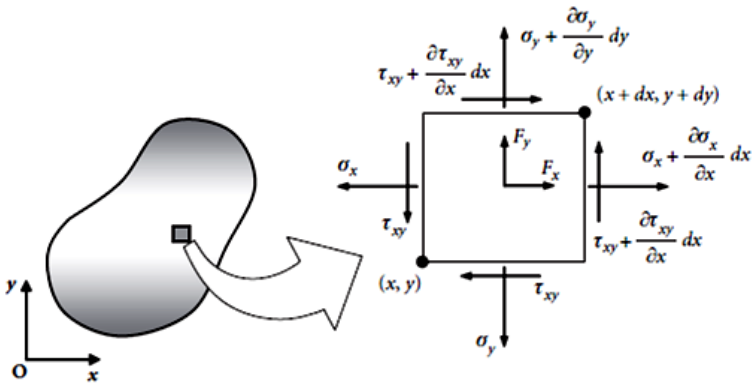

Figure II.8 Stress states in an infinitesimal element of a two-dimensional elastic body.

The shear stresses τ_{xy} and τ_{yx} are generally equal to each other due to the rotational equilibrium of the two-dimensional elastic body around its center of gravity.

(b) STRAIN–DISPLACEMENT RELATIONS

If the deformation of a two-dimensional elastic body is infinitesimally small under the applied load, the normal strains $\varepsilon_x$and ε_y in the directions of the x- and the y-axes, respectively, and the engineering shearing strain γ_{xy} in the x–y plane are expressed by the following equations:

$$\begin{cases} \varepsilon_x = \dfrac{\partial u}{\partial x} \\ \varepsilon_y = \dfrac{\partial v}{\partial y} \\ \gamma_{xu} = \dfrac{\partial v}{\partial x} + \dfrac{\partial u}{\partial y} \end{cases} \qquad \text{(II.40)}$$

where u and v are infinitesimal displacements in the directions of the x- and the y-axes, respectively.

(c) STRESS–STRAIN RELATIONS (CONSTITUTIVE EQUATIONS)

The stress–strain relations describe states of deformation, strains induced by the internal forces, or stresses resisting against applied loads. Unlike the other fundamental equations which can be determined mechanistically or geometrically, these relations depend on the properties of the material, and they are determined experimentally and often called constitutive relations or constitutive equations. One of the most popular relations is the generalized Hooke's law which relates six components of the three-dimensional stress tensor with those of strain tensor through the following simple linear expressions [32]:

$$\begin{cases} \sigma_x = \dfrac{vE}{(1+v)(1-2v)} e_v + 2G\varepsilon_x \\ \sigma_y = \dfrac{vE}{(1+v)(1-2v)} e_v + 2G\varepsilon_y \\ \sigma_z = \dfrac{vE}{(1+v)(1-2v)} e_v + 2G\varepsilon_z \\ \tau_{xy} = G\gamma_{xy} = \dfrac{E}{2(1+v)}\gamma_{xy} \\ \tau_{yz} = G\gamma_{yz} = \dfrac{E}{2(1+v)}\gamma_{yz} \\ \tau_{zx} = G\gamma_{zx} = \dfrac{E}{2(1+v)}\gamma_{zx} \end{cases} \quad \text{(II.41)}$$

(d) BASIC STEPS IN THE FINITE ELEMENT METHOD

The basic steps involved in any finite element analysis consist of the following:

Preprocessing Phase

1. Create and discredited the solution domain into finite elements; that is subdivide the problem into nodes and elements.

2. Assume a shape function to represent the physical behavior of an element; that is an approximate continuous function is assumed to represent the solution of an element.

3. Develop equations for an element.

4. Assemble the elements to present the entire problem. Construct the global stiffness matrix.

5. Apply boundary conditions. Initial conditions and loading.

Solution Phase

6. Solve a set of linear or nonlinear algebraic equations simultaneously to obtain nodal results. Such as displacement values at different nodes or temperature values at different nodes in a heat transfer problem.

Postprocessing Phase

7. Obtain other important information. At this point, you may be interested in values of principal stresses. Heat fluxes, etc. In general, there are several approaches to formulating finite element problems: 1) Direct Fornlulatiotz, 2) The Minitn~tm Total Potenrinl Energy Fonnulution. And 3) Weighted Re.vicluc11 Formulations. Again. It is

important to note that the basic steps in. Evolved in any finite element analysis.Regardless of how we generate the finite element model. Will be the same as those listed above [33].

(e) FEM Notation

As the name suggests the FEM treat the continuous problem domain as a collection of individual finite elements. The problem parameters are defined on each of the nodes of a typical element. Let us now have a look to the key definitions of the FEM notation.

• Dimensionality: The elements can be defined differently depending on the problem context. Dimensionality indeed expresses wether the element has 1, 2 or 3 space dimensions.

• Nodal Points: Every element is described by its nodal points. Frequently the nodal points are chosen to be the corners of the element. However in case of non linear geometries nodal points are also defined on the edges.

• Geometry: This term is used to describe the domain on which finite element discretization needs to be applied. It can be smooth an regular (e.g. a rectangular plate), or complex (e.g. surface of a machine part). The geometry is defined by the placements of the nodal points.

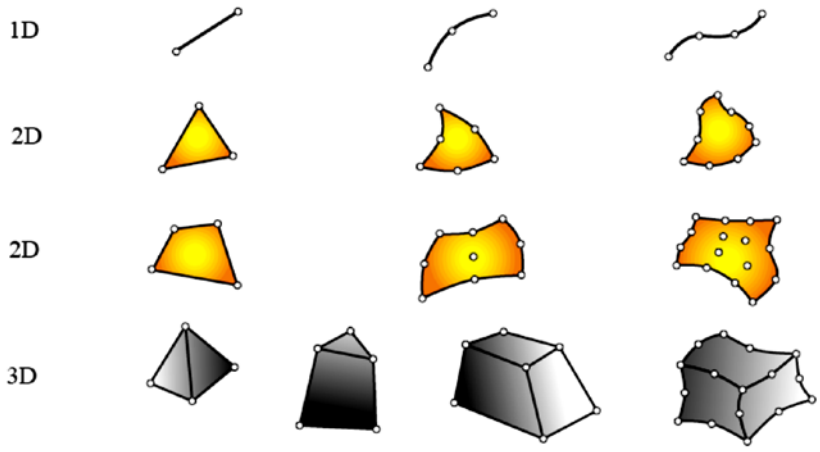

Figure II.9 Typical Finite Element Geometries

• Degrees of Freedom: The degree of freedom is the number of ways in which the original problem domain can change its state. In the case of the continous problem domain, the DOF is infinite, because problem characteristics can be defined in each point on the domain. In the discrete FEM domain, instead, the DOF is limited by the number elements, because problem characteristics can only be defined on the nodal points.

• Nodal Forces: A set of nodal forces (or any other actions depending on the problem) are defined on each nodal point. From the mathematical point of view this corresponds to the non-homogeneous right hand side of the governing DE.

(f) Mechanical Approach

There are different approaches to the setup of a Finite Element Method. We decided to start discovering FEM this way, most of the terms and concepts in the mathematical formulation find its origins in concepts. Furthermore understanding the connection between the physical model and the mathematical formulation is very valuable, as it enables us to have bigger control on the problem treated [34].

(g) Nodes

As shown in figure II.10, the transformation of the practical engineering problem to a mathematical representation is achieved by discretizing the domain of interest into elements (sub-domains).

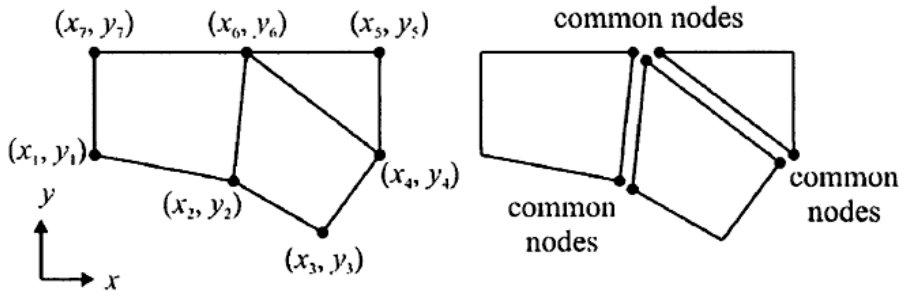

Figure II.10 Division of a domain into elements

These elements are connected to each other by their "common" nodes. A node specifies the coordinate location in space where degrees of freedom and actions of the physical problem exist. The nodal unknown(s) in the matrix system of equations represents one (or more) of the primary field variables. Nodal variables assigned to an element are called the degrees of freedom of the element. The common nodes shown in figure III.10 provide continuity for the nodal variables (degrees of freedom).

Table II.1 freedom degree and force vector in Finite elements analysis

Discipline	DOF	Force Vector
Structural/solid	Displacement	Mechanical force
Heat conduction	Temperature	Heat flux
Acoustic fluid	Displacement potential	Particle velocity
Potential flow	Pressure	Particle velocity
General flows	Velocity	Fluxes
Electrostatics	Electric potential	Charge density
Magnetostatics	Magnetic potential	Magnetic intensity

Degrees of freedom (DOF) of a node are dictated by the physical nature of the problem and the element type. Table 1presents the DOF and corresponding "forces" used in FEA for different physical problems [35].

(h) Elements

Depending on the geometry and the physical nature of the problem, the domain of interest can be discretized by employing line, area, or volume elements. Some of the common elements in FEA are shown in figure II.11. Each element, identified by an element number, is defined by a specific sequence of global node numbers. The specific sequence (usually counterclockwise) is based on the node numbering at the element level. The node numbering sequence for the elements shown in figure II.12 are presented in Table II.2 [34].

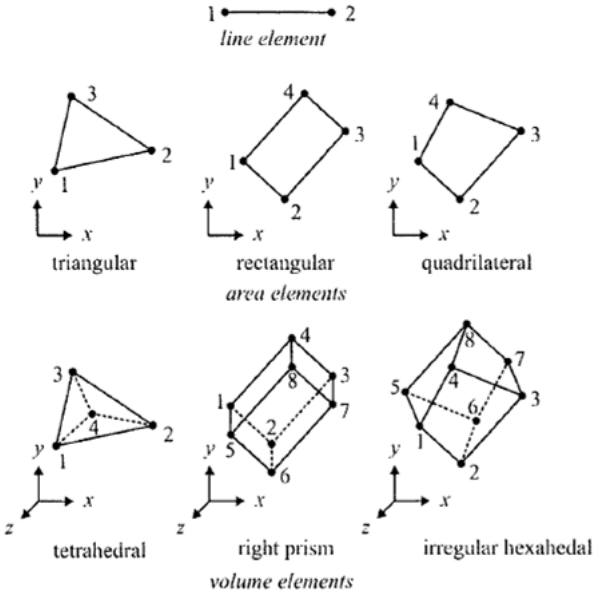

Figure II.11 line, area and volume elements description with node number at the element level.

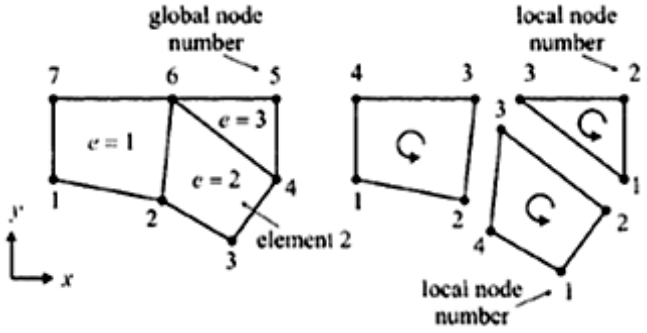

Figure II.12 discretization of a domain

Table II.2 description of numbering at the element level**.**

Element Number	Node 1	Node 2	Node 3	Node 4
1	1	2	6	7
2	3	4	6	2
3	4	5	6	

II.6.1.6 Element Attributes

Take finite elements of any kind one at a time. Their local properties can be developed by considering them in isolation, as individual entities. This is the key to the modular programming of element libraries. In the Direct Stiffness Method, elements are isolated by the disconnection and localization steps. The procedure involves the separation of elements from their neighbors by disconnecting the nodes, followed by referral of the element to a convenient local coordinate system.10 After that we can consider generic elements: a bar element,a beam element, and so on. From the standpoint of the computer implementation, it means that you can write one subroutine or module that constructs, by suitable parametrization, all elements of one type, instead of writing a new one for each element instance. Following is a summary of the data associated with an individual finite element. This data is used in finite element programs to carry out element level calculations.

(a) Element Dimensionality

Elements can have intrinsic dimensionality of one, two or three space dimensions. There are also special elements with zero dimensionality, such as lumped springs or point masses. The intrinsic dimensionality can be expanded as necessary by use of kinematic transformations. For example a 1D element such as a bar, spar or beam may be used to build a model in 2D or 3D space.

(b) Element Nodes

Each element possesses a set of distinguishing points called nodal points or nodes for short. Nodes serve a dual purpose: definition of element geometry, and home for degrees of freedom. When a distinction is necessary we call the former geometric nodes and the latter connection nodes. For most elements studied here, geometric and connector nodes coalesce. Nodes are usually located at the corners or end points of elements. In the so-called refined or higher-order elements nodes are also placed on sides or faces, as well as possibly the interior of the element.

(c) Element Geometry

The geometry of the element is defined by the placement of the geometric nodal points. Most elements used in practice have fairly simple geometries. In one-dimension, elements are usually straight lines or curved segments. In two dimensions they are of triangular or quadrilateral shape. In three dimensions the most common shapes are tetrahedra, pentahedra , and hexahedra .

(d) Element Degrees of Freedom

The element degrees of freedom (DOF) specify the state of the element. They also function as “handles” through which adjacent elements are connected. DOFs are defined as the values of a primary field variable at connector node points. Here we simply note that the key factor is the way in which the primary variable appears in the mathematical model. For mechanical elements, the primary variable is the displacement field and the DOF for many (but not all) elements are the displacement components at the nodes.

(e) Nodal Forces

There is always a set of nodal forces in a one-to-one correspondence with degrees of freedom. In, mechanical elements the correspondence is established through energy arguments.

(f) Element Constitutive Properties

For a mechanical element these are relations that specify the material behavior. For example, in a, linear elastic bar element it is sufficient to specify the elastic modulus E and the thermal coefficient of expansion α.

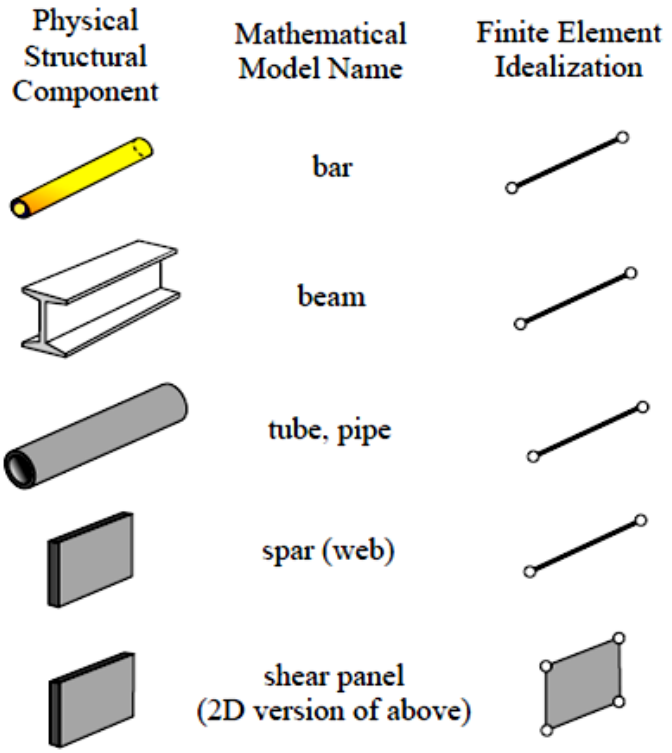

Figure II.13 primitive structural elements examples

(g) Element Fabrication Properties

For mechanical elements these are fabrication properties which have been integrated out from the element dimensionality. Examples are cross sectional properties of Mechanics of Materials elements such as bars, beams and shafts, as well as the thickness of a plate or shell element. For computer implementation the foregoing data sets are organized into data structures. These are used by element generation modules to compute element stiffness relations in the local system

(h) Classification of Mechanical Elements

The following classification of finite elements in structural mechanics is loosely based on the "closeness" of the element with respect to the original physical structure. It is given here because it clarifies points that recur in subsequent sections, as well as providing insight into advanced modeling techniques such as hierarchical breakdown and global-local analysis.

- **Primitive Structural Elements**

These resemble fabricated structural components. They are often drawn as such; see Figure II.14. The qualifier primitive distinguishes them from macro-elements, which is another element class described below.

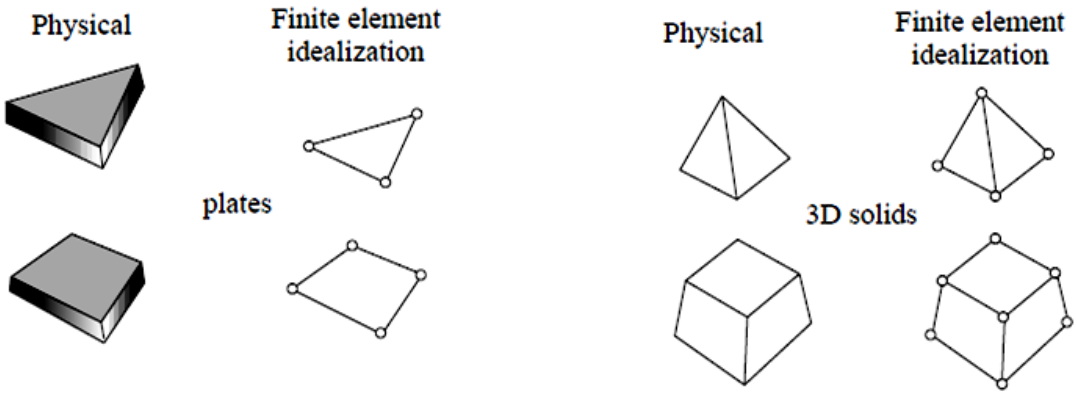

Figure II.14 examples of continuum element.

Primitive means that they are not decomposable into simpler elements. These elements are usually derived from Mechanics-of-Materials simplified theories and are better understood from a physical, rather than mathematical, standpoint. Examples are the elements.

- **Continuum Elements**

These do not resemble fabricated structural components at all. They result from the subdivision of “blobs” of continua, or of structural components viewed as continua. Unlike structural elements, continuum elements are better understood in terms of their mathematical interpretation. Examples: plates, slices, shells, axisymmetric solids, general solids. See figure II.15.

- **Special Elements**

Special elements partake of the characteristics of structural and continuum elements. They are derived from a continuum mechanics standpoint but include features closely related to the physics of the problem. Examples: crack elements for fracture mechanics applications, shear panels, infinite and semi-infinite elements, contact and penalty elements, rigid-body elements. See figure III.16.

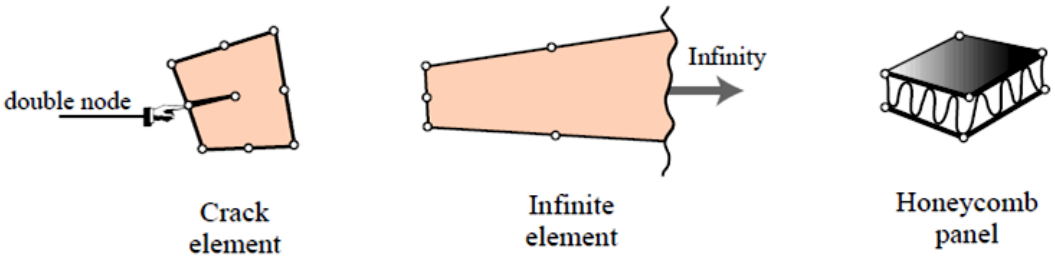

Figure II.15 special element examples.

- **Macro-elements**

Macro-elements are also called mesh units and super-elements, although the latter term overlaps with substructures (defined below). These often resemble structural components, but are fabricated with simpler elements. See Figure II.17. The main reason for introducing macro-elements is to simplify preprocessing tasks. For example, it may be simpler to define a regular 2D mesh using quadrilaterals rather than triangles. The fact that, behind the scene, the quadrilateral is actually a macro-element may not be important to most users.

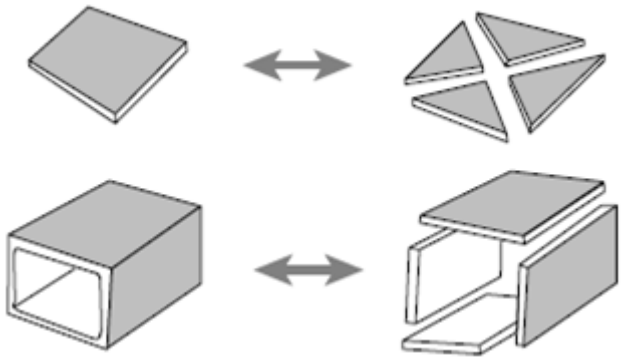

Figure II.16 Macro-element examples

Similarly a box macro-element can save modeling times for structures that are built by such components; for example box-girder bridges [36]

- ✓ **Meshes**

The meshes used for the numerical experiments are shown in Figures II.17-II.20. Here 3 levels of refinement are used for the h-refinement cases. Note that mesh 4 has a self-overlap, this mesh is used to show the robustness of the method. The higher degree results for h-refinement are obtained using a k-refinement strategy.

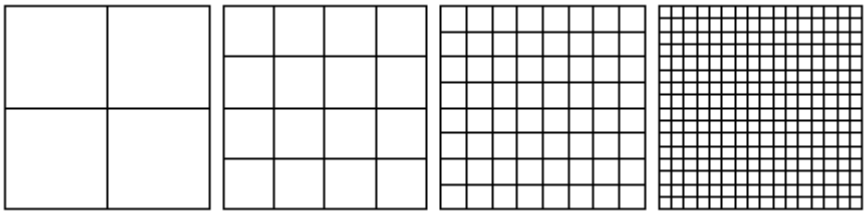

(a) mesh1 (b) mesh2 (c) mesh3 (d) mesh4

Figure II.17 refinement sequence for unit square.

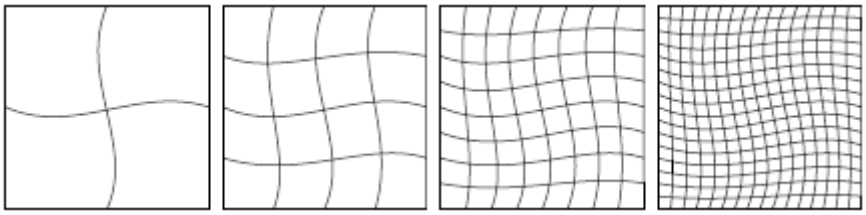

(a) mesh1 (b) mesh2 (c) mesh3 (d) mesh4

Figure II.18 refinement sequence for curvilinear1

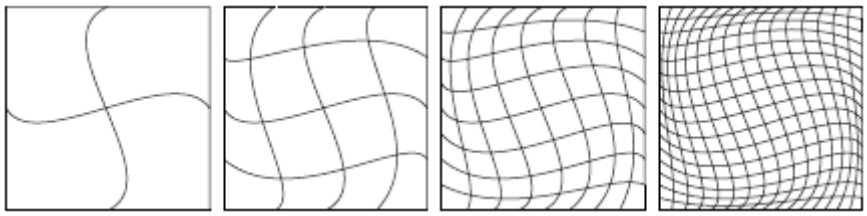

(a) mesh1 (b) mesh2 (c) mesh3 (d) mesh4

Figure II.19 refinement sequence for curvilinear2

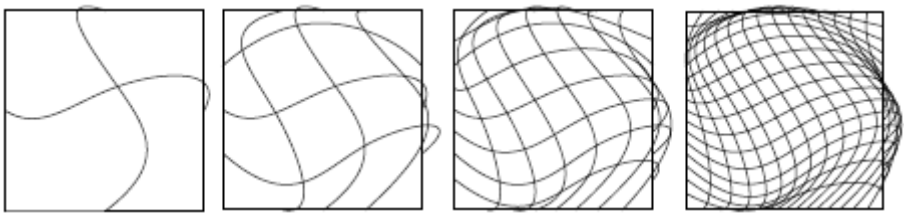

(a) mesh1 (b) mesh2 (c) mesh3 (d) mesh4

Figure II.20 refinement sequence for curvilinear1

Note further that the number of elements and thus the largest element circumdiameter stays constant for increasing order [37].

- **Substructures**

Also called structural modules and super-elements. These are sets of elements with a well defined structural function, typically obtained by cutting the complete structure into functional components. Examples: the wings and fuselage of an airplane; the towers, deck and cables of a suspension bridge. The distinction between substructures and macro-

elements is not clear-cut. The main conceptual distinction is that substructures are defined "top down" as parts of a complete structure, whereas macro-elements are built "bottom up" from primitive elements. The term super-element is often used in a collective sense to embrace element groupings that range from macro-elements to substructures.

(i) Assembly

The assembly procedure of the Direct Stiffness Method for a general finite element model follows rules identical in principle to those discussed for the truss example. As in that case the process involves two basic steps: Globalization. The element equations are transformed to a common global coordinate system, if necessary. Merge. The element stiffness equations are merged into the master stiffness equations by appropriate indexing and matrix-entry addition.

The hand calculations for the example truss conceal, however, the implementation complexity. The master stiffness equations in practical applications may involve thousands or even millions of freedoms, and programming can become involved.

(j) Boundary Conditions

A key strength of the FEM is the ease and elegance with which it handles arbitrary boundary and interface conditions. This power, however, has a down side. A big hurdle faced by FEM newcomers is the understanding and proper handling of boundary conditions. Below is a simple recipe for treating boundary conditions.

- **Essential and Natural B.C.**

The key thing to remember is that boundary conditions (BCs) come in two basic flavors: essential and natural. Essential BCs directly affect DOFs, and are imposed on the left-hand side vector **u**. Natural BCs do not directly affect DOFs and are imposed on the right-hand side vector **f**. For the moment, the basic recipe is:

1. If a boundary condition involves one or more degrees of freedom in a direct way, it is essential. An example is a prescribed node displacement.

2. Otherwise it is natural.

The term "direct" is meant to exclude derivatives of the primary function, unless those derivatives also appear as degrees of freedom, such as rotations in beams and plates.

- **B.C. in Structural Problems**

Essential boundary conditions in mechanical problems involve displacements (but not strain-type displacement derivatives). Support conditions for a building or bridge problem furnish a particularly simple example. But there are more general boundary conditions that occur in practice. Astructural engineer must be familiar with displacement B.C. of the following types. Ground or support constraints.Directly restraint the structure against rigid body motions.Symmetry conditions. To impose symmetry or antisymmetry restraints at certain points, lines or planes of structural symmetry. This allows the discretization to proceed only over part of the structure with a consequent savings in modeling effort and number of equations to be solved. An example are rotational degrees of freedom normal to smooth shell surfaces. Connection constraints. To provide connectivity to adjoining structures or substructures, or to specify relations between degrees of freedom. Many conditions of this type can be subsumed under the label multipoint constraints or multifreedom constraints. These can be notoriously difficult to handle from a numerical standpoint [38].

II.6.1.7 The application of FEM in CAD (Computer Aided Design)

Current systems, especially for mechanical products are 3D systems and they are spreading now their dominance to the other sectors. In this part we will speak about the concept of designand modeling**.** These are mainly surface modeling systems for mechanical products, with very good rendering capabilities. The process usually starts with a rough sketch of the blade, figure II.21 (a), you can create the 3D model from the 2d sketches and then use advanced photo-realistic rendering and animation to further evaluate, present and sell the concepts, figure II. 21 (b).

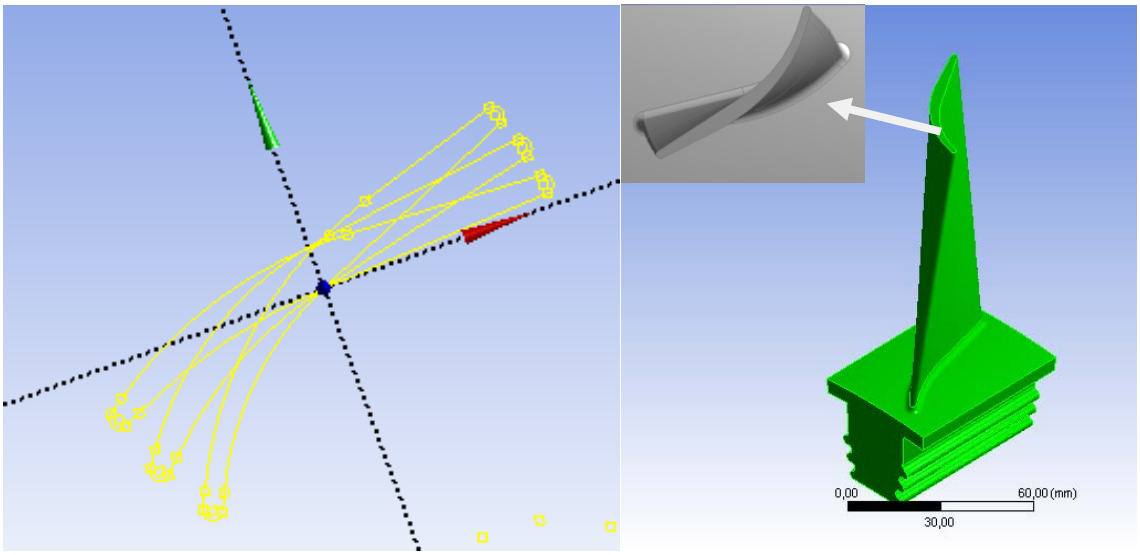

(a) (b)

Figure II.21 (a) Sketch the product, (b) Rendering of the 3D Model.

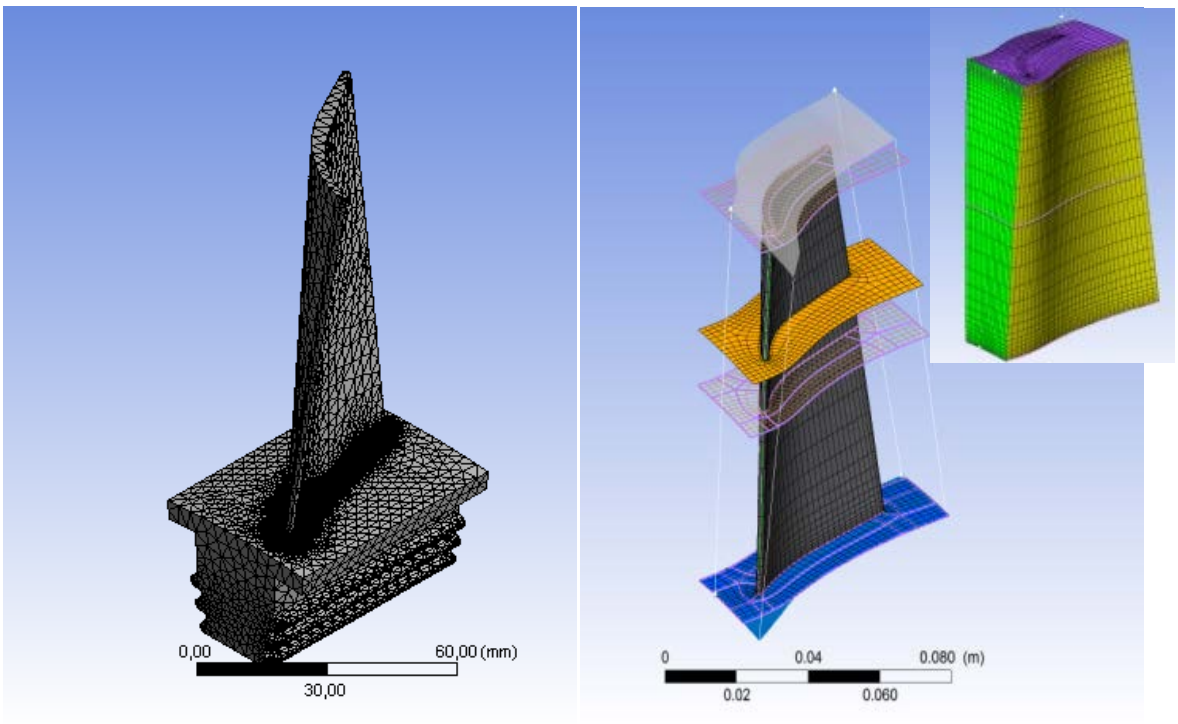

(a) (b)

Figure II.22.The Gas turbine blade model. (a) Structural mesh, (b) Meshed used for CFD.

In Figure II.22 (a) we used the tetrahedron mesh because of the creation of crack that's demanded this type of meshing (fracture meshing supports quadratic tetrahedron elements only). But for the CFD (Fig. II.22 (b)) mesh it's automatically taken by using turbogrid that's give us this type of mesh.

For confirming that our mesh is the right mesh we do a test by increasing the mesh (elements and nodes) that's shown in table.II.3 and Figure II.23

Table II.3 Mesh test values with Max stress

Mesh number	1	2	3	4	5	6
nodes	63584	151600	600879	902208	1632070	1910718
Elements	41845	104399	423715	637450	1156589	1354851
Max stress (MPa)	94.073	98.273	101,99	101,991	101,991	101,991

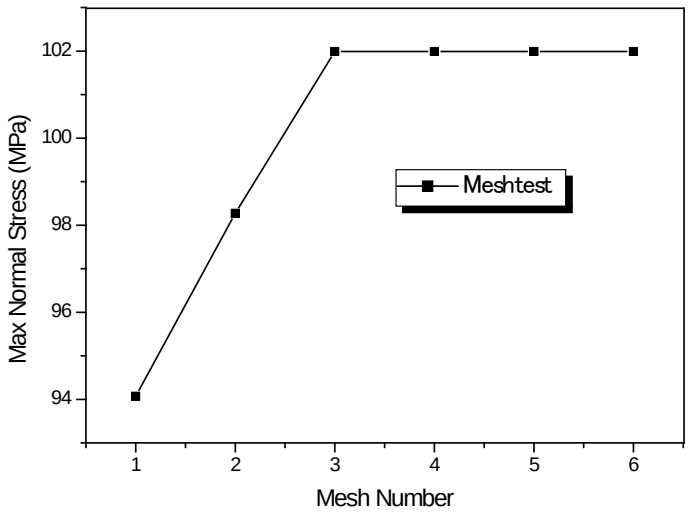

Figure II.23 curve of the Mesh test

After mesh test this result of normal stress (σ_{xx}) has been grow form mesh 1 to mesh 3 and after that the Max Stress has been stabilized in 101, 99 MPa. In the next chapter we go to see the results of this simulation.

II.6.1.8 Advantages of the Finite Element Method

The finite element method has been applied to numerous problems, both structural and nonstructural. They include the ability to:

1. Complex form means irregularly shaped systems
2. Using any kind of load conditions
3. Using a lot of model of systems composed many materials
4. Using unlimited numbers and types of boundary conditions
5. It is able to change the size of element for any condition
6. The finite element method can be used for any situation 1D, 2D or 3D which depend the geometry of system
7. Taking into consideration the effects of static and dynamic for each phenomenon
8. It is very important to note that the nonlinear behavior depending on the deformations.
9. The finite element method is not only suitable for the mechanical domains but also accepts for medicine fields

II.6.1.9 Disadvantages of the Finite Element Method

It is complex to applied FEM for flow fluid applications such as Newtonian or Non-Newtonian fluids. It has been applied only for special problems. Thus, the importance of FEM depends only for the structures such as ordinary or composite.

References

[1] Wilders, P., Fox, P., Ecer, A., Satofuka, N. and Periaux, J. eds., 2002. Parallel Computational Fluid Dynamics 2001, Practice and Theory. Elsevier. ASIN : B00PIREMC2

[2] Anderl, Reiner, and Peter Binde. Simulations with NX. Munich, Carl Hanser Verlag, 2014. ISBN 978-1-56990-479-4 E-Book ISBN 978-1-56990-480-0

[3] Nompelis, I., Drayna, T.W. and Candler, G.V., 2006. A parallel unstructured implicit solver for hypersonic reacting flow simulation. In Parallel Computational Fluid Dynamics 2005 (pp. 389-395). Elsevier. doi.org/10.1016/B978-044452206-1/50047-1

[4] Deane, A., Brenner, G., Emerson, D.R., McDonough, J., Tromeur-Dervout, D., Satofuka, N., Ecer, A. and Periaux, J. eds., 2006. Parallel Computational Fluid Dynamics 2005: Theory and Applications. Elsevier.ISSN1570-9426.

[5] Jamshed, Shamoon. Using HPC for Computational Fluid Dynamics: A Guide to High Performance Computing for CFD Engineers. Academic Press, 2015. Accession NumberADA375601

[6] Ledesma, D.S., 2020. A local solution to the Navier–Stokes equations on manifolds via stochastic representation. Nonlinear Analysis, 198, p.111927. doi.org/10.1016/j.na.2020.111927

[7] Li, X. and Li, L.A., 2020. Vanishing viscosity limit to the planar rarefaction wave for the two-dimensional full compressible Navier-Stokes equations. Journal of Differential Equations. doi.org/10.1007/s00220-019-03580-8

[8] Liu, Z., 2020. Algebraic decay of weak solutions to 3D Navier-Stokes equations in general unbounded domains. Journal of Mathematical Analysis and Applications, p.124300. doi.org/10.1016/j.jmaa.2020.124300

[9] Dong, L., 2020. Strong solutions for the stochastic Navier-Stokes equations on the 2D rotating sphere with stable Lévy noise. Journal of Mathematical Analysis and Applications, p.124182.

[10] Craig, K.J., Nieuwoudt, M.N. and Niemand, L.J., 2013. CFD simulation of anaerobic digester with variable sewage sludge rheology. Water research, 47(13), pp.4485-4497. doi.org/10.1016/j.watres.2013.05.011

[11] Vakamalla, T.R. and Mangadoddy, N., 2015. Rheology-based CFD modeling of magnetite medium segregation in a dense medium cyclone. Powder Technology, 277, pp.275-286. http://dx.doi.org/10.1016/j.powtec.2015.02.025

[12] Hou, W., Zhang, L., Zhang, J. and Bao, J., 2016. Rheology evolution and CFD modeling of lignocellulose biomass during extremely high solids content pretreatment. Biochemical Engineering Journal, 105, pp.412-419. DOI: 10.1016/j.bej.2015.10.021

[13] Hicks, C.I., See, H., Fletcher, D.F. and Ekwebelam, C., 2012. The shear rheology of bread dough: Analysis of local flow behaviour using CFD. Food and Bioproducts Processing, 90(3), pp.361-369. doi.org/10.1016/j.fbp.2012.01.001

[14] Joel H. FerzigerMilovan PerićRobert L. Street, 2020. Computational Methods for Fluid Dynamics Fourth edition, Springer Nature Switzerland AG 2020. doi.org/10.1007/978-3-319-**99693**-6

[15] Bird, R. Byron, and John M. Wiest. "Constitutive equations for polymeric liquids." Annual review of fluid mechanics 27.1 (1995): 169-193. Copyright © 1995 by Annual Reviews Inc. All rights reserved

[16] Tabbakh, Z., Seaid, M., Ellaia, R., Ouazar, D. and Benkhaldoun, F., 2019. A local radial basis function projection method for incompressible flows in water eutrophication. Engineering Analysis with Boundary Elements, Volume 106, September 2019, Pages 528-540

[17] Denner, F., Evrard, F. and van Wachem, B.G., 2020. Conservative finite-volume framework and pressure-based algorithm for flows of incompressible, ideal-gas and real-gas fluids at all speeds. Journal of Computational Physics, p.109348. doi:10.1016/j.jcp.2020.109348

[18] Avancini, G. and Sanches, R.A., 2020. A total Lagrangian position-based finite element formulation for free-surface incompressible flows. Finite Elements in Analysis and Design, 169, p.103348. https://doi.org/10.1016/j.finel.2019.103348

[19] Daryl L. Logan, A First Course in the Finite Element Method , Thomson, 2007,USA.

ISBN 0534552986, 9780534552985

[20] Kendall E. Atkinson, book (Numerical analysis), University of Iowa, Iowa City, Iowa, 2007.USA. ISBN 0-471-62489-6

[21] Tu, Jiyuan, Guan Heng Yeoh, and Chaoqun Liu. Computational fluid dynamics: a practical approach. Butterworth-Heinemann, 2018. ISBN-13: 978-0081011270

[22] Evans, G., Blackledge, J. and Yardley, P., 2012. Numerical methods for partial differential equations. Springer Science & Business Media. ISBN978-1-4471-0377-6

[23] Ames, W.F., 2014. Numerical methods for partial differential equations. Academic press.ISBN 10-1483235505

[24] Mazumder, S., 2015. Numerical methods for partial differential equations: finite difference and finite volume methods. Academic Press. ISBN: 9780128035047

[25] McDonald PW. (1971). The computation of transonic flow through two-dimensional gas turbine cascades, ASME Paper 71-GT-89,Gas Turbine Conference and Products Show, Houston. doi.org/10.1115/71-GT-89

[26] MacCormak RW, Paullay AJ. (1972). Computational efficiency achieved by time splitting of finite difference operators,AIAA Paper 72-154.

[27] Rizzi AW, Inuoye M. (1973). Time split finite volume method for 3D blunt body flows,AIAA J., 11:1478–1485. doi.org/10.2514/6.1973-133

[28] Kim, J., Kim, D. and Choi, H., 2001. An immersed-boundary finite-volume method for simulations of flow in complex geometries. Journal of computational physics, 171(1), pp.132-150. doi.org/10.1007/BF02990875

[29] Moukalled, F., Mangani, L. and Darwish, M., 2016. The finite volume method in computational fluid dynamics (Vol. 6). Berlin, Germany:: Springer. ISBN 978-3-319-16874-6

[30] Dr Nicos Bilalis,Report Produced For The EC Funded Project, INNOREGIO: Dissemination Of Innovation And Knowledge Management

Techniques, Technical University Of Crete, january 2000. https://www.academia.edu/32686097

[31] J.H. Argyris and S. Kelsey, (Energy Theorems and Structural Analysis), Aircraft Engineering, Vol. 27, 1955. http://www.ce.memphis.edu/7117/notes/presentations/papers/Argyris1954-P1.

[32] T. A. Stolarski,Y. Nakasone And S. Yoshimoto,"Engineering AnalysisWith ANSYS® Software", Department Of Mechanical Engineering School Of Engineering And Design Brunel University,Middlesex, Uk,Department Of Mechanical Engineering Tokyo University Of Science, Tokyo, Japan , First published 2006 ISBN 978-0-7506-6875-0

[33] saeed Loaveni,Finite Element Analysis,Theory And Applications With ANSYS®, 1999,By Laxxuss, ISBN 0-13-785098-0.ISBN013-785098-0

[34] Niko Manopulo,Seminar: Interplay of Mathematical Modeling and Numerical Simulation An Introduction to Finite Element Methods, JASS 05,May 4, 2005.

http://wwwmayr.in.tum.de/konferenzen/Jass05/courses/2/Manopulo/Manopulo_paper.

[35] Madenci,Erdogan, and Ibrahim Guven. The finite element method and applications in engineering using ANSYS®. Springer, 2015. ISBN 978-1-4899-7550-8

[36] . FEM Modeling: Introduction CH 6 http://kis.tu.kielce.pl/mo/COLORADO_FEM/colorado/IFEM.Ch06.pdf

[37] Dennis Ernens, Finite Element Methods with exact geometry representation IsoGeometric Analysis, NURBS Enhanced Finite Element Method and AnisoGeometric Analysis, November 4, 2011. DOI: 10.13140/RG.2.1.1054.6326

[38] Felippa, Carlos A. "Introduction to finite element methods." University of Colorado 885 (2004).

CHAPTER III

Results and Discussions

III.1 Failure Turbine

III.1.1 Numerical study and software analysis

In this numerical study, the interaction between flow/structure analyses was carried out by ANSYS® software. In the computational fluid dynamics Software CFD part, we use steady state gas flow in three-dimensional, this code solves the Reynolds-averaged Navier−Stokes equations in stationary and rotating coordinates. In regard to the turbulence modeling, using k-ε realisable model at different blowing ratios, and in the structural part an isotropic, elastic material and with static state.

The rotor of this turbine have a external diameter D_{ext}=700 mm , internal diameter D_{int}=500 mm and blade length L=100 mm, this turbine had 61 blades , a complete modeling solution took a long time, one blades of rotor are modeled with consideration of correct boundary conditions (Figure III (1.a)).

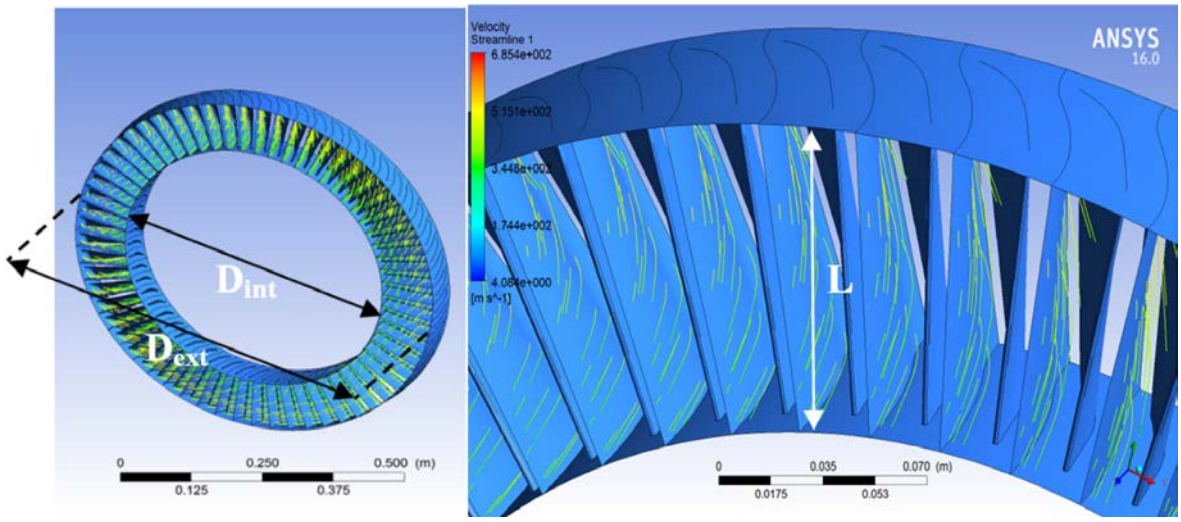

(a) (b)

Figure III.1: (a) Geometry size and proprieties of our rotor stage (b) magnification of blade geometry.

Table III.1. Chemical composition of Inconel 718 alloy [1].

Ni+Cr	Cr	Mo	Nb+Ta	Ti	Al	Fe
53,7	17,9	2,9	5,22	1,0	0,49	18,79

Pressure distribution showed consistence with real conditions (Figure III (1.b)) and our blade it's from Inconel 718 alloy used in industry of gas turbine It provides superior abrasion, high temperature and chemical resistance. This material has an excellent cost-to part life performance record. (table III.1) [1].

In any gas turbine module, we have in the first stage the rotor are connected to the central shaft and rotate at high speed. And the Other rows, called stators, are fixed and do not rotate. The job of the stators is to keep the flow from spiraling around the axis by bringing the flow back parallel to the axis.

III.2 RESULTS AND DISCUSSIONS

This study is divided in two parts; the first is the CFD software and the second is the structural analyses. In the part of CFD, the blades are meshed with TurboGrid^{TM} software taking account the CFX software is the aim to put the boundary condition, analyze and get the pressure.

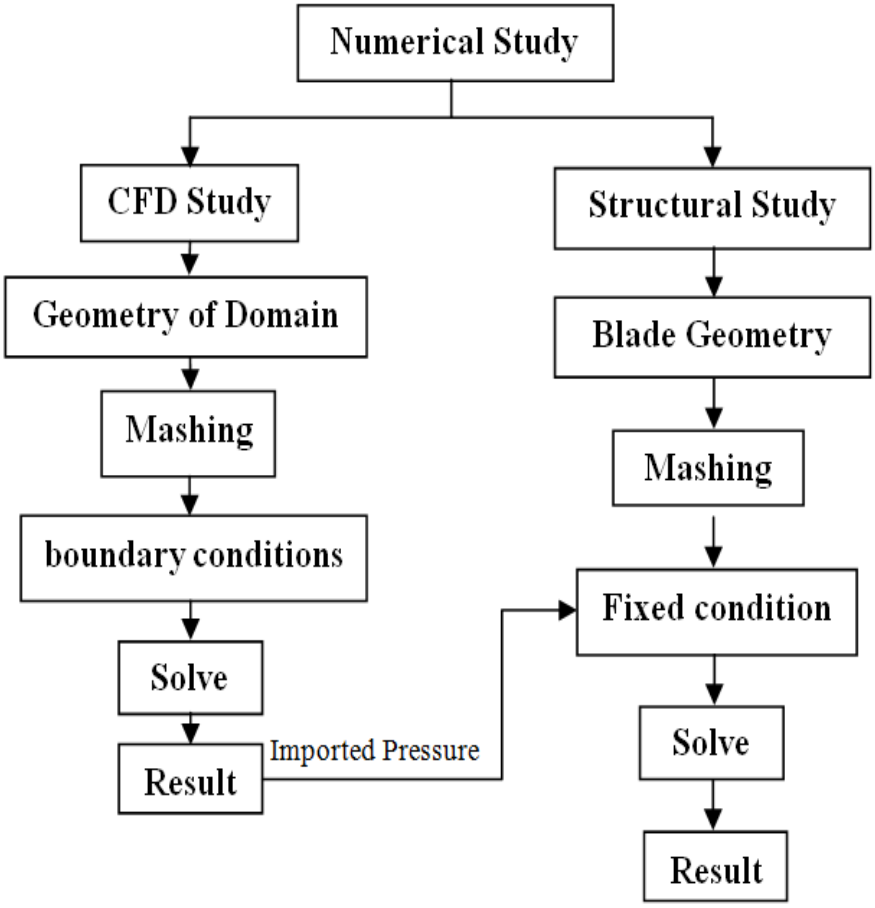

Figure III.2: Flowchart of fluid/solid interaction.

The last imported with our blade body with fixing tree root to get finally as result normal stress and von misses. In the next parts of our study we'll show you more details of the analysis. The figure III.2 shows the Flow chart of solid fluid interaction.

III.2.1 CFD Study

In the fluid part we used CFD ANSYS®software advanced for our study, however, the applied boundary conditions follow a classical scheme for incompressible and low Mach number flow simulations.

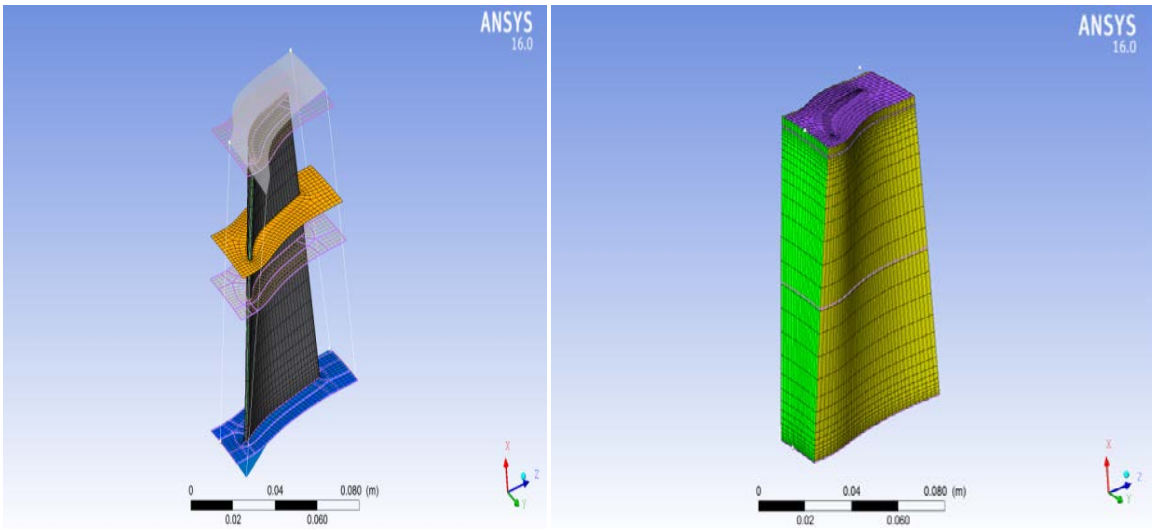

(a) (b)

Figure III.3: Domain meshing used, (a) domain inside, (b) domain outside

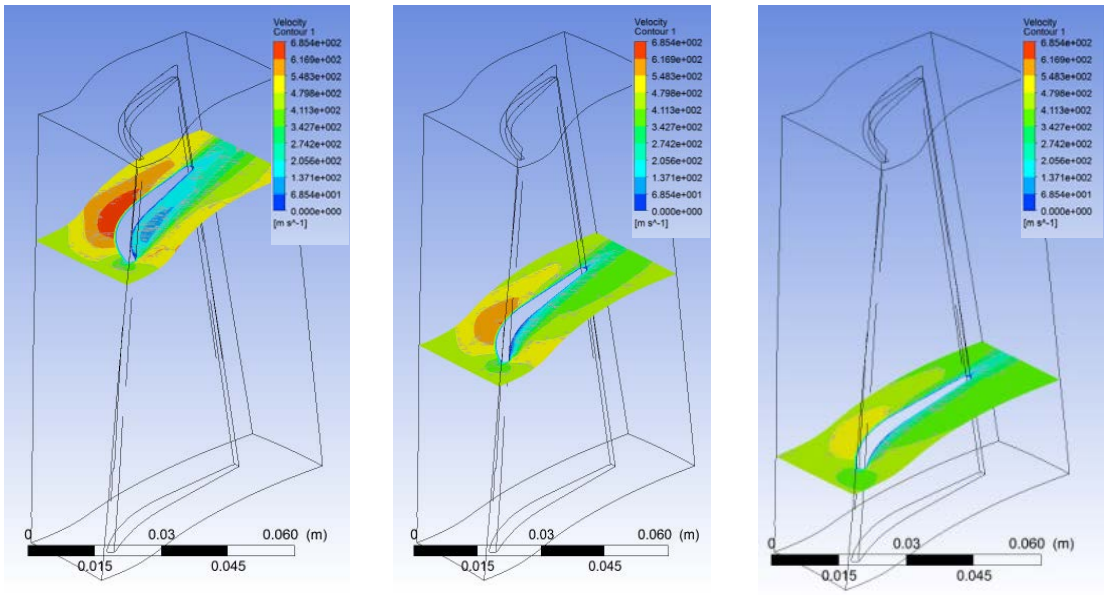

(a) (b) (c)

Figure III.4: Example of the velocity distribution for (a) z=75 mm, (b) z=50 mm, (c) z=25 mm.

A constant velocity is imposed at the inlet surface while ambient static pressure (101 GPa) is maintained at both outlet sections. In inlet air flow speed 300 m/s and outlet pressure is 200 GPa. The figure III.3 present the domain meshed by TurboGrid. The Forth & fifth figure represents the contour of velocity of flow and pressure in the blade surface . And in the Fig.III.4, the obtained maximum value of apply pressure is about 0.355 MPa. In literature we have many authors valid our results.

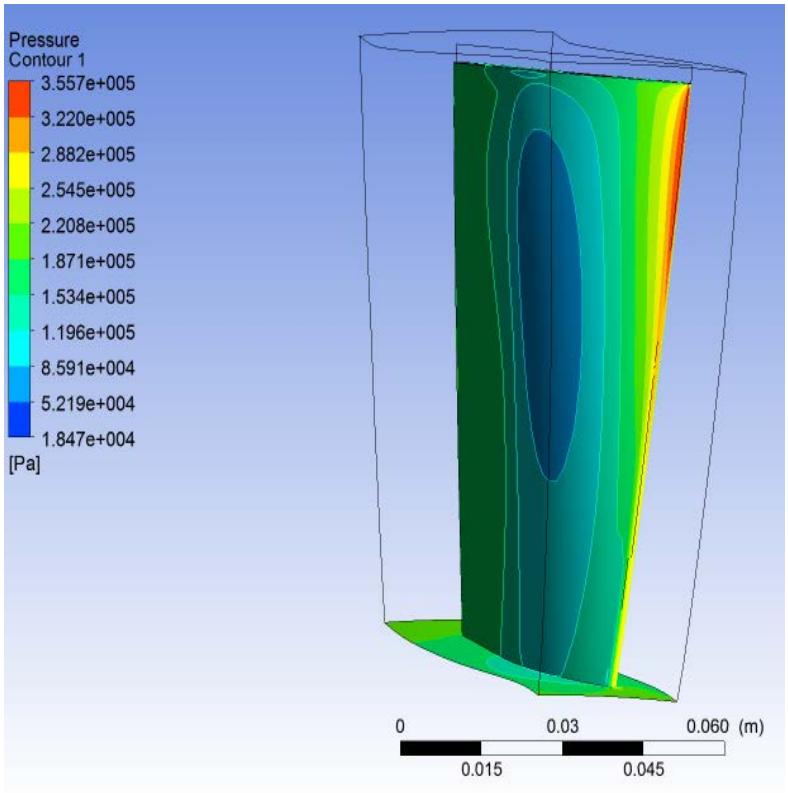

Figure III.5: Global contour pressure distribution.

Volkov et al.[2] find a maximum pressure value at 0.334 MPa, in other paper we have the work of S.A. Moshizi et al. [3], this author studied the effect of the viscosity (viscous and inviscid) flow fields of a gas turbine blade cascade on the pressure and section sides of the blade, this maximum pressure value is 0.383 MPa, this value validated with ANSYS® FLUENT User's Guide (0.382 MPa). Wang Peil et al.[4], he study Heat Transfer and Aerodynamics of Complex Shroud Leakage Flows in a Low-Pressure Turbine and find the pressure value 0.225 MPa. Rashidzadeh et al. [5], in his study of The SGT-600 industrial twin-shaft gas turbine modeling for mechanical drive applications at the steady state conditions the pressure rate to 0.15 MPa as max. And The American Petroleum Institute.[6], in his General-Purpose Steam Turbines for Petroleum, Chemical, and Gas Industry Services have make the maximum pressure of work ≥ 0,7.

III.2.2 Structural study

In the Structural study, the geometry of our blade is presented in Figure III.6.(a). With the meshing used, the blade meshed that's show in Figure III.6.(b). In the boundary condition we have fixed the three root of our blade (Ux=Uy=Uz=0), the loading pressure is imported from the CFD result to blade body.

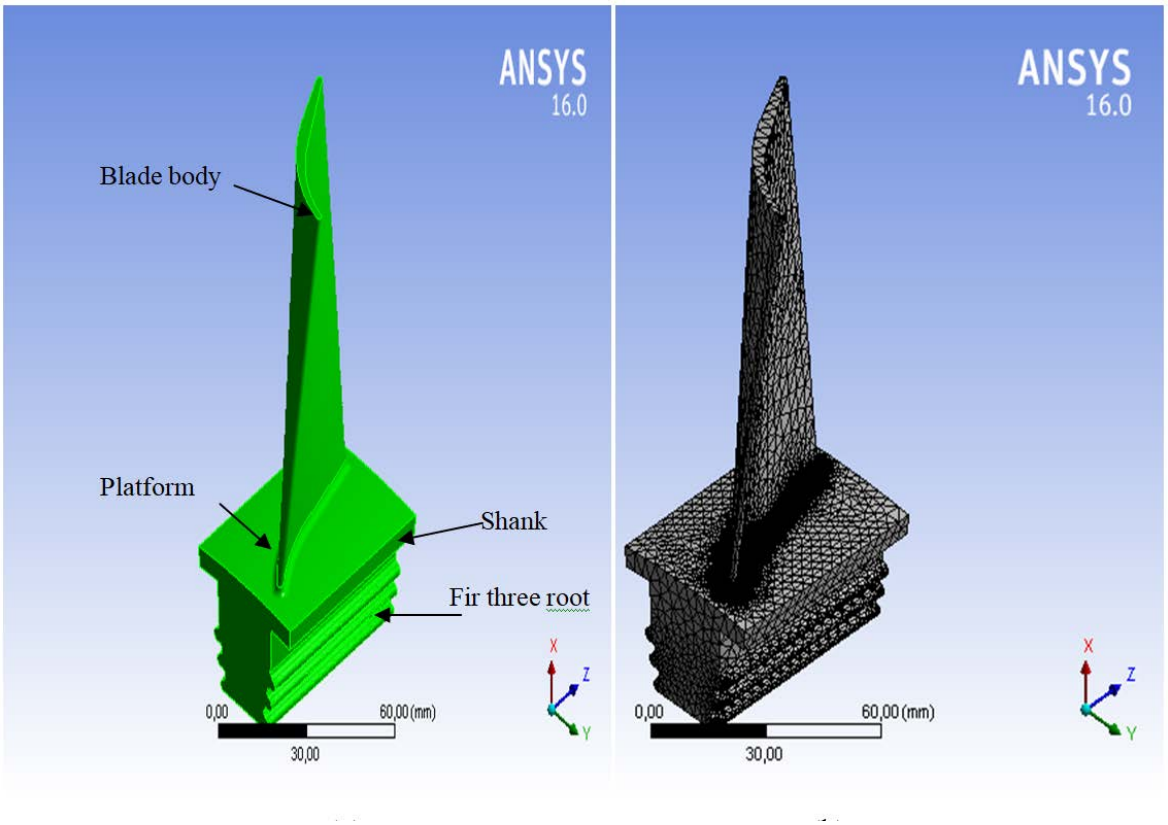

(a) (b)

Figure III.6: The Gas turbine blade model. (a) Structural module, (b) Meshed used.

That's showed down in Figure III.7. And the blades of the turbine are twisted, the blades have stagger angle that is greater at the tip than at the root. Because twist makes the gas flow from the combustion system do equal work at all positions along the length of the blade and to ensure that the flow enters the exhaust system with a uniform axial velocity [7].

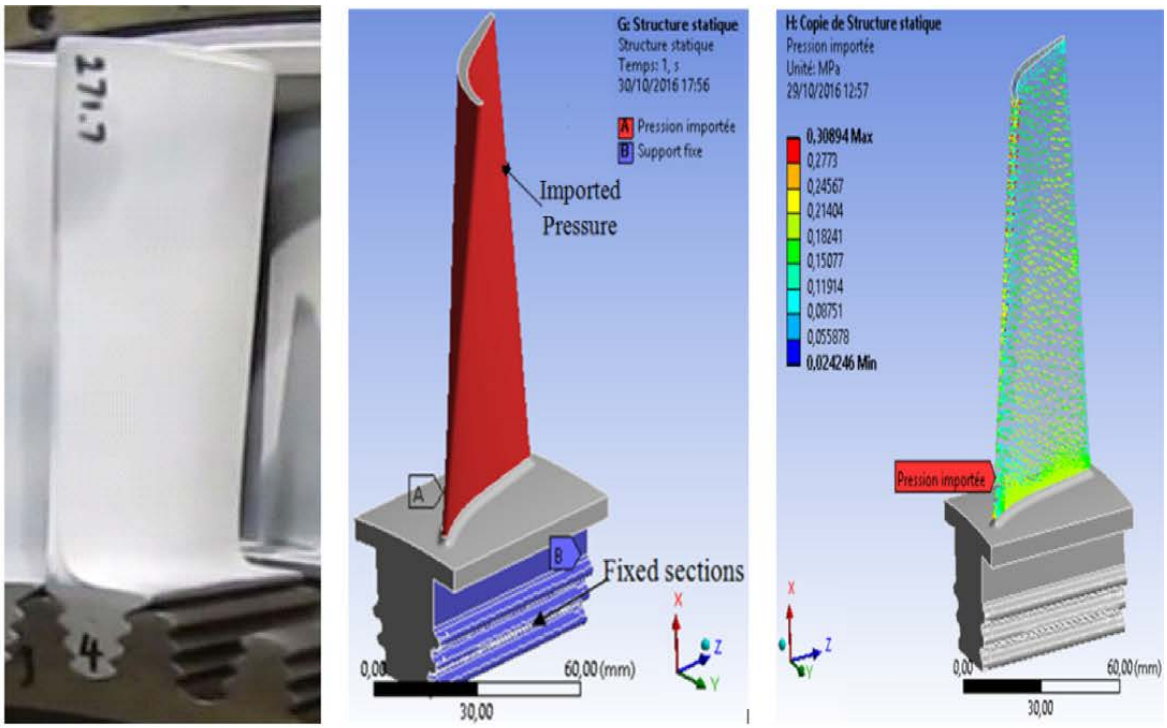

(a) (b) (c)

Figure III.7: Geometric used with the boundary condition, (a) blade fixation, (d) blade boundary condition, and (e) imported pressure.

The critical region or the crack zone is region in which maximum normal stress occurs, in the Figure .III.8 showed their normal stress (or principal stress) in deferent axes (X,Y and Z), we have a max stress in X direction with a 101.99 MPa value.

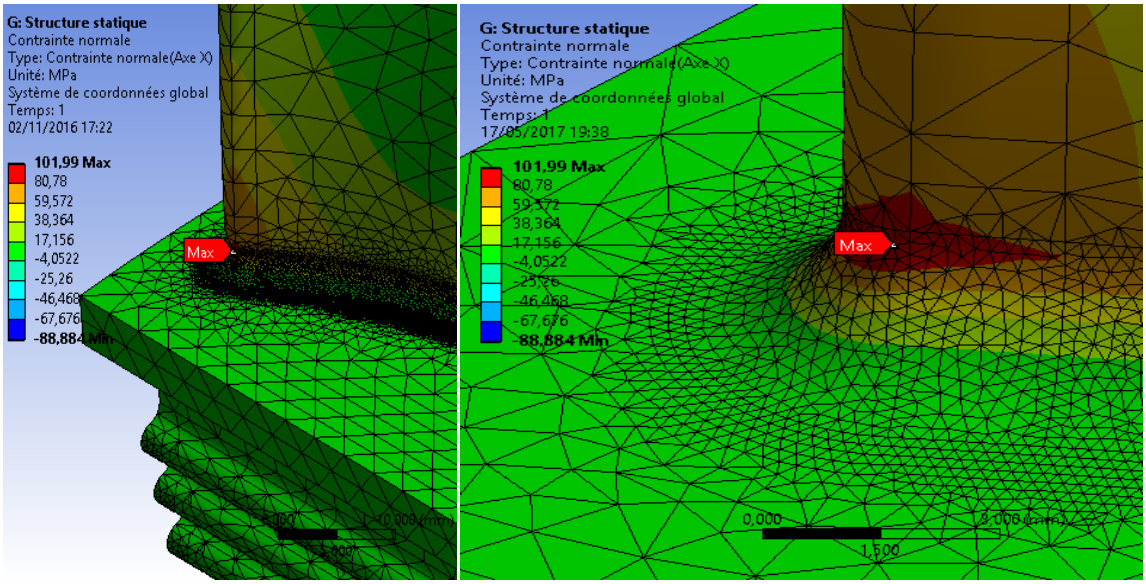

(a)

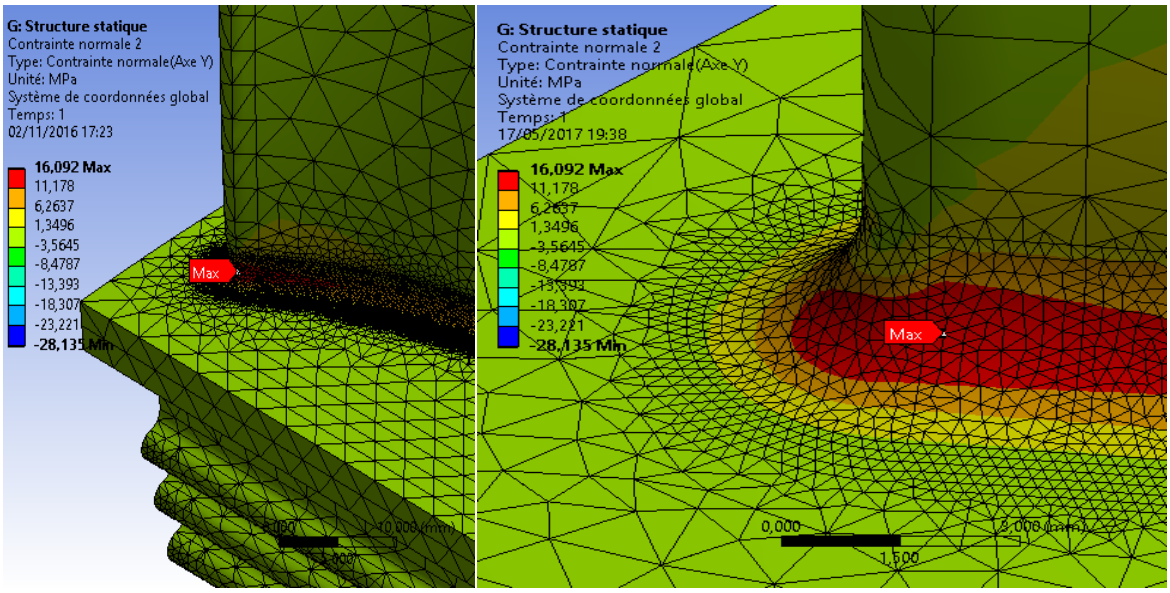

(b)

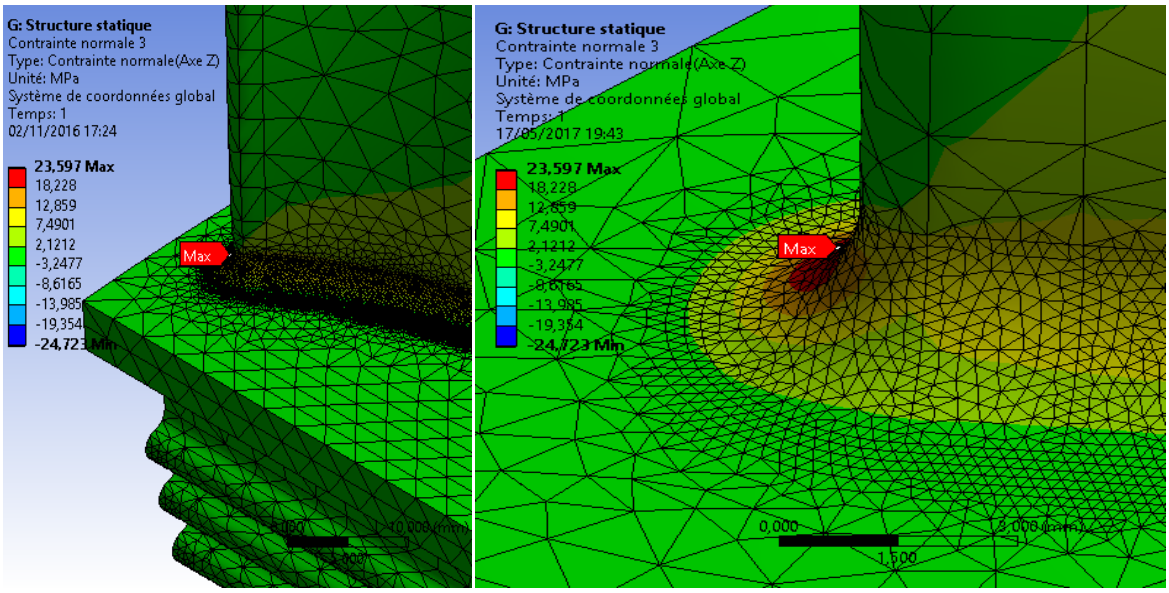

(c)

Figure III.8: Maximum normal stress in (a) X, (b) Y, (c) Z.

The normal stress occurs near the platform at for three regions. The location of maximum normal stress shows the fillet region at the intersection of blade and root subjected. This area would be the most susceptible to the crack. In the next part, we create a little crack in the node where we have a maximum value of normal stress between them (Figure III.8.(a)). This result validate by the work of [8].

III.2.3 Creation of the crack in the leave of the blade

After studying the maximum stress of the blade, and taking it as a point of crack. We will propagate step by step. In order to study the direction of the crack. we choose semi-elliptical crack according a several authors have been suggested that the damage severely of compressor of a gas turbine due to the failure of blade and the observation showed that a serious pitting was occurred to the blade surfaces and there were evidences of fatigue marks a semi-elliptical fracture surface Figure .III.9.

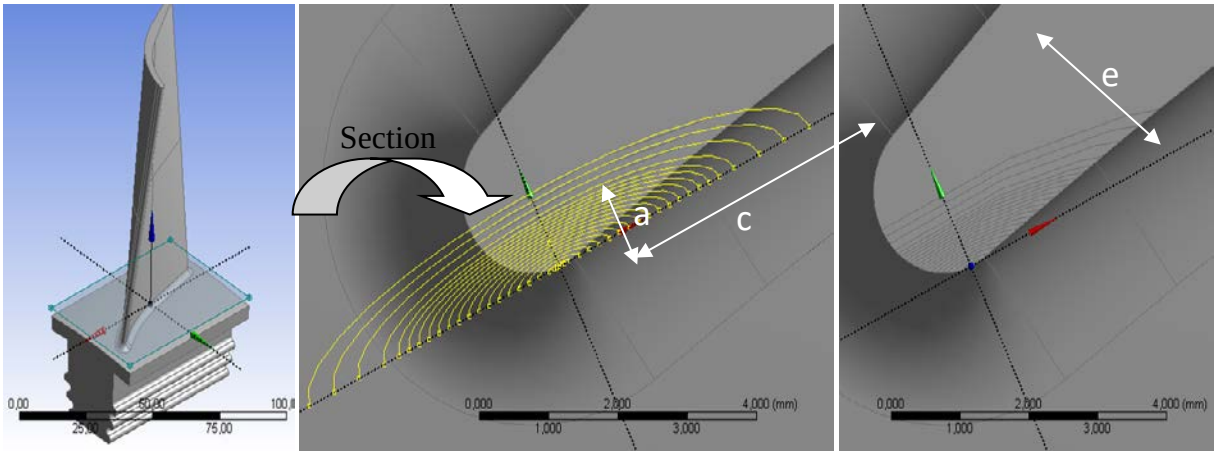

Figure III.9: Crack section presentation.

The propagation of an initial semi-elliptical crack were generated in two parameter crack propagation space (a/c, a/e) as shown in Figure III.9. On the node where we have a maximum normal stress,the shape transition of the crack surface during propagation i.e. from a surface to a corner and finally to an edge shape. In the Figure .III.9 shows the crack front evolution during simulation along with the transition of the crack front shape through the edges of the solid model.

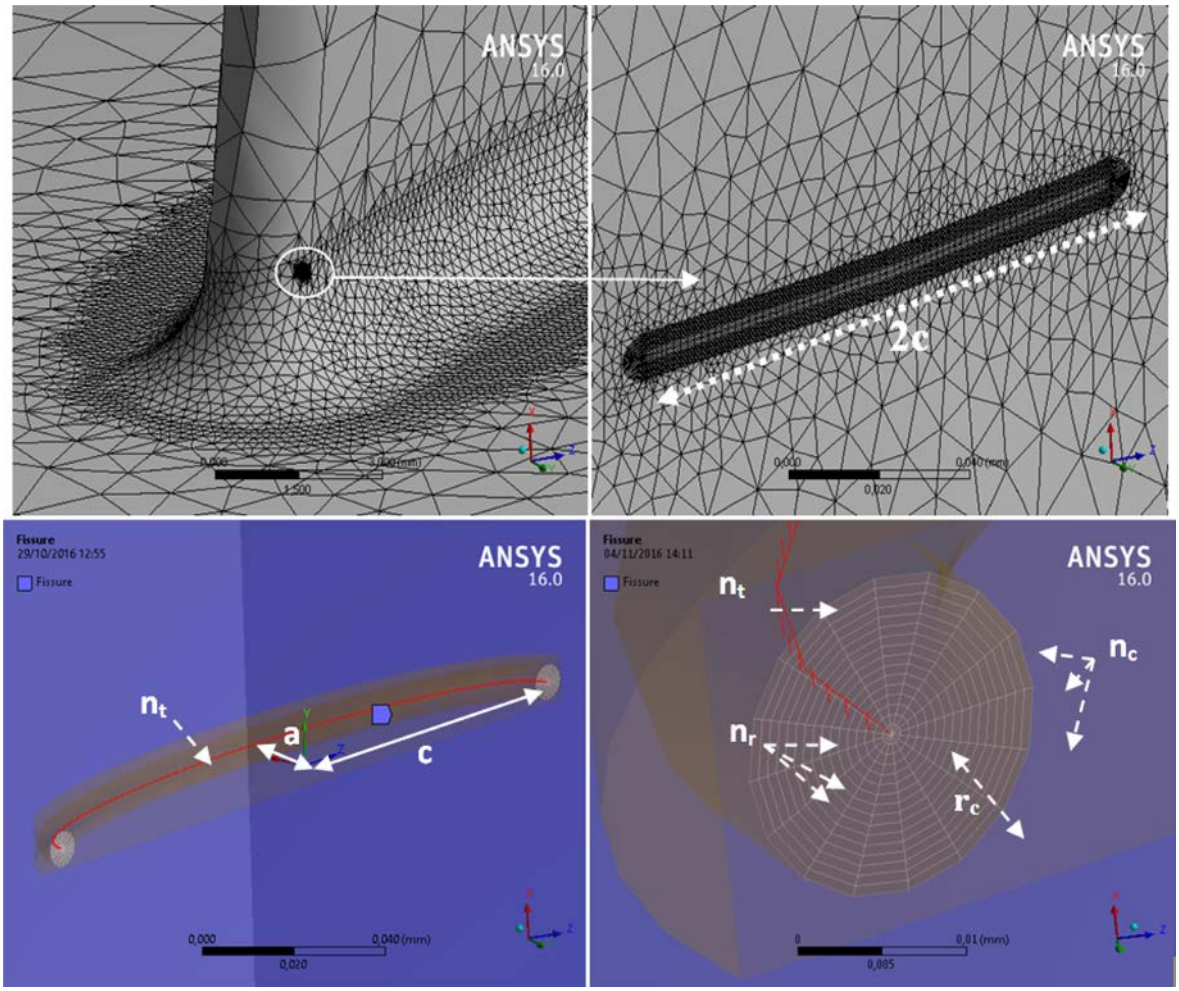

Figure III.10: Semi-elliptical crack meshing characterization.

Figure III.10 showed the semi-elliptical crack with a depth a, length c, and meshed proprieties: meshing circumferential radius r_c=0.01 mm, circumferential division n_c=16, radial division n_r=16 and the crack tip division n_t=91

III.2.4 Stress Intensity Factor on the crack distribution

Since linear elastic fracture mechanic principles are not applicable to surface interception points, stress intensity factor at those points is to be neglected and the preceding points can be considered, from Figure III.11 it is seen that surface interception .at the crack depth is subjected to mixed mode I , II and III. The stress field's distribution at near of the crack tip is very important, because these fields govern the fracture process that takes place at the crack tip. In this section we shall make a thorough study of the stresses near the crack tip for the three deformation modes.

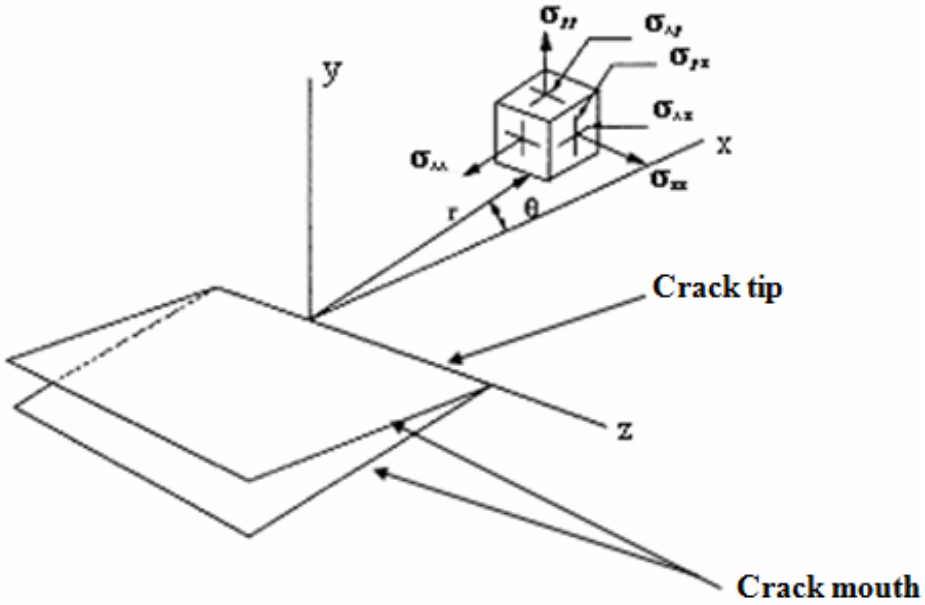

Figure III.11: Stress Field in the vicinity of the crack.

(a) Opening mode

The stresses near the crack tip are

$$\sigma_x = \frac{K_I}{\sqrt{2\pi R}}\cos\left(\frac{\theta}{2}\right)\left(1-\sin\left(\frac{\theta}{2}\right)\sin\left(\frac{3\theta}{2}\right)\right) \quad \text{(III.1a)}$$

$$\sigma_y = \frac{K_I}{\sqrt{2\pi R}}\cos\left(\frac{\theta}{2}\right)\left(1+\sin\left(\frac{\theta}{2}\right)\sin\left(\frac{3\theta}{2}\right)\right) \quad \text{(III.1b)}$$

$$\sigma_{xy} = \frac{K_I}{\sqrt{2\pi R}}\cos\left(\frac{\theta}{2}\right)\sin\left(\frac{\theta}{2}\right)\cos\left(\frac{3\theta}{2}\right) \quad \text{(III.1c)}$$

(b) Sliding mode

The stresses near the crack tip are

$$\sigma_x = -\frac{K_{II}}{\sqrt{2\pi R}}\sin\left(\frac{\theta}{2}\right)\left(2+\cos\left(\frac{\theta}{2}\right)\cos\left(\frac{3\theta}{2}\right)\right) \quad \text{(III.2a)}$$

$$\sigma_y = \frac{K_{II}}{\sqrt{2\pi R}}\sin\left(\frac{\theta}{2}\right)\cos\left(\frac{\theta}{2}\right)\cos\left(\frac{3\theta}{2}\right) \quad \text{(III.2b)}$$

$$\sigma_{xy} = \frac{K_{II}}{\sqrt{2\pi R}} \cos\left(\frac{\theta}{2}\right)\left(1 - \sin\left(\frac{\theta}{2}\right)\sin\left(\frac{3\theta}{2}\right)\right) \quad \text{(III.2ac)}$$

(c) Tearing mode

$$\sigma_{xz} = -\frac{K_{III}}{\sqrt{2\pi R}} \sin\left(\frac{\theta}{2}\right) \quad \text{(III.3a)}$$

$$\sigma_{yz} = \frac{K_{III}}{\sqrt{2\pi R}} \cos\left(\frac{\theta}{2}\right) \quad \text{(III.3b)}$$

Where the subscripts x, y and z suggests a local Cartesian co-coordinate system formed by the plane normal to the crack front and the plane tangential to the crack front point; r and θ are the local polar co-ordinates, K_I, K_{II} and K_{III} is the stress intensity factor for mode I, II and III respectively.

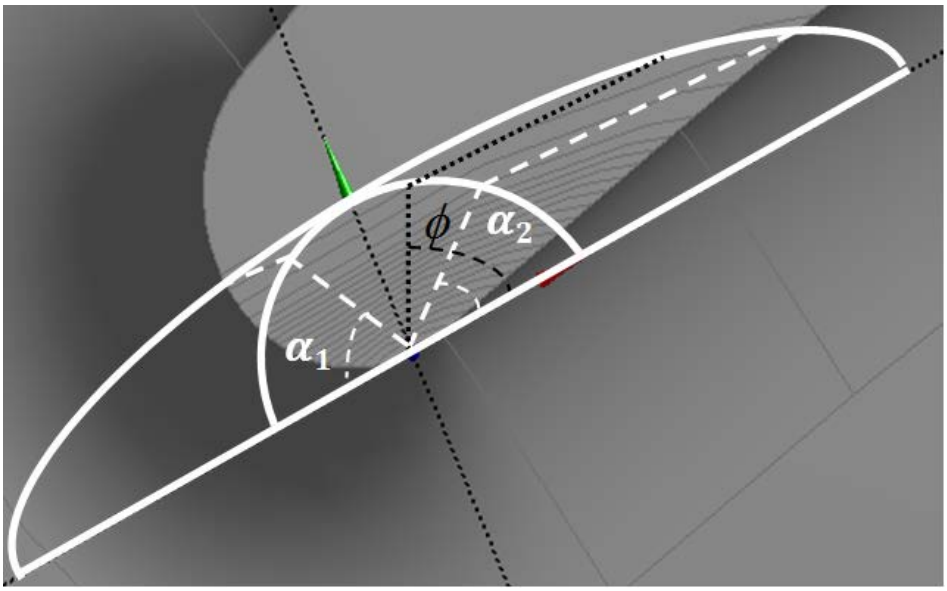

Figure III.12: Superficial semi-elliptical cracks schematically with of the angle ϕ.

In the Figure III.12 we have a superficial semi-elliptical cracks schematically and the crack angle ϕ, this angle presented the crack tip, this angle is limited between two angles, the beginnings angle α_1 to a finished angle $(\pi - \alpha_2)$.

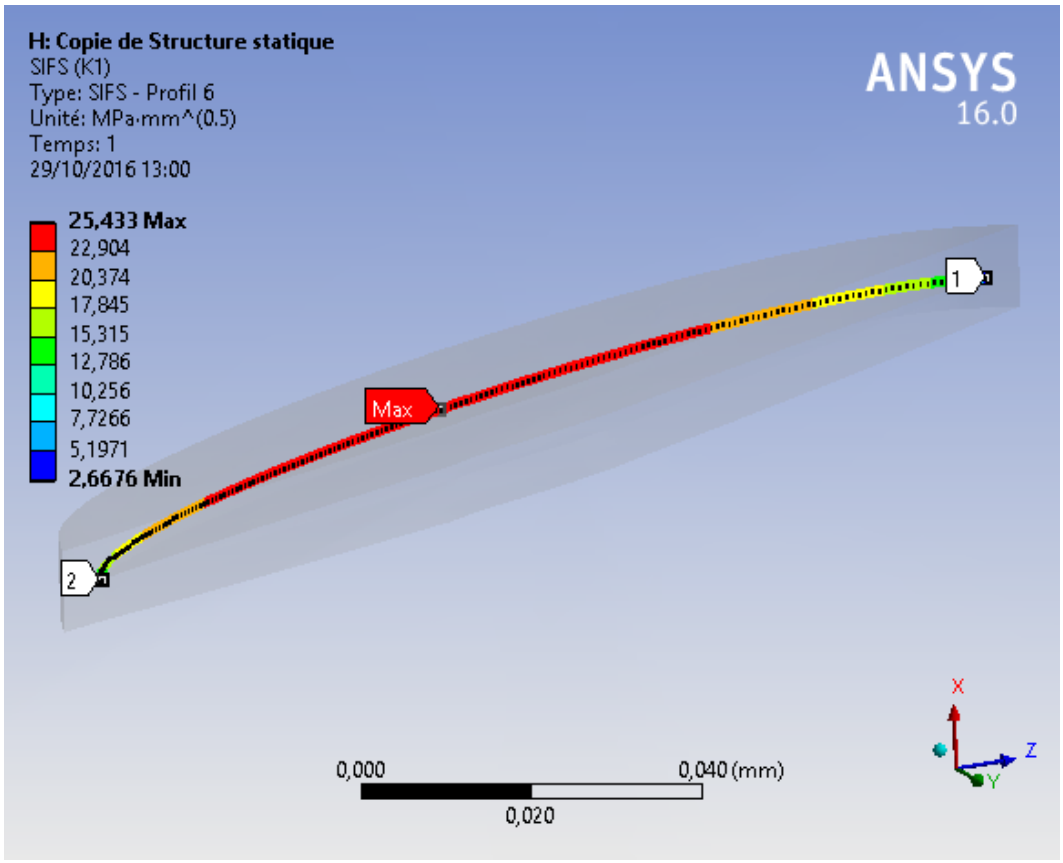

(a) Mode I

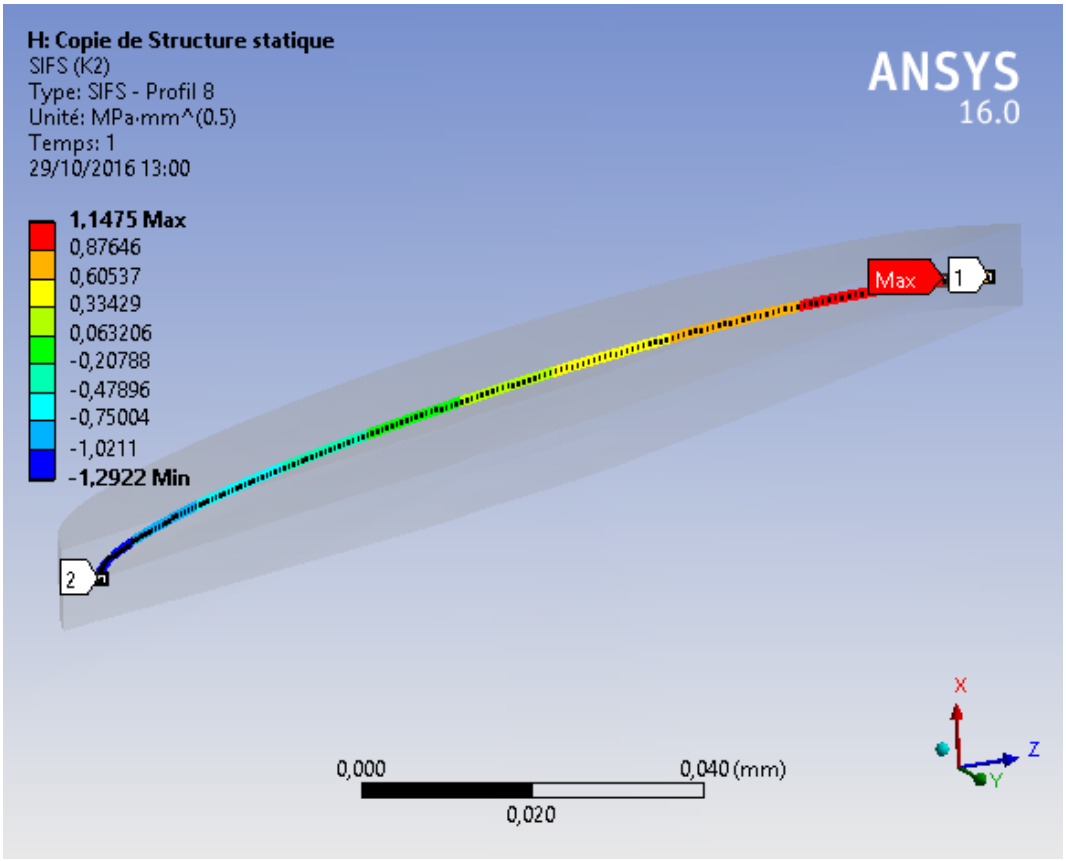

(b) Mode II

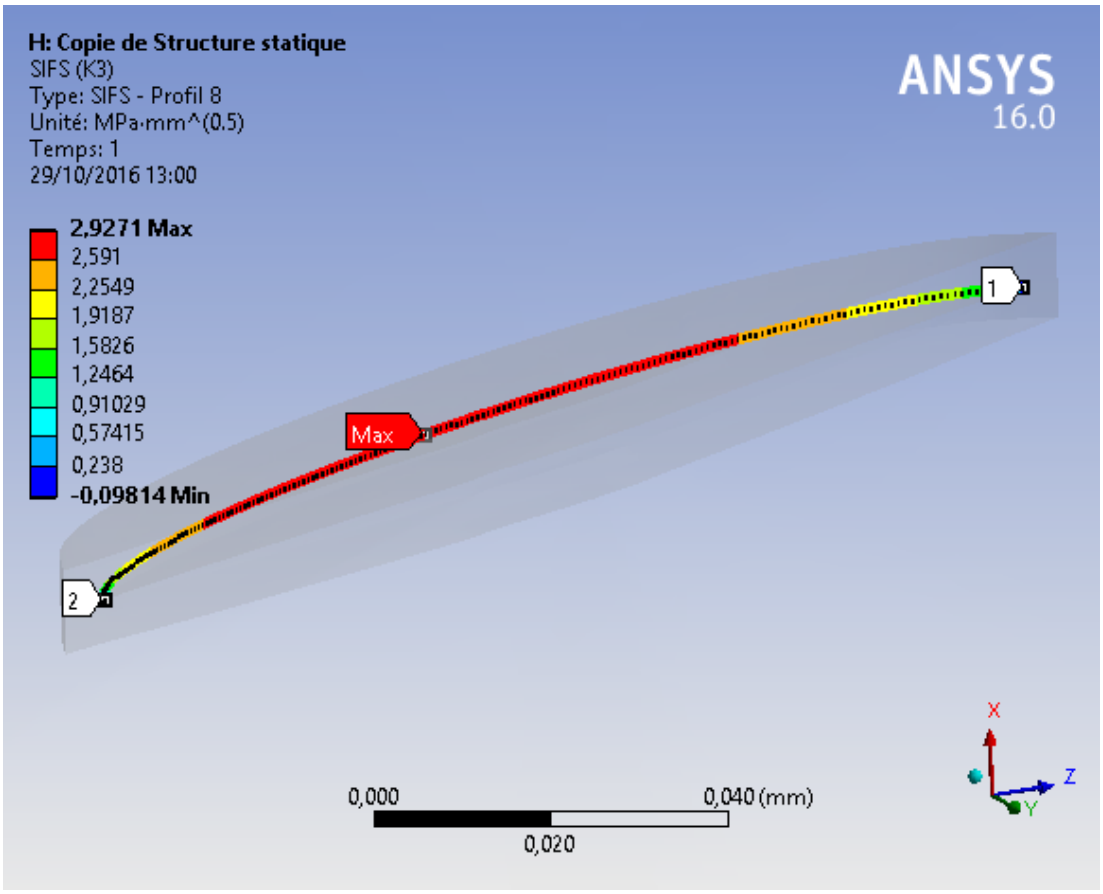

(c) Mode III

Figure III.13: Three modes of failure. (a) Opening mode; (b) plane shear mode; (c) shear mode anti-plan.

In the Figure III.13 the SIF K_I and K_{II} are maximum at point a. value of K_I depends upon the direction of the centrifugal load applied .the change in value of K_{II} is because of change in the direction in plane sliding for an applied load .the mode1 stress intensity factor at the location of the crack is shown in Figure III.13.a. For different crack lengths .the maximum SIF is 25.433 MPa $m^{0.5}$ at the surface interception points.

As remarked, the Stress intensity factor in the mode I are dominant. The extended analysis is made for the different angles and depths, recapitulated in the Table III.2

Table III.2. The angle ɵ with respect to the depth (e/a).

ϕ	88,06	90,01	114,35	133,65	152,18	158,04	160,15	160,38	165,84
a/e	0,005	0,01	0,1	0,2	0,3	0,35	0,4	0,45	0,5

with ϕ is the angle of front crack, a/e is the depth ratio as represented in the Figure III.14. The Figure III.14 presents the stress intensity factors (K_I, K_{II} and K_{III}) distribution a log the crack front, compared between a short crack and long crack depth, the maximum value of K_I and K_{II} is

located at both the deepest point at ϕ =90°. And the must domain mode is K_I. In the Figure III.14.b the a value deviate at ϕ=133,64°, so we have a crack propagation to this direction.

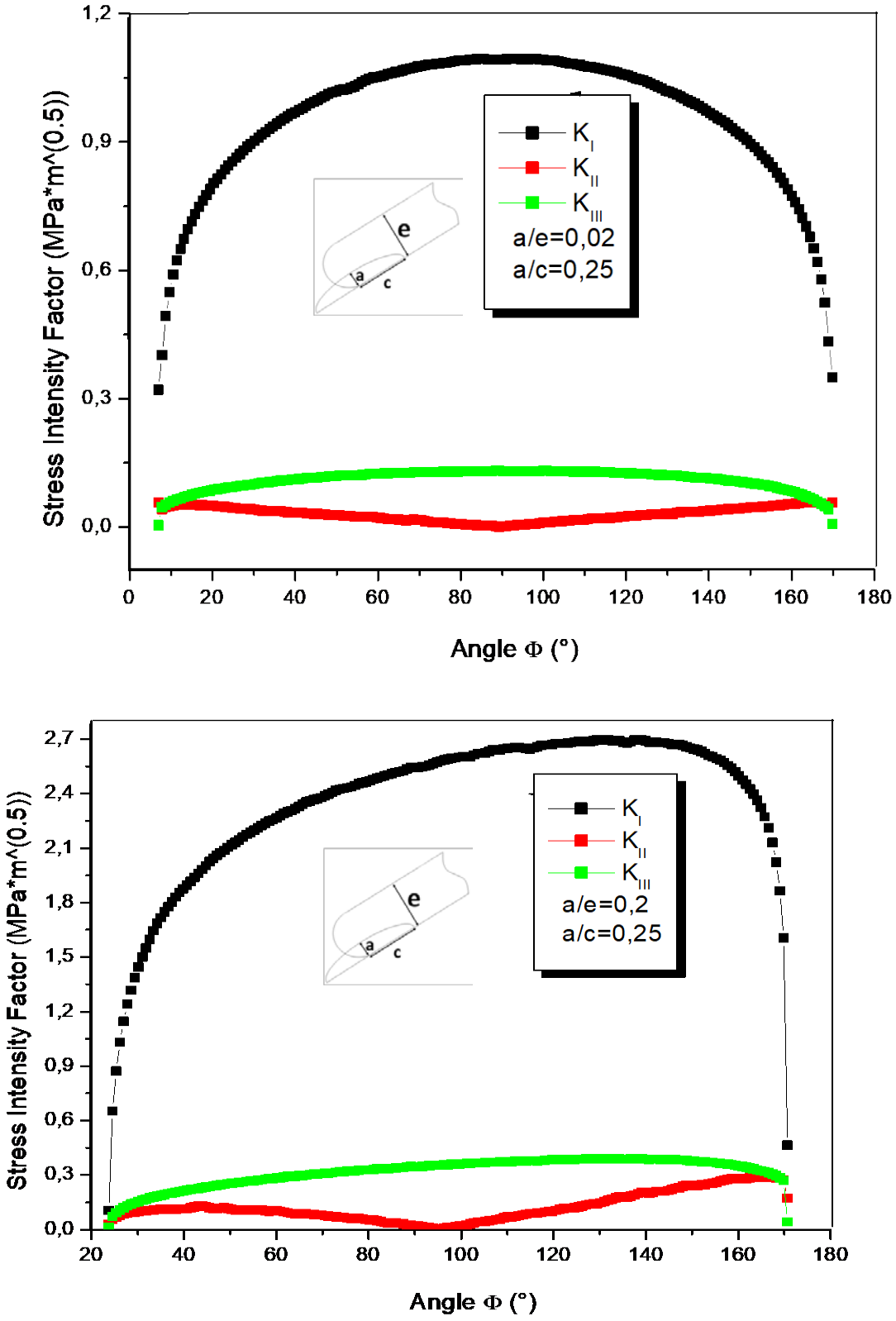

Figure III.14: stress intensity factors in different depth a

in order to validate the obtained stress intensity factor solution a NEWMAN & RAJU problem whose solution is available in literature has been solved by using fracture module in ANSYS® Work bench and ANSYS® APDL compression , consists of a rectangular bar having a semi-elliptical crack subjected to tension loading .the crack is defined by its crack length and crack depth. Among these formulas we were interested in our study in the work of NEWMAN & RAJU [7, 9] using their results presented in the analytical form. In this part was determined with two numerical methods to obtain more precision results.

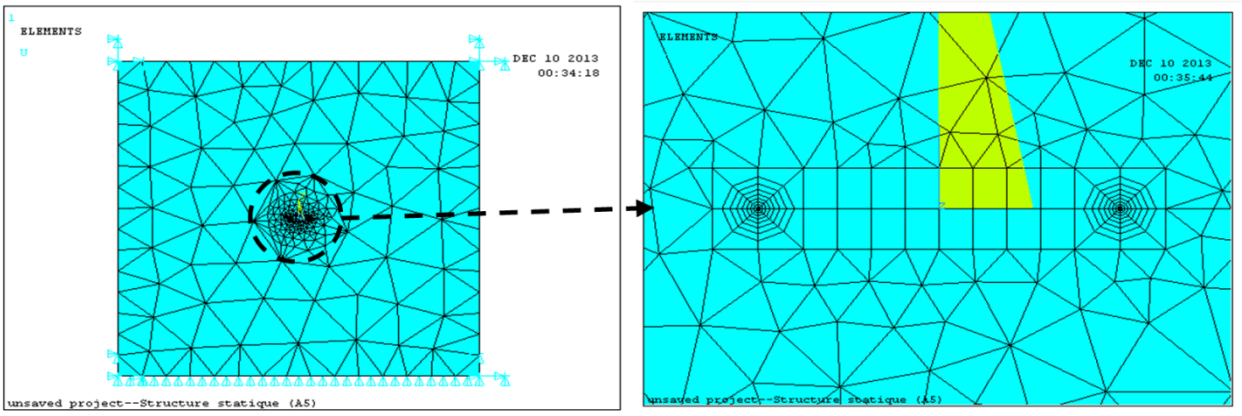

Figure III.15: Define the crack front mesh characteristics for APDL.

A rectangular bar having a semi-elliptical crack subjected to tension loading. The crack is defined by length c and depth a. The specimen with the dimensions 2b = 2h = 100 mm, and Thickness e=10 mm, for a circular crack of dimensions a/e=0.25. The bar was subjected to a pressure of P = 10 Pa on one side while at the other side displacements were constrained. Fine mesh was used near the crack region to obtain the accurate stress intensity factor solution. Assembly of the plate containing the crack is shown in the Figure III.15.

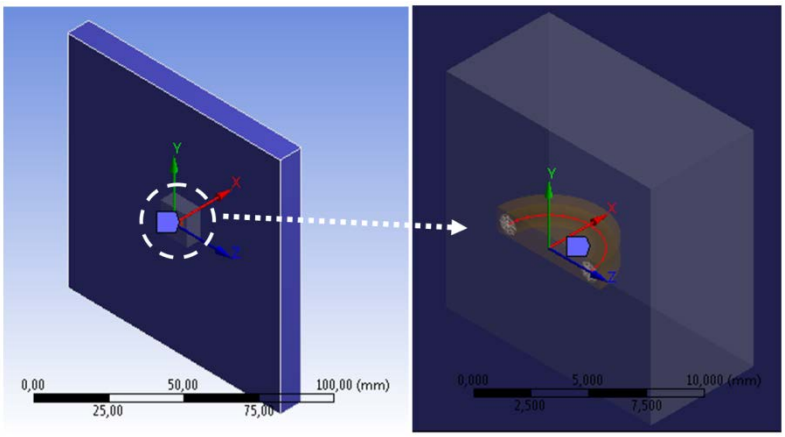

Figure III.16: Schematic representation of the domain and the semi-elliptic open fissure.

The evolution of the stress intensity factor in mode I normalized by the constant $K_0 = 2.P\sqrt{\pi a}$ is represented as a function of the angle ϕ describing the front of the crack.

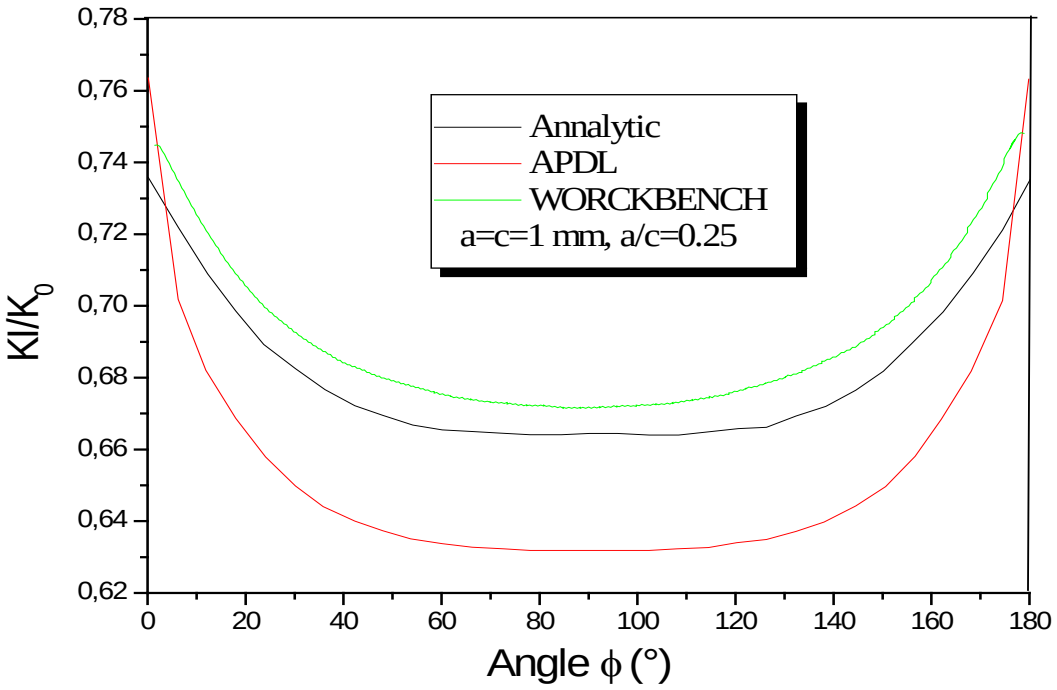

Figure III.17: Evolution of K_I along the front of semicircular fissures with APDL and WORCKBENCH compared to the analytical results determined by [7].

Numerical stress intensity factor solution for NEWMAN & RAJU problem is compared with workbench and APDL software methods, note that the maximum error obtained by WORKBENCH is less than 5%. However, the results obtained by APDL are 10%. For this purpose, we calculate the WORCKEBENCH calculation method for the remainder of this study.

In this parts The SIF distributions are presented separately for each of the crack modes for different depth, Figure III.18 shows variation of mode I, mode II and mode III stress intensity factors along the crack front relative to a depth variation from a/e=0,005 to 0,5 and a/c = 0,25. The maximum of K_I angle increase whenever we have an increase for variation of depth of crack. In this depth increase to a critical depth $\frac{a}{e} = 0{,}45$ at $\phi = 160{,}38°$where we have $K_I = K_{IC}$ (Fracture Toughness) Figure III.(18.a) , from this point we have crack instability. The factor of difference between the SIF of K_I and K_{II} is 22,8% and in the difference between K_I and K_{III} is 15,67% this two values negligible. For K_{II} and K_{III}, the values do not exceed 0.6 which lies that these values are negligible compared to the K_I.

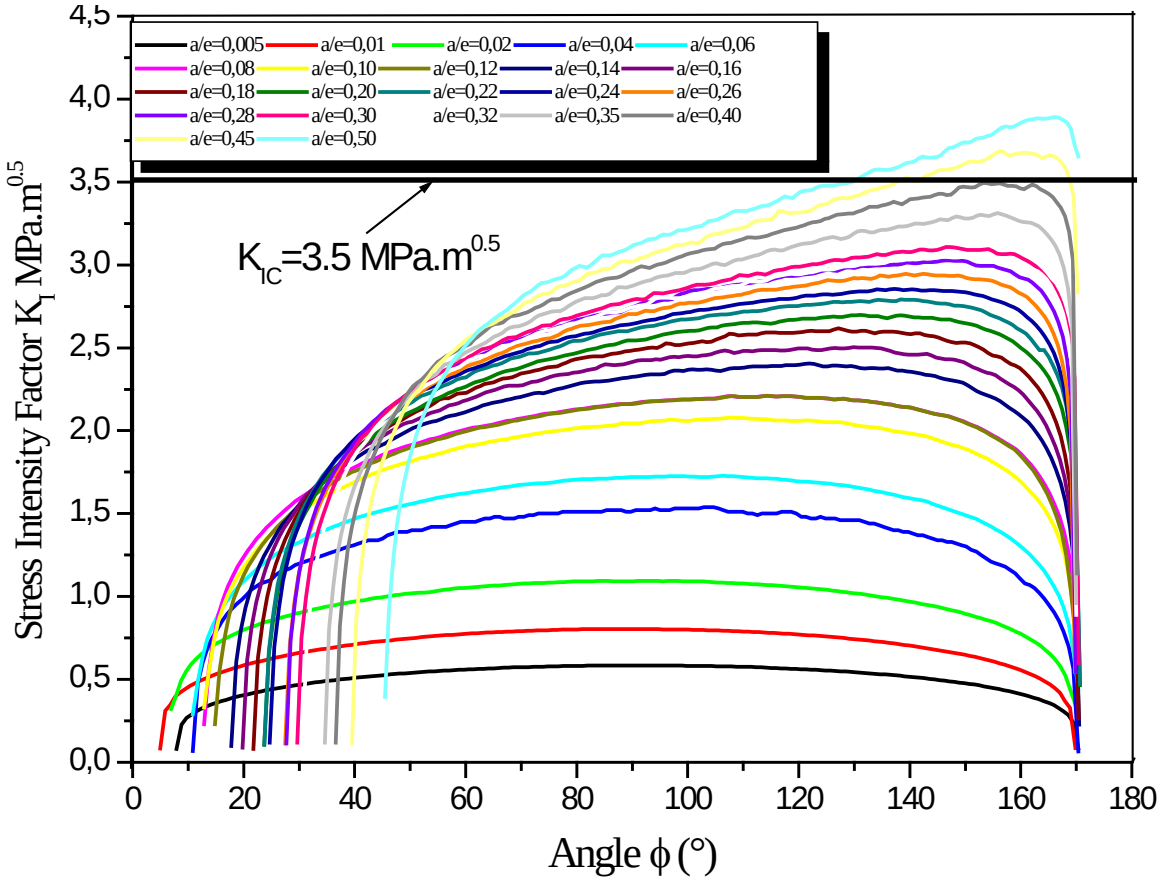
a/e=0,005 a/e=0,01 a/e=0,02 a/e=0,04 a/e=0,06
a/e=0,08 a/e=0,10 a/e=0,12 a/e=0,14 a/e=0,16
a/e=0,18 a/e=0,20 a/e=0,22 a/e=0,24 a/e=0,26
a/e=0,28 a/e=0,30 a/e=0,32 a/e=0,35 a/e=0,40
a/e=0,45 a/e=0,50
K_IC=3.5 MPa.m^0.5
Stress Intensity Factor K_I MPa.m^0.5
Angle ϕ (°)

(a)

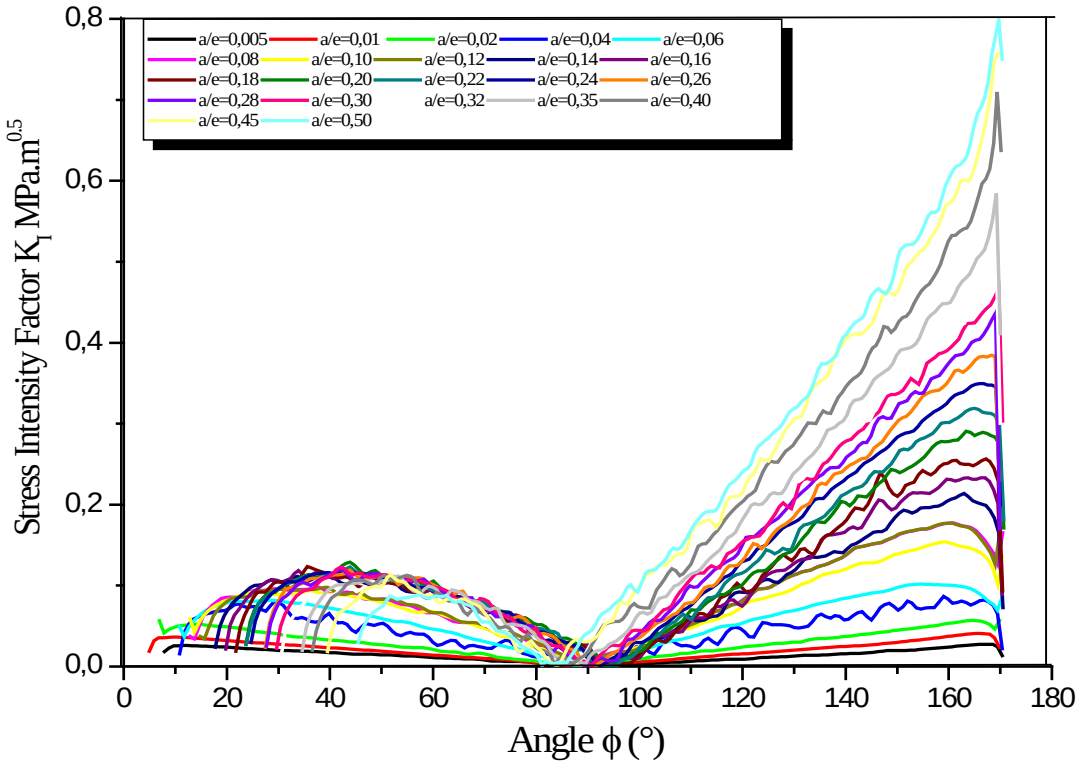
a/e=0,005 a/e=0,01 a/e=0,02 a/e=0,04 a/e=0,06
a/e=0,08 a/e=0,10 a/e=0,12 a/e=0,14 a/e=0,16
a/e=0,18 a/e=0,20 a/e=0,22 a/e=0,24 a/e=0,26
a/e=0,28 a/e=0,30 a/e=0,32 a/e=0,35 a/e=0,40
a/e=0,45 a/e=0,50
Stress Intensity Factor K_I MPa.m^0.5
Angle ϕ (°)

(b)

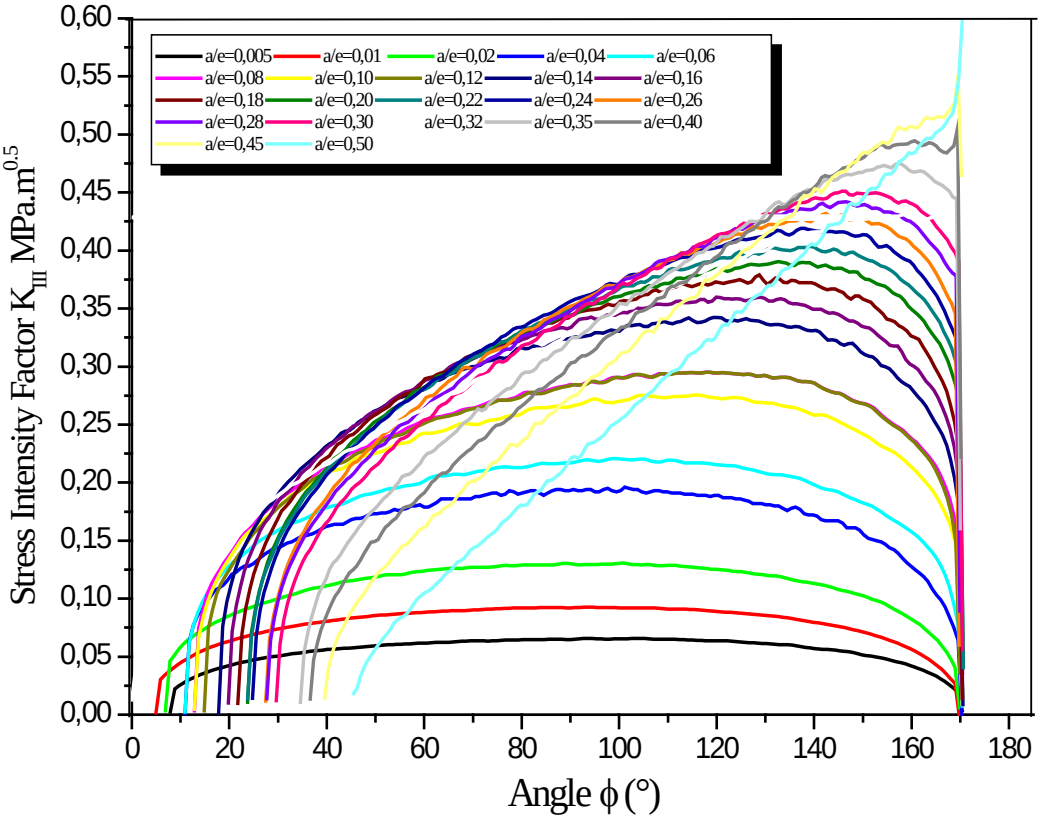

(c)

Figure III.18: Stress Intensity Factor, (a) K_I, (b) K_{II}, (c) K_{III}.

For different angles, we take the maximum value for $K_{I\,max}$:

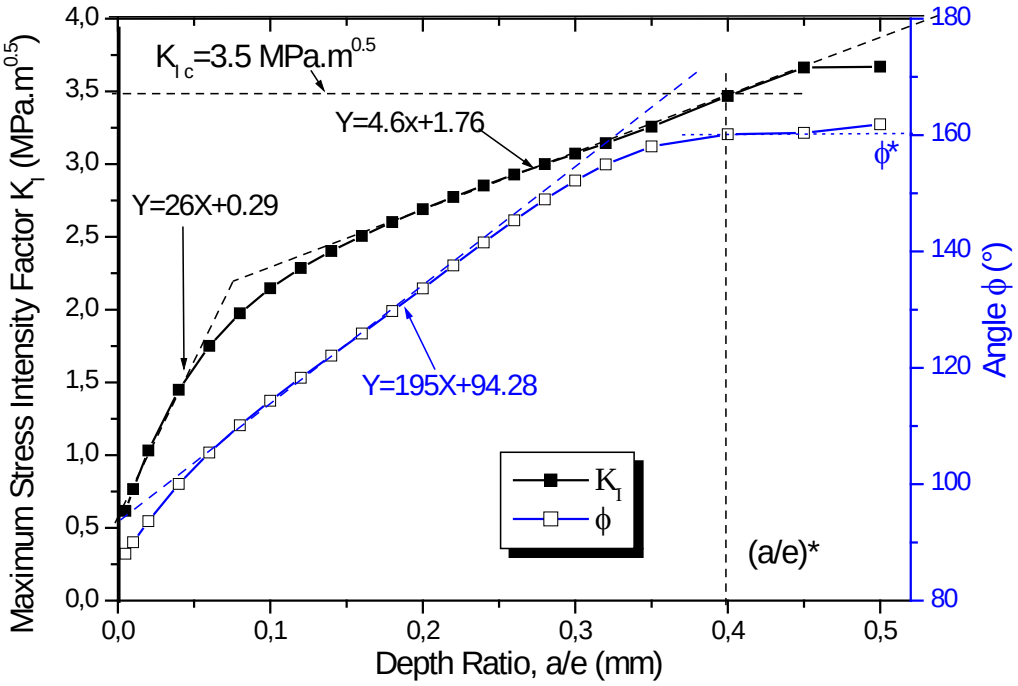

Figure III.19: The max values of stress intensity factors and angle on function of $\frac{a}{e}$.

For a given crack length, a linear behavior of the stress intensity factor maximum K_I for the same material is observed in the interval of depth ratio a/e=[0.08-0.5]

III.2.4.1 Equivalent Stress Intensity Factor

The horizontal axes stay the same like the other curves but the vertical axe will be the stress intensity factor equivalent In this case our curve look like the SIF in mode I , it increase every time we change the depth of crack and the beginning of crack angle change each time.

$$K_{eq} = \sqrt{(K_{II}^2 + K_{II}^2 + \frac{1+K_{III}^2}{1-\upsilon})} \qquad \text{(III.4)}$$

Note that the loading of the pure mode I gives almost the same values as K_{eq}, Also trearch that the K_{eq} depends on the root of the quasi sum of 3 modes and the coefficient of poison.

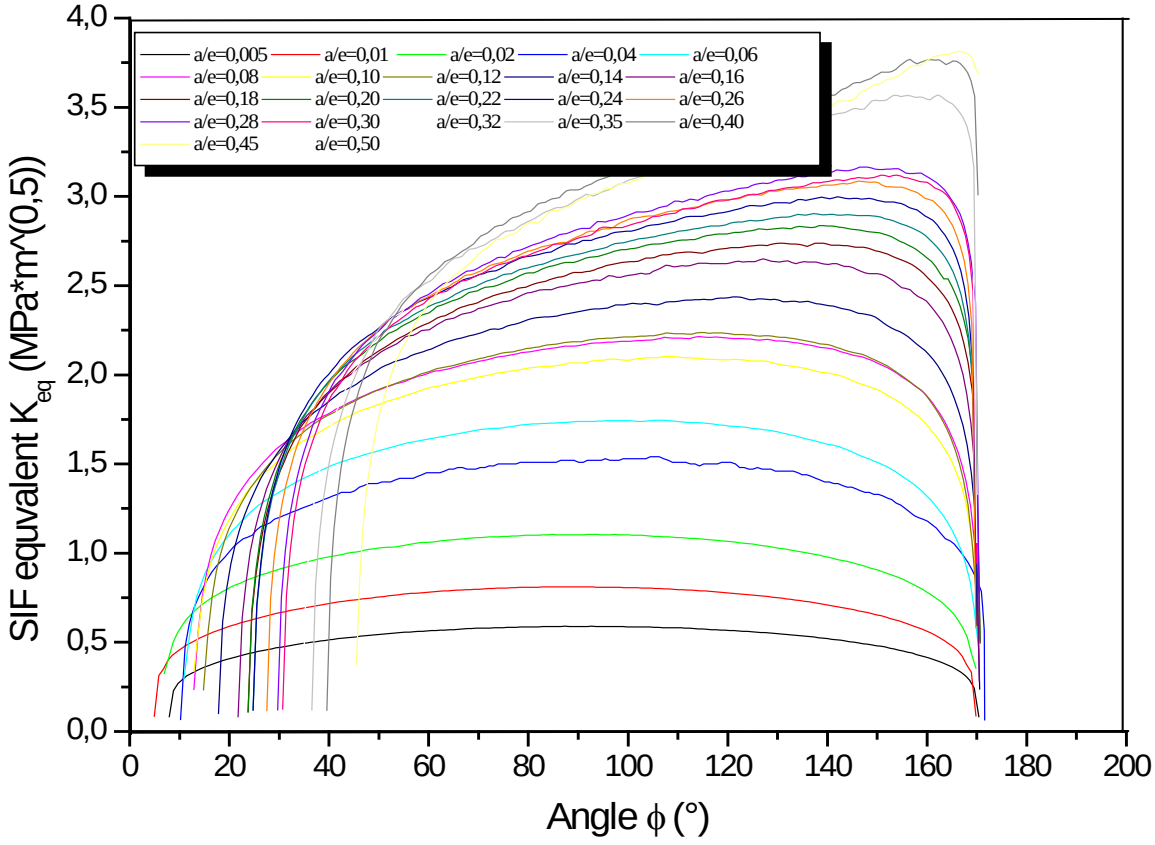

Figure III.20: Stress Intensity Factor equivalent (K_{equi}) en function to angle

- ✓ **Validation with the Wastergard equation**

We are interested in this study to the work of Westergard [7] equation for verify the credibility of this equation (III.5).

$$K_I = \sigma\sqrt{\pi a} \qquad \text{(III.5)}$$

Equations [III.1a, III.1b and III.1c] are the dominant near crack tip terms of the Westergard solution for the stress state near the crack tip in this problem [10].

Therefore, we plotted K_I against $\sqrt{\pi a}$, and we compared the tangent with the middling apply pressure (P_{midd}=0.187 MPa).

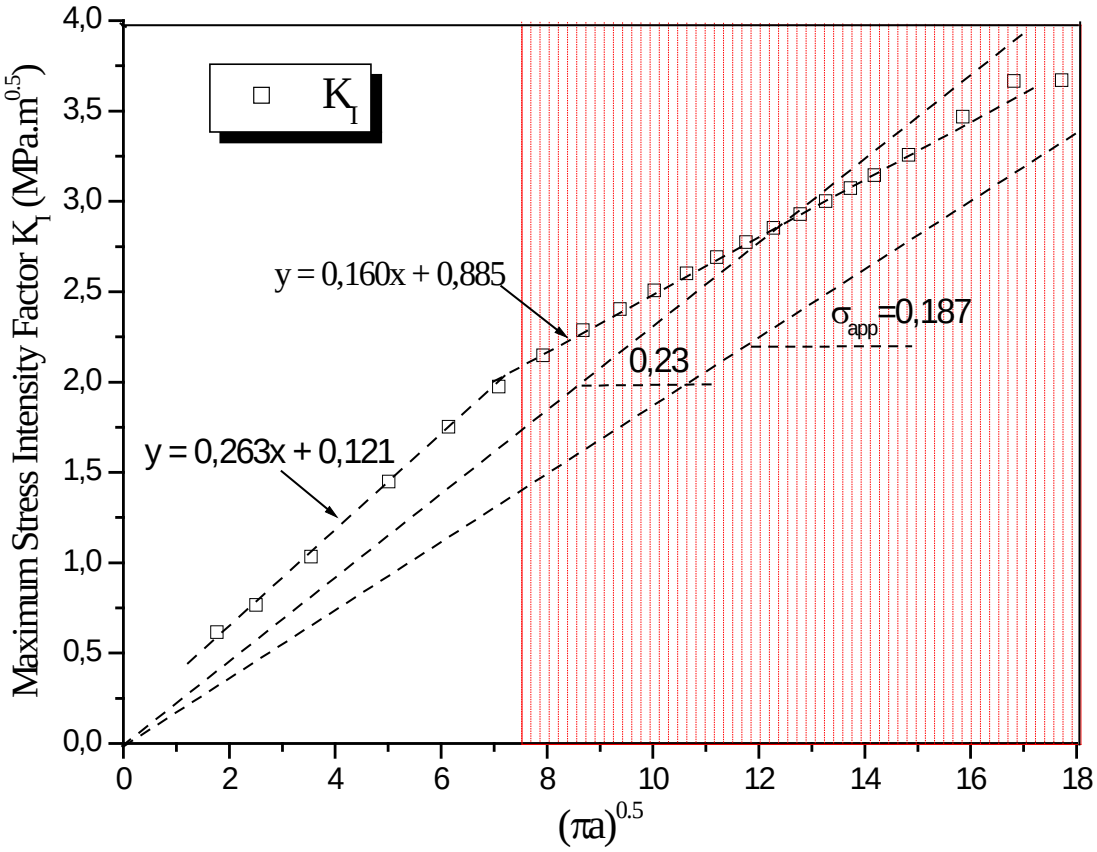

Figure III.21: The theory graph Wastergard equation.

In the last figure, it has been found that the tangent of Wastergard equation gives a value of 0.23 with an error of 23%, for which purpose the curve has been expressed in two parts in order to compare the results with that obtained.

The first part in the interval [0-7.8], the tangent is 0.263 with an error of 40.6%, the second part is 0.16 with an error of 14% in the interval [7.8-18], by these results it has been concluded that the Wastergard equation can be applied In the interval of [7.8-18].

The method demonstrated its potential by yielding excellent correlation with other available numerical.

III.2.4.2 Volumetric method to calculate T-stress on the blade

The Volumetric Method, presented by Pluvinage [11], is a meso-mechanical method belonging to the Notch Finite Element Method (NFEM). This methodassumes,as per the mesofracture principle, that the fracture process requires a physical volume. This assumption is supported by the fact that the fracture resistance is affected by the loading mode, structural geometry and scale effect. Using the value of the “hot spot stress”, i.e. the maximum stress valueis not possible to

explain the influence of theses parameters on fracture resistance. It isnecessary to take into account the stress value and the stress gradient in all neighboring points within the fracture process volume. This volume is assumed to be quasi-cylindrical with a notch plastic zone of similar shape.The diameter of this cylinder is called the “effective distance “. By computing the average value of opening stress within this zone, the fracture stress can be estimated.This leads to a local fracture stress criterion based on two parameters, namely, the effective distance X_{ef} and the effective opening stress $\sigma_{\theta\theta,ef}$. The graphical representation of this local fracture stress criterion is given in Figure **II**.22, where the stress normal to the notch plane is plotted against the distance ahead of the notch.

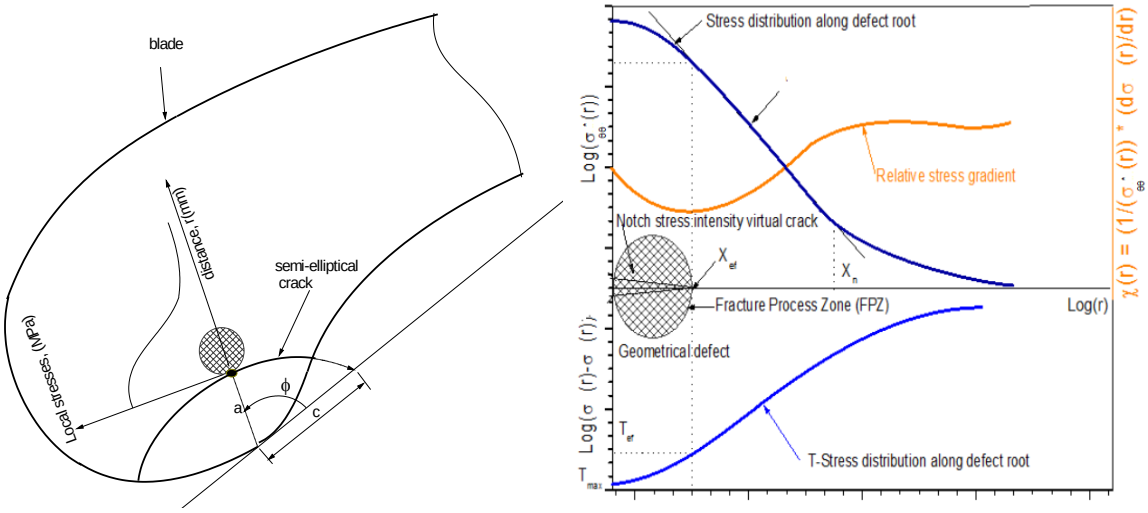

(a) (b)

Figure III. 22: (a) Schematic presentation of a local stress criterion for fracture emanating from notches and (b) determination of effective stress intensity factor and the effective T-stress at notch root together with the relative stress gradient versus distance from the notch tip.

For the determination of X_{ef}, a graphical procedure is used; itis observed that the effective distance is related to the maximum value of the relative stress gradient χ. This distance corresponds to the beginning of the pseudo stress gradient and it is indicated by **Figure III (22.**b). The opening stress distribution at the notch was calculated using FEM for elastic analysis of 2D model in plane strain conditions. The effective distance X_{ef} was determined using the normal stress distributions. The notches root plotted in bi-logarithmic axes and the relative stress gradient, plotted on the same graphallows obtainingthe effective distance value.

$$\chi(r)=\frac{1}{\sigma^{*}_{\theta\theta}(r)}\frac{\partial\sigma^{*}_{\theta\theta}(r)}{\partial r} \quad \text{(III.6)}$$

Where $\chi(r)$ and $\sigma^{*}_{\theta\theta}(r)$ are the relative stress gradient and the maximum principal stress or crack opening stress, respectively. The relative stress gradient depicts the severity of the stress concentration around the crack tips. However, the stress distribution effect is not solely a major parameter for the fracture process zone. The minimum point of the relative stress gradient in the bi-logarithmic diagram is conventionally taken into account as the relevant effective distance and signifies the virtual crack length. The effective stress is defined as the average of the weighted stress inside the fracture process zone:

$$\sigma^{*}_{\theta\theta,ef}=\frac{1}{X_{ef}}\int_{0}^{X_{ef}}\sigma^{*}_{\theta\theta}(r).\Phi(r)dr \quad \text{(III.7)}$$

Where $\sigma^{*}_{\theta\theta,ef}$, X_{ef}, $\sigma^{*}_{\theta\theta}(r)$ and $\Phi(r)$ are the effective stress, effective distance, maximum principal stress, and weight function, respectively. The unit weight function and Peterson's weight function are the simplest definitions of weight function the effective distance. The unit weight function deals with the average stress and Peterson's weight functions give the stress value at a specific distance and it is not required to compute numerical integration. Therefore, the Effective Stress Intensity Factor (ESIF) is described and defines as a function of effective distance and effective stress which is given by relationship III.8 below:

$$K_{ef}=\sigma^{*}_{\theta\theta,ef}\sqrt{2\pi X_{ef}} \quad \text{(III.8)}$$

ESIF is consideredto be as a value of facture toughness with a unit of MPa.$m^{0.5}$, and the minimum effective distance corresponds to the abscissa of the upper limit of zone II and its distance from notch rot was suggested to be the effective distance X_{ef}. The effective T-stress, T_{ef} is not singular as r→0, but it canbe modifiedto the effective crack tip plastic zone. The effective T-stress T_{ef} can be rewritten as follows:

$$T_{ef}=\frac{1}{X_{ef}}\int_{0}^{X_{ef}}T(r).\Phi(r).dr \quad \text{(III.9)}$$

Where $T=\left(\sigma^{*}_{rr}-\sigma^{*}_{\theta\theta}\right)$ and the effective stress intensity factor (K_{ef}) takes the form of

$$K_{ef} = K_{\rho} + T_{ef}\sqrt{2\pi X_{ef}} = \sigma_{ef}\sqrt{2\pi X_{ef}} + T_{ef}\sqrt{2\pi X_{ef}}\ ,\text{asr}\rightarrow X_{ef} \qquad \text{(III.10)}$$

The effective Stress Intensity Factor K_{ef}, the effective T-stress, T_{ef}, near the notch rot, and the relative distance are shown in Figure III 23. The Effective T-stress has been used as a constraint parameter. This addition to the classical plastic notch tip parameter K_{ef} provides an effective two-parameter characterization of elastic notch-tip fields in a variety of notch configurations and loading conditions.

As shown in Figure III.23. there is many t-stress curves for each depth ration with variation of angel. And this figure shows the variation of t-stress with the variation of angle so we take in each depth value from the curves and results of the values are in the Figure III.23.

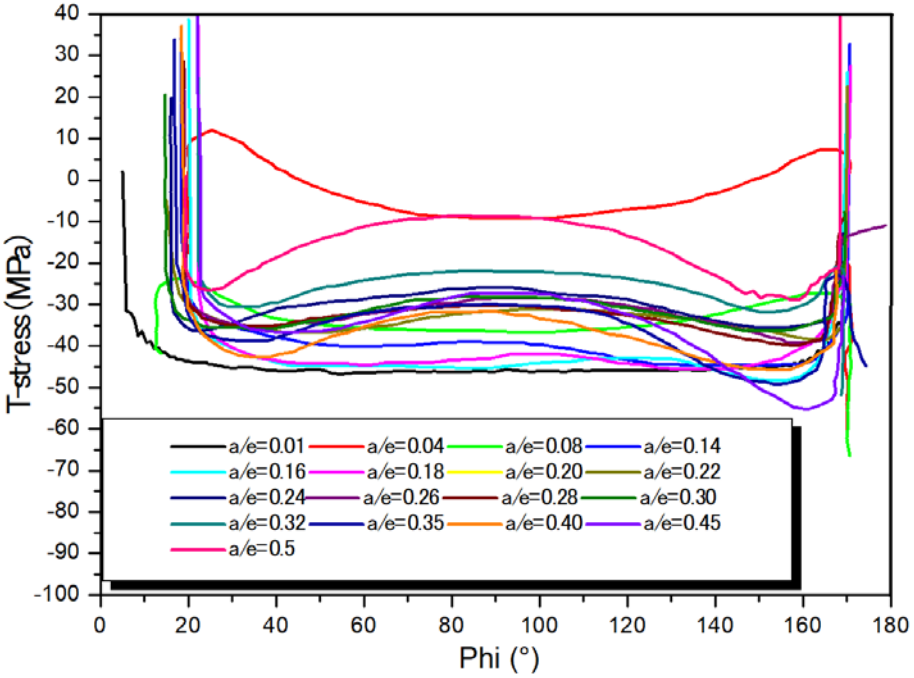

Figure III.23: the t-stresses curves in function of angle of crack

It was shown in Figure III.23 and Figure III.24, the T-stress has an influence on the way of cracking, a positive T-stress corresponds to a stress σ_{xx}higher than σ_{xx}. In such a configuration the crack should to Bifurcate. More generally, it was shown that a negative T-stress (T<<0) stabilizes (Figure III.25 (a)) the way of cracking, i.e. a small disturbance of the way of the crack will quickly be attenuated.

The opening stresses distribution along the principal proposal direction are presented separately for the relative depth variation from a/e = 0.1 to 0.5 as shown in Figure III.24 An example of the tangential stress distribution at the notch tip, the relative tangential stress gradient versus the distance and the determination of the effective distance were showed in the Figure. III.24.b. The

maximum of opening tangential stress ($\sigma_{\Theta\Theta,max}$) increases with the increase of the crack depth. Table III.3 recapitulates the effective opening stress, the effective distance and the effective stress intensity factorfor the different crack length.

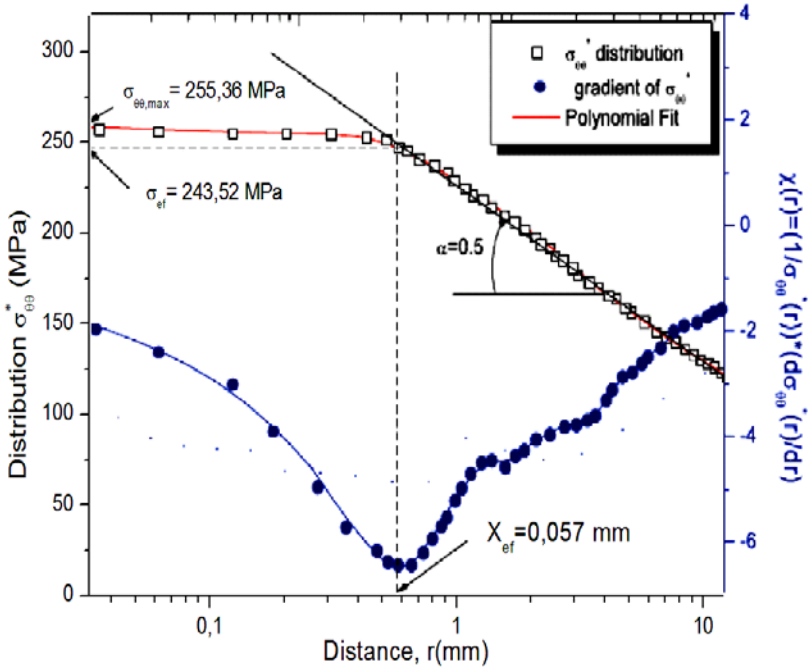

(a)

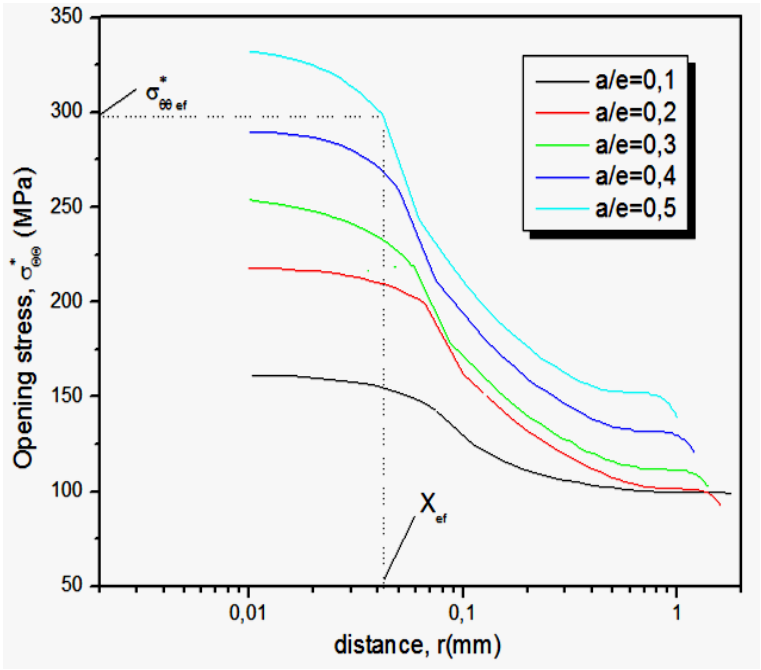

(b)

Figure III.24: (a) The opening stress distribution along of the ligament for the different crack length and example of the tangential stress distribution at the notch tip. Relative tangential stress gradient versus the distance. (b) Determination of the effective tangential distance for a/e = 0.3.

The Stress Difference Method (SDM) is used to determine the T parameter. It should be noted that this method does not produce constant values of the T-stress, except for short notches [12, 13]. The application of this method to determinate T in structures under pressure remains conservative in the presence of notches. As shown in Figure III.25.a, there are many T-stress curves for each depth ratio with a variation of angle. This figure shows the variation of T-stress with the variation of angle, so we take in each depth value from the curves as shown in Figure**.III.25**. b.

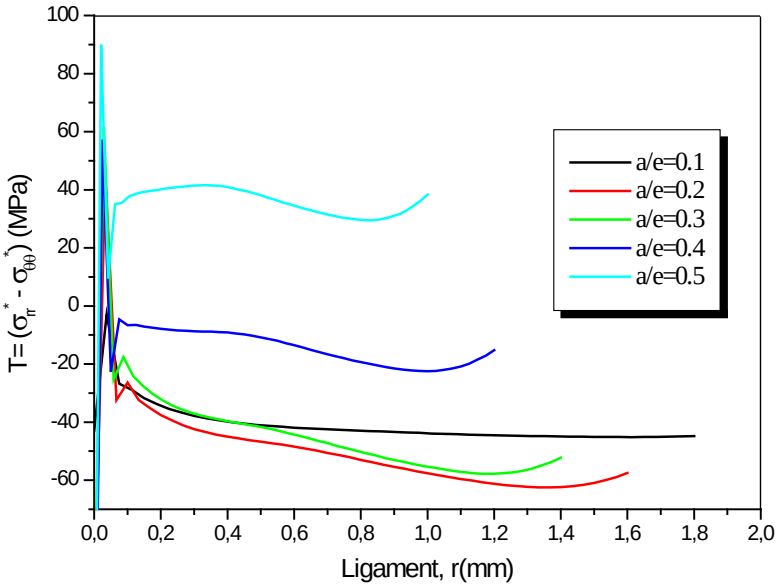

(a)

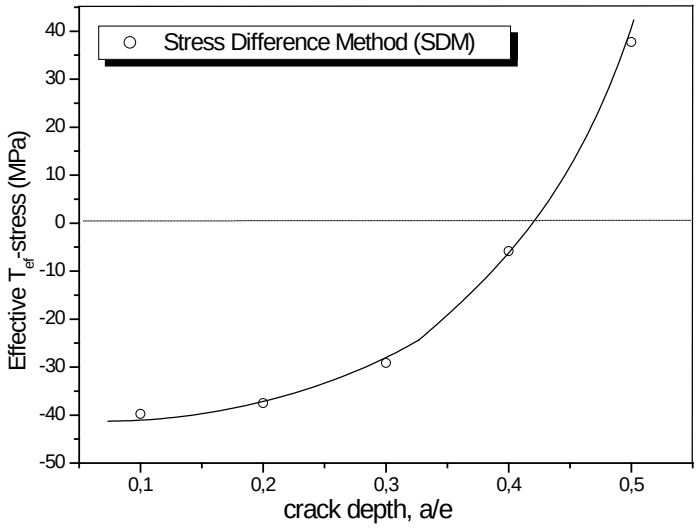

(b)

Fig.III.25. The T-stresses evolution along the ligament (a) and the effective T-stress for different crack depth (b) using the stress difference method.

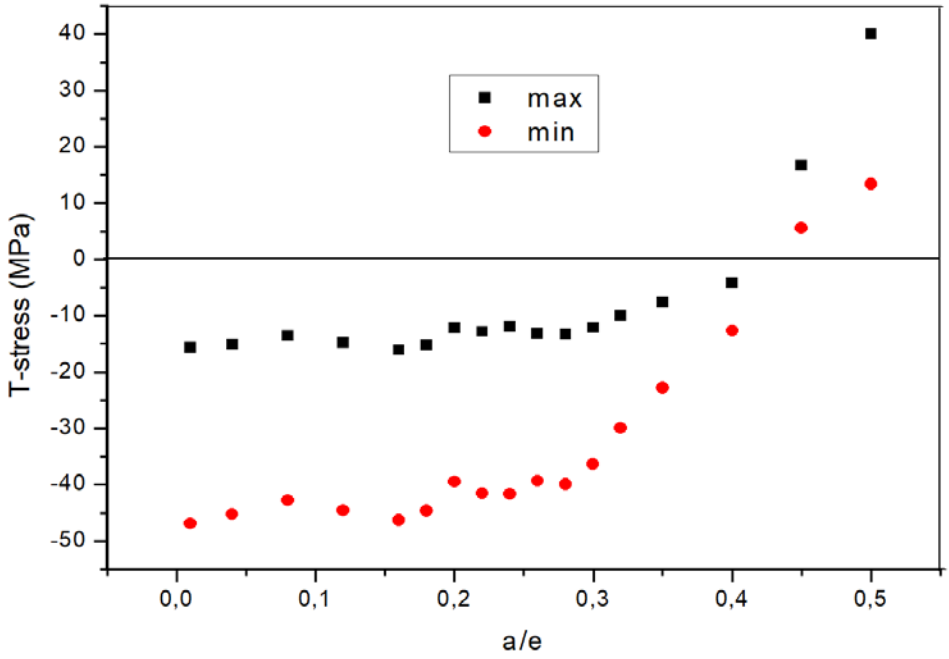

Figure III .26: cuve of T-stresses in function of depth ratio.

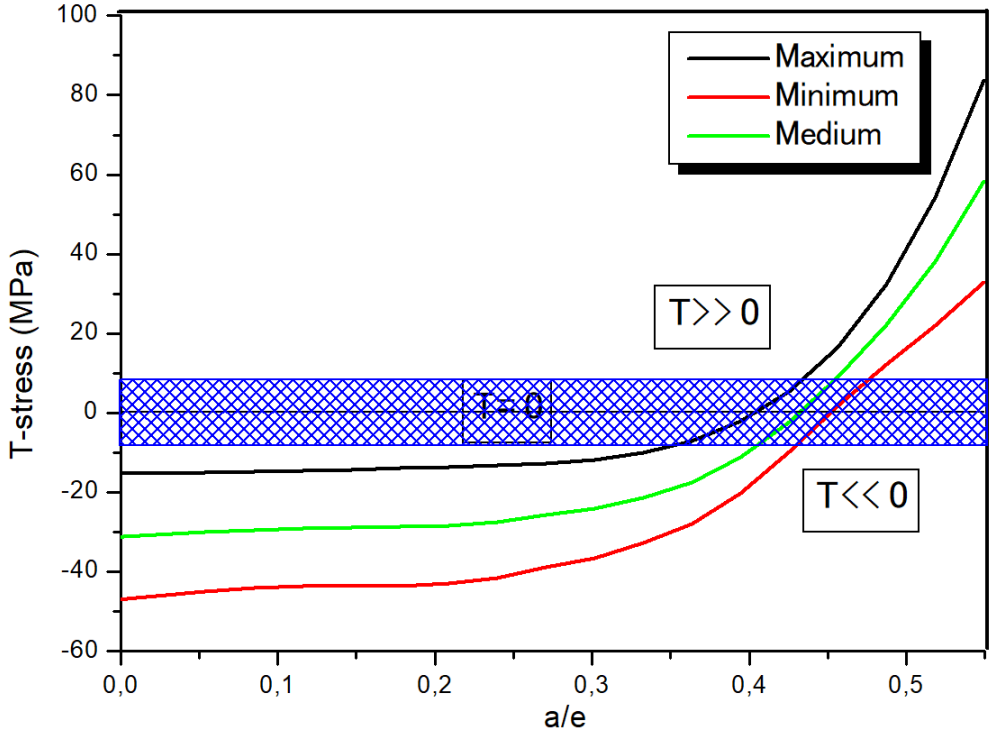

Figure III.27: Approximation of the T-stress distribution

On the other hand, a positive T-stress (T>>0) accentuates the deviations due to the microstructural obstacles and makes it possible the crack to Bifurcate (Figure **III**.28 (c)). But in case of T equal (T≈0) zero the crack can take one of the two behavior, stabilized or bifurcate (Figure **III**.28 (c)).

As shown in Figure III.28 (e), small-crack initiation and growth is a three-dimensional process (with cracks in the depth, a, and length, c), the crack depth may still be growing. As the crack grows in the depth direction, the rise in the crack-driving. As the cracks become longer

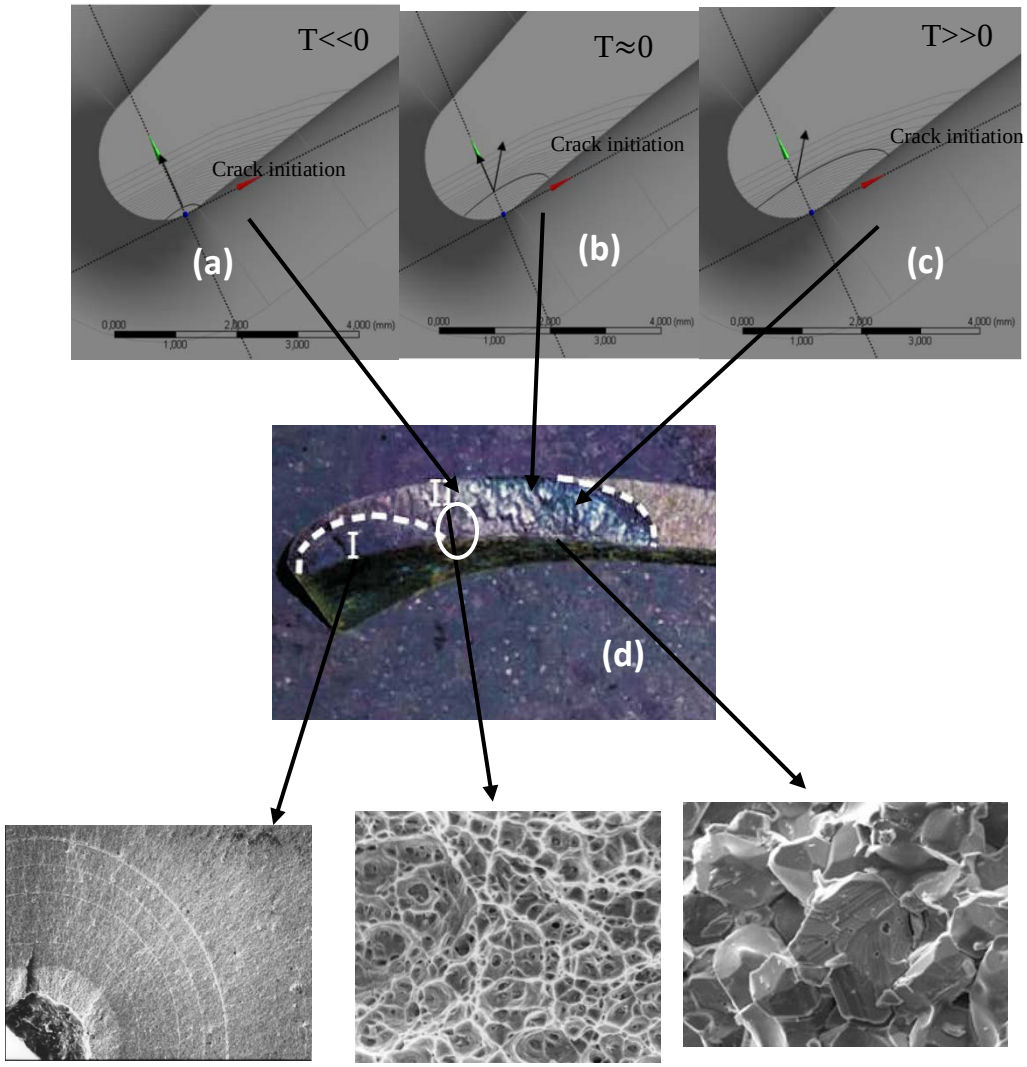

Figure III.28: Crack profile or Crack origin sites , (a) T<<0, (b) T=0 , (c) T >>0 , (d)General view of the fracture surface [14] , (e) zoom of crack beginning[15] ,(f) slow crack growth(ductile),(g) rapid crack growth (brittle**).**

Ductile fracture is a slow process and stable. It will on continue only if there is an increase in the level of applied stress. Normally occurred in a transgranular manner in the metal that has good ductility and toughness. This type of fracture involves plastic deformation in the vicinity of an advancing crack. In the Figure **III**.28. (e) shows a complete ductile fracture with small and uniform dimples.

Cracks spread very rapidly, unstable without further increase in the stress applied, with little or no plastic flow that is the brittle fracture (Figure **III**.28 (f)). The crack propagate most easily

along specific crystallographic planes by cleavage, in some cases, the crack may take an inter-granular path, particularly when segregation or inclusions weaken the grain boundaries.

Table III.3. The effective opening stress, the effective distance for the different of the crack length.

Crack length (a/e)	X_{ef} (mm)	$\sigma_{\theta\theta,ef}$ (MPa)	T_{ef} (MPa)	K_{ef} (MPa.m$^{0.5}$)
0.1	0.070	170.17	-38.57	3.36
0.2	0.060	215.58	-36.02	4.18
0.3	0.057	243.52	-31.29	4.61
0.4	0.048	292.39	-8.75	5.08
0.5	0.041	325.18	+36.76	5.22

III.3.Experimental validation research

In the experimental part, we have faced a problem with the raw material of the Inconel 718. For this reason, a material which has the same mechanical characteristics as the Inconel 718 ALLOY was used. This material is made of API 5L X52 steel. It is available in the Algerian industry.

In order to investigate the experimental analysis, the specimens of API X52 were put in a corrosive environment with the presence of hydrogen. Moreover, the experimental tests were used to examine the specimens embrittlement and their resistance to cracking. The obtained results in this study are valid in the turbine blades taking into consideration the same operating service (gas transport) and the environmental media of the gas compression (corrosive media of hydrogen which is transporting with the gas). These corrosive materials effect the turbine blades as shown in our previous numerical simulation.

III.3.1**HYDROGEN EMBRITTLEMENT EFFECT ON PIPELINE STEEL**

In this part, the results from hydrogen embrittlement test are described to study the effects on mechanical properties on the API 5L X52 pipeline steel, including the sandblasting, the optical

microscopic observations, tensile properties, impact strength and fracture toughness. The influence of hydrogen embrittlement is coupled with constraint (T-stress is used as constraint parameter) to show the effects on the Material Failure Master Curve (MFMC), for more details see [16].

II.3.2. Hydrogen effect on microstructure surface

Fracture surfaces were examined with a Scanning Electron Microscopy (SEM) for determination of fracture initiation points and also for checking of eventual fracture surface modification under influence of hydrogen. It has been found for hydrogen tests, inner fracture surface is characterized by an array of surface cracks (see Fig. 29(a)). Careful examination shows that, surface cracks density is higher and average crack length is smaller. View of surface cracks under hydrogen conditions is given in Fig. 29(b) at magnification X250.

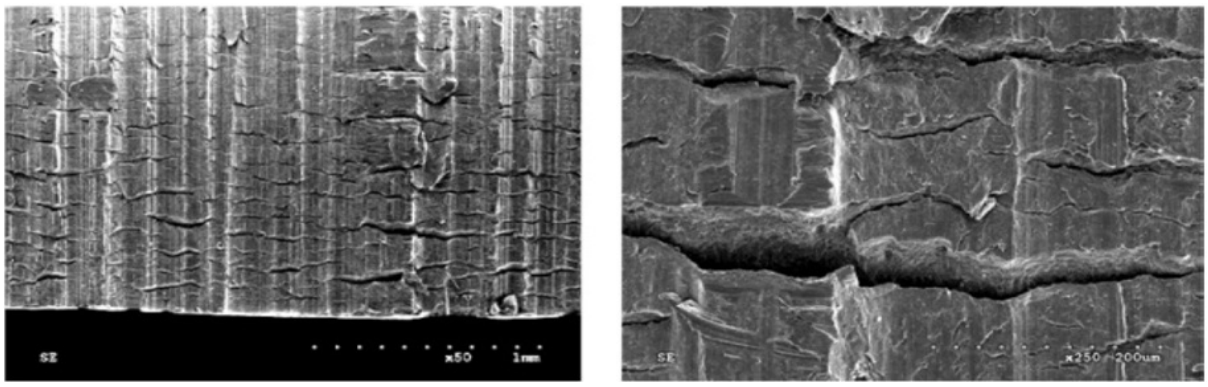

(a) (b)

Figure III.29- (a) Surface cracks mesh at the edge of fractured notch for test in hydrogen. (b) Magnification X250.

Crack propagation in air shows perlite debonding and ferrite matrix cracking as in Fig. 30. In air, crack propagates by mode I in ferrite phase. Some cracks are arrested in the perlitic phase, and continue as second crack in ferrite. Extension of second crack is probably prolongation of the first crack in third dimension. The perlite phase play the role of crack arrestator.

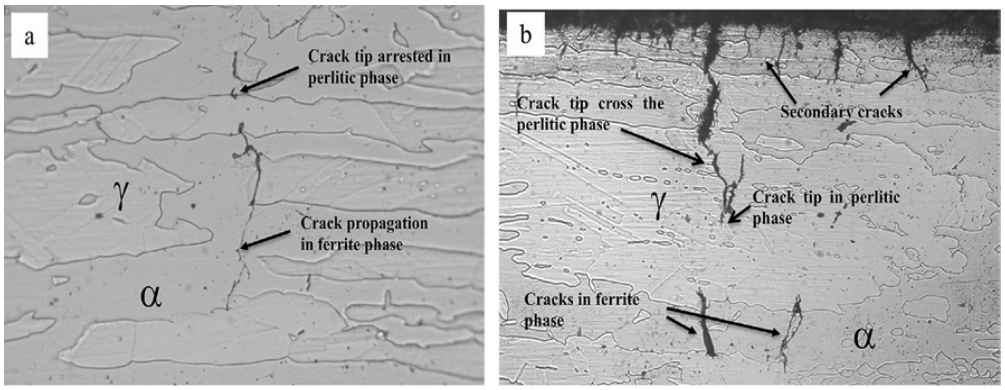

(a) 40µm (50X) (b) 100µm (20X)

Figure III.30- Optical photographs for cross section through the cracks and secondary cracks (a) without hydrogen & (b) hydrogen environment [17].

With hydrogen environment, fracture is sometimes initiated from secondary cracks and very close to the surface due to pitting under hydrogen attack as shown in Fig. 30(b). The crack stress field will produce a strain magnification in adjacent micro-cracks and penetration of hydrogen atoms will result in further cracking of ferrite phase at the crack tip. The crack cross the perlitic phase and will propagate in the straight direction, facilitating hydrogen propagation and weeping.

III.3.3. Hydrogen effect on tensile properties

The effect of hydrogen permeation and embrittlement on the low-carbon steels was investigated by Razzini et al.[18]. They found that the steels with yield strengths below about 900 MPa are essentially immune to hydrogen embrittlement, and almost all pipeline steels have a yield strength below that value. Cheolho Park et al.[19] has study the investigation of the grain size effect on the resistance to hydrogen embrittlement of API 2W Grade 60 steels. The fine grained (14 µm) steel showed superior HE resistance despite exhibiting higher total hydrogen content than the coarse-grained (35 µm) steel. R. Capriotti et al.[20] use the AISI 4130 steel charging by the hydrogen to showing their effect on the residual stress and on the mechanical properties. T. Bellahcene et al.[21] study the effect of hydrogen on the mechanical properties, using the API 5L X70 pipeline steel. M. Javidi et al.[22] swot up the stress corrosion cracking (SCC) and corrosion behaviour of API 5L X52 carbon steel in 25 wt-% diethanolamine solution, saturated/unsaturated with carbon dioxide and containing hydrogen sulphide at different temperatures were investigated using slow strain rate test.

Table III.4.– Hydrogen embrittellment effect on the mechanical properties of the API 5L X52 pipeline steel compared with the literature results.

		Young module (GPa)		Yield stress (MPa)		Ultimate stress (MPa)		Elongation (%)	
API 5L X52	Air	194	2 %	437	4 %	616	7 %	15.94	34 %
	H_2	191		420		570		10.56	
[21]	Air	/	/	549	2 %	707	20 %	13,5	40 %
	H_2	/		538		568		8,1	
[22]	Air	/	/	/	/	801	3 %	7,2	3 %
	H_2	/		/		779		6,0	
[23]	Air	/	/	625	8 %	712	13 %	19,9	32 %
	H_2	/		575		622		13,55	
[24]	Air	/	/	403	14 %	499	15 %	27,40	37 %
	H_2	/		347		423		17,17	

The effect of hydrogen on tensile properties of our API 5L X52 pipeline steel will present in this part. The stress strain curves will be determined with and without hydrogen absorption and reported in Fig 31. A small decrease of yield stress has been noted (2.5%) as an important reduction of elongation at failure than 38% (Table 4).

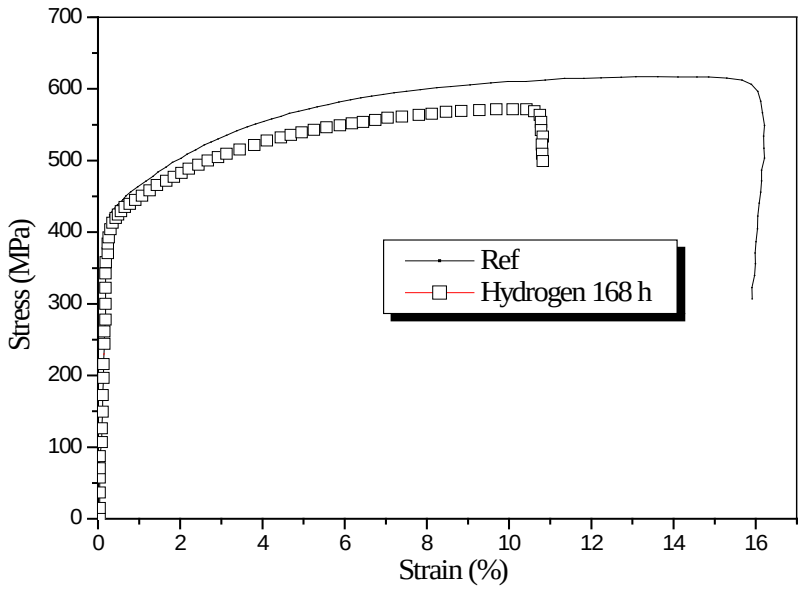

Figure III.31- Stress strain curves of API 5L X52 pipe steel with and without hydrogen absorption [17].

III.3.4 Hydrogen effect on fracture toughness

In this part we used a CT specimen immersed into the cell with solution NS_4 and exposed under constant potential of polarisation, which is slightly negative than free corrosion potential for

given steel. The hydrogen-charging process is controlled by registration of the cathodic polarisation current. Influence of holding time of electrolytic hydrogen charging has been inspired from [15], Fig 32.

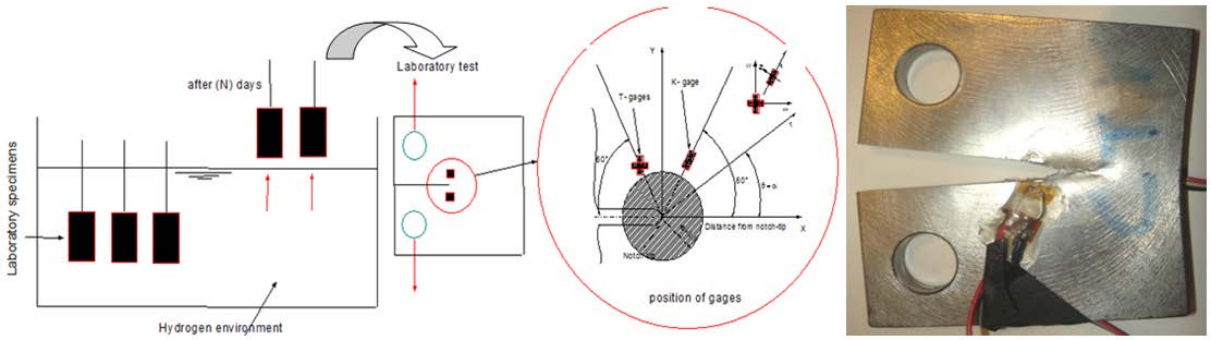

Figure III.32- Procedures of immersed specimens in hydrogen environment and emplacement of gauges near the notch-tip for the different specimens [24].

At these conditions hydrogen atoms are generated on the steel surface by the electrochemical reduction of water molecules according to known reactions [29].

Table III.5.- Influence of hydrogen on fracture toughness for a CT specimen of API 5L X52 API 5L X70 and API 5L X100 steels [30].

			$K_{I,i}$ (MPa.m$^{0.5}$)	$K_{I,moy}$ (MPa.m$^{0.5}$)	Influence (%)
API 5L X52	Air	CT1	97,59	95,54	13,44
		CT2	93,49		
	Hydrogen	CT1	85,55	82,69	
		CT2	79,84		
API 5L X70	Air	CT1	117.99	118.59	4.74
		CT2	119.19		
	Hydrogen	CT1	111.10	112.97	
		CT2	114.84		
API 5L X100	Air	CT1	159.99	151.82	0.80
		CT2	143.66		
	Hydrogen	CT1	155.85	150.61	
		CT2	145.37		

III.3.5 ASSESSMENT OF CORROSION DEFECT

Pipelines have been employed as one of the most practical and low price method for large oil and gas transport since 1950. The pipe line installations for oil and gas transmission are drastically increased in the past ten years. Consequently, the pipeline failure problems have been

increasingly occurred. Failures emanating from corrosion defect are elasto plastic fracture or plastic collapse. For these two situations, defect assessment is made generally by two tools: SINTAP procedure and limit analysis (LA).

III.3.6. Limit Analysis

The structural integrity of corrosion defects is substantially studied. In Fig. 33, a list of methods available for corrosion defect assessment is presented. They are grouped vertically by their type, codified methods or others, and horizontally by their applicability, pressure or combined loading, etc [31]. The pressure at all points of the pipeline should be less than the maximum allowable operating pressure (MAOP) which is a design parameter in the pipeline engineering. This upper limit is calculated using Equation (3):

$$P < MAOP \tag{2}$$

$$MAOP = SMYS \frac{2t}{D-t} f_F f_E f_T \tag{3}$$

When the P is the service pressure, the MAOP is the maximum allowable operating pressure, the SMYS is called the specified minimum yield strength (SMYS) of pipe material. the nominal wall thickness noticed by t, D the Outside diameter of pipeline. The factor f_F has been named the design factor (for the liquid f_F=0.72, for the gas 0.4<f_F<0.2) [32]. This factor is usually 0.72 for cross-country or offshore gas pipelines, but can be as low as 0.4, depending on class location and type of construction. The class locations, in turn, depend on the population density in the vicinity of the pipeline. The seam joint factor, f_E, varies with the type of pipe material and joint type. Seam joint factors are between 1 and 0.6 for the most commonly used material types. The temperature de-ration factor, f_T, is equal to 1 for the gas temperature below 120^{o}C but it arrives to 0.867 at 230^{o}C [32].

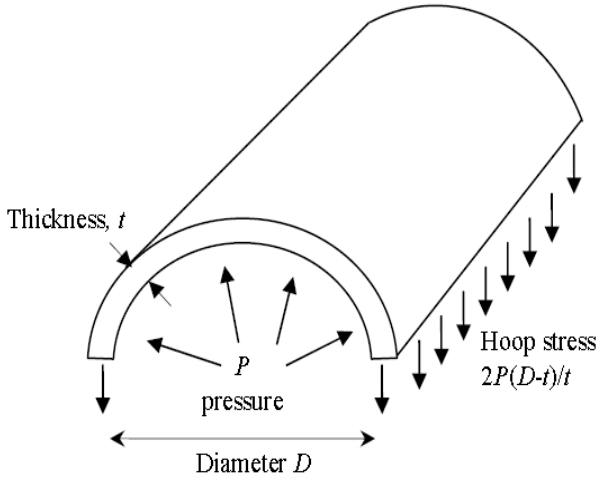

Figure III.33- Stress in pipeline subjected to internal pressure due to gas flow [32].

Several common design codes that incorporate the PF models are the DNV RP F101, Modified ASME B31G, Shell, RSTRENG, PCORRC, Netto Method and Choi's. It can be said that these codes were more or less originated from the original B21G criterion but later evolved using extensive series of full-scale tests results on corroded pipelines. Most of these codes are represented by safety factors and thus making it as deterministic in nature. An example of these codes can be found in Table 6. Each PF model is governed by input parameters of pipe outer diameter (D), wall thickness (t), minimum yield strength (SMYS) or ultimate tensile strength (SMYS), longitudinal extend of corrosion (l) and corrosion defect depth (d). Even though design codes have helped avoid unnecessary repairs and replacements, the excess conservatism continues to cause some unnecessary repairs.

Table III.6.- Failure pressure (PF) models used to compute remaining strength of pipeline subjected to corrosion.

Failure pressure models	Failure pressure expression, *PF*	Bulging factor, *M*
ASME B31G	$PF = \frac{2(1.1SMYS)t}{D}\left[\frac{1-\frac{2d}{3t}}{1-\frac{2d}{3tM}}\right]$	$M = \sqrt{1+\frac{0.8L^2}{Dt}}$
Modified ASME B31G	$PF = \frac{2(SMYS+68.95)t}{D}\left[\frac{1-0.85(d/t)}{1-0.85(d/t)/M}\right]$	$M = \sqrt{1+0.6275\left(\frac{l^2}{Dt}\right)-0.003375\left(\frac{l^4}{D^2t^2}\right)}$ $For\sqrt{\frac{l^2}{Dt}} \le 50$ $M = 3.3+0.032\left(\frac{l^2}{Dt}\right)$ $For\sqrt{\frac{l^2}{Dt}} \ge 50$
DNV RP F101	$PF = \frac{2SMTSt}{D-t}\left[\frac{1-(d/t)}{1-(d/t)/M}\right]$	$M = \sqrt{1+0.31\left(\frac{l}{Dt}\right)^2}$
SHELL-92	$PF = \frac{1.8SMTSt}{D}\left[\frac{1-(d/t)}{1-(d/t)/M}\right]$	$M = \sqrt{1+0.805\left(\frac{l}{Dt}\right)^2}$

RSTRENG	$PF = \frac{2SMTSt}{D}\left[1-(d/t)/M\right]$	$M = \sqrt{1+0.6275\left(\frac{l^2}{Dt}\right)-0.003375\left(\frac{l^4}{D^2t^2}\right)}$
Netto Method	$PF = \frac{1.1SMTS2t}{D}\left[1-0.9435(d/t)^{1.6}\left(\frac{l}{D}\right)^{0.4}\right]$	/
Choi's	$PF = 0.9\frac{2SMTSt}{D}\left[C_0 - C_1\left(\frac{L}{Rt}\right)+C_2\left(\frac{L}{Rt}\right)^2\right] \quad \sqrt{\frac{l}{Rt}} < 6$	$C_0 = 0.06\left(\frac{d}{t}\right)^2 - 0.1035\left(\frac{d}{t}\right)+1$ $C_1 = -0.6913\left(\frac{d}{t}\right)^2 + 0.4548\left(\frac{d}{t}\right) - 0.1447$ $C_2 = 0.1163\left(\frac{d}{t}\right)^2 - 0.1053\left(\frac{d}{t}\right)+0.0292$
	$PF = 1\frac{2SMTSt}{D}\left[C_3 - C_4\left(\frac{L}{Rt}\right)\right] \quad \sqrt{\frac{l}{Rt}} > 6$	$C_3 = -0.9847\left(\frac{d}{t}\right)+1.1101$ $C_4 = 0.0071\left(\frac{d}{t}\right) - 0.0126$

III.3.7. SINTAP procedure

In the structural integrity assessment analysis, two types of philosophy have been selected for the SINTAP procedure. The first used the concept of a crack driving force curve (CDF) and the second is the Failure Assessment Diagram (FAD). In the CDF approach based on the J-integral concept compared directly with the material's fracture toughness without taking into count of the plastic limit effect. On the other hand, the FAD approach uses the comparison of the crack tip driving force with the material's fracture toughness and with the plastic load limit analysis at the same time (Figure 34).

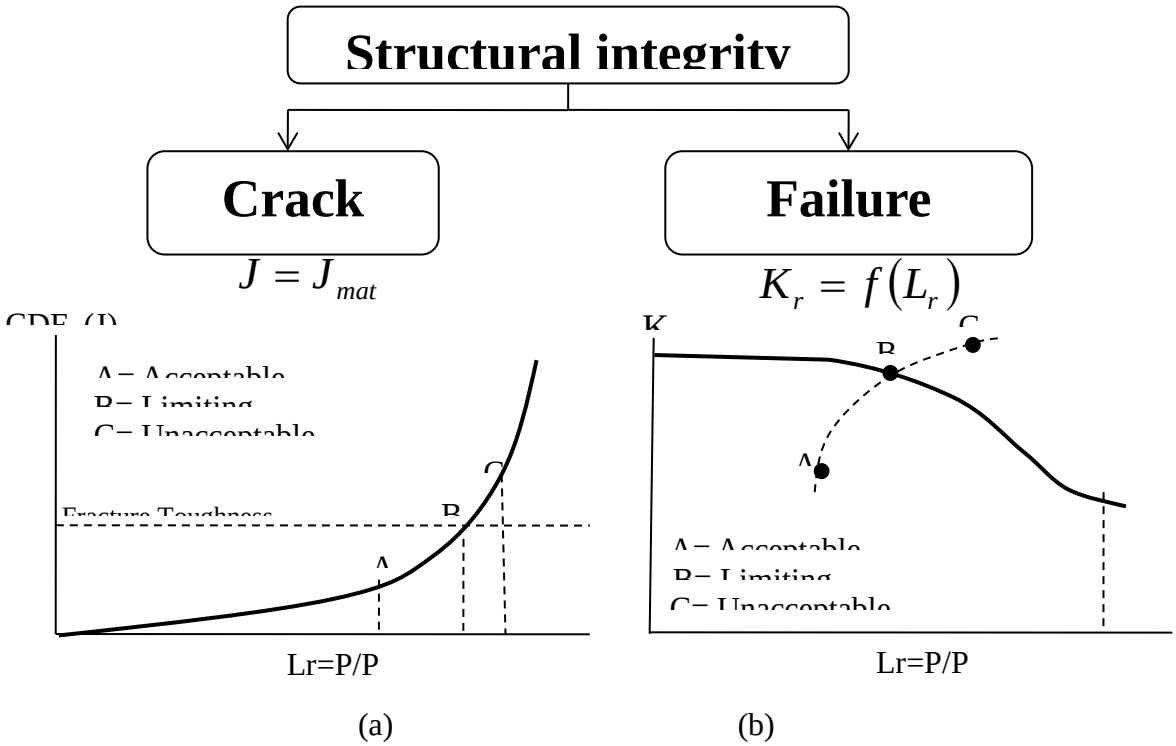

Figure III.34- Schimic representation of the two approaches using in the SINTAP. (a) CDF and (b) FAD.

III.3.8. CDF Route

In the CDF route (Figure 6(a)), an applied parameter such as the J-integral or crack tip opening displacement (CTOD = δ) is determined, which characterizes the stresses and strains ahead of the crack tip in a specimen or component:

$$J = J_e\left[f\left(L_r\right)\right]^{-2} \; or \; \delta = \delta_e\left[f\left(L_r\right)\right]^{-2} \tag{4}$$

where J_e and δ_e are the elastic values of the crack tip parameters which can be deduced from the stress intensity factor K_I (a,F) as

$$J_e = \frac{\left[K_I\left(a,F\right)\right]^2}{E'} \; or \; \delta_e = \frac{\left[K_I\left(a,F\right)\right]^2}{E'} \tag{5}$$

with E' being Young's modulus E in plane stress and $E/(1-\nu^2)$ in plane strain. The quantity ν is Poisson's ratio. The fracture resistance of the material is used in terms of the K factor, K_{mat}. This quantity is obtained formally from the J-integral or CTOD by:

$$K_{mat} = \sqrt{\frac{J_{mat}.E}{\left(1-\nu^2\right)}} = \sqrt{\frac{\sigma_y.\delta_{mat}.E}{\left(1-\nu^2\right)}} \tag{6}$$

With J_{mat} and δ_{mat} the fracture toughness of material (J-integral and CTOD) [33].

III.3.9. Failure Assessment Diagram

Any kind of rupture (brittle, elastoplastic or plastic collapse) can be represented by a working point in graph non dimensional applied crack driving force k_r versus non dimensional applied load L_r. Critical values of k_r and L_r define a critical curve (or interpolation curve). In the above mentioned graph, this curve defines the integrity area as the area under the interpolation curve between critical points (0;1) and (1;0) (Fig. 35).

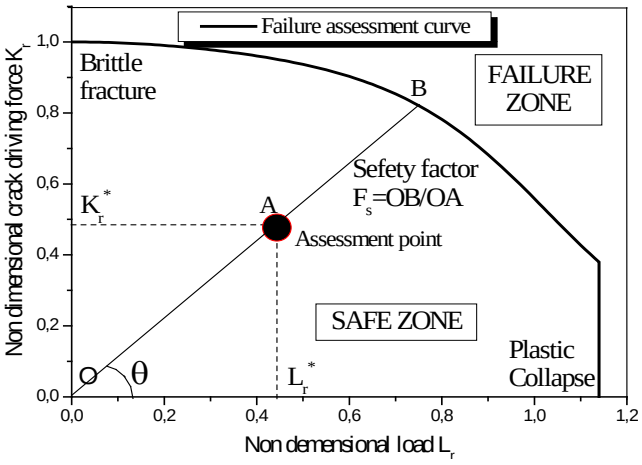

Figure III.35- Schematically presentation of the Failure Assessment Diagram.

Definitions of non dimensional crack driving force k_r and non dimensional applied stress S_r or load L_r. Non dimensional crack driving force k_r was initially defined as the ratio of applied stress intensity factor over the fracture toughness of material K^*_c.

$$k_r = \frac{K_{ap}}{K_c^*} \tag{7}$$

By extension, it can be defined from the J integral or crack opening displacement:

$$k_r = \sqrt{\frac{J_{app}}{J_{mat}}} \quad or \quad k_r = \sqrt{\frac{\delta_{app}}{\delta_c}} \tag{8}$$

where J_{app} and δ_{app} are the applied J integral and crack opening displacement and J_{mat} and R_c are fracture toughness expressed in terms of critical value of J Integral or critical crack opening displacement of the material. Non dimensional stress S_r is defined as ratio of the gross stress R_g over flow stress R_c (chosen as yield stress R_y, ultimate stress; R_m or classic flow stress $R_c=(R_y+R_m)/2$).

$$S_r = \frac{\sigma g}{R_c} \tag{9}$$

Non dimensional load L_r is defined as follow:

$$L_r = \frac{P}{P_L} \tag{10}$$

P is applied load and P_L limit load.

III.4. SIMULATION APPROACH AND NUMERICAL METHODS

In this analysis we consider a simple structure: a pipe submitted to internal pressure, this pipe is made from API 5L X52 steel. The pipe has a diameter D=611 mm and thickness t=11 mm. This pipe exhibits an internal semi-elliptical crack at pipeline with a/t=0.1, 0.2, 0.3, 0.4 and 0.5, with a/c=0.5 and pressure variation to the limit pressure P_L . Using ANSYS [29] software, after conversion of engineering stress/strain to True stress/strain of API 5L X52 pipeline steel with and without hydrogen. A SOLID186 element using in this finite element analysis with a 20 node solid element that exhibits quadratic displacement behavior. The element is defined by 20 nodes having three degrees of freedom per node: translations in the nodal x, y, and z directions. The element supports plasticity, hyper-elasticity, creep, stress stiffening, large deflection, and large strain capabilities. The SOLID186 has been adapted to meshing the pipe, with a refined meshing at the near of crack tip which represents the critical zone of the pipe (Fig.8(a) and (c)). The semi-elliptical crack characterised with crack depth ratio a/t and a/c=0.2 (fig.36(b)). A example of Von Mises stress distribution at the semi-elliptical crack tip showed in the Fig.36(d).

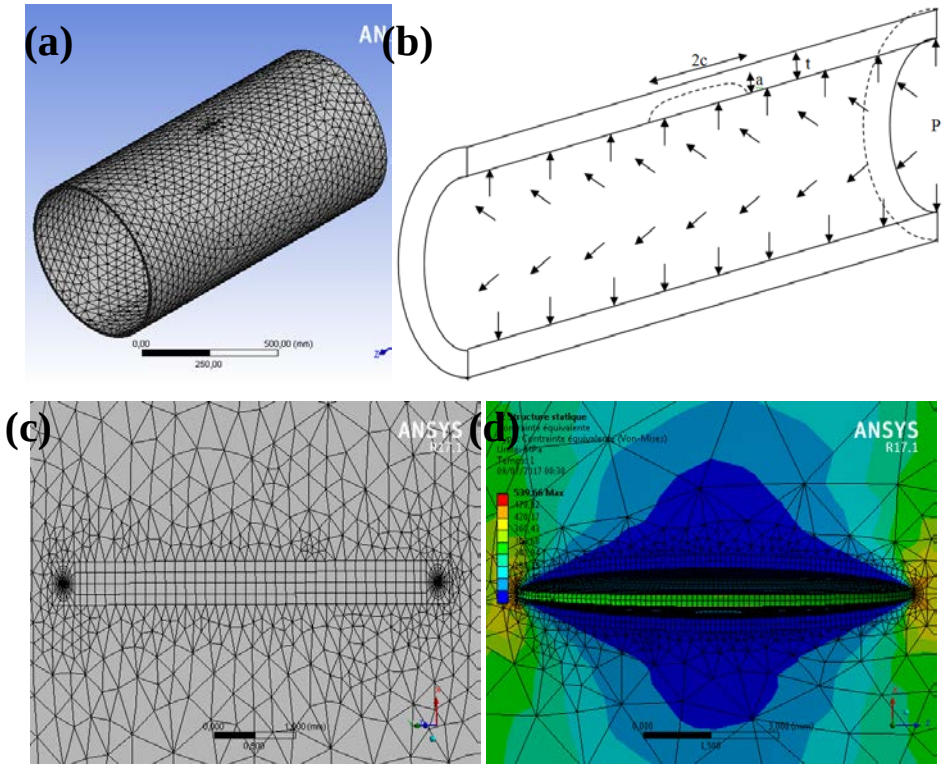

Figure III.36- Internal Semi-elliptical crack at pipeline presentation, (a) Pipeline geometry and mesh type, (b) Schematic diagram depicting the longitudinal section, (c) crack mashing and (d) Von Mises stress distribution at crack tip.

The Table 4 showing the failure pressure establish by different codes (ASME B31G [34], Modified B31G [35], DNV RP F-101 [36], SHELL-92 [37], RSTRENG [38], the Netto et al.[39] method and the Choi's [40]) with and without hydrogen effect. A maximum decreasing of the limit pressure with 4%, is observed since regardless of the decrease of the mechanical properties of 4% too (Table 7). The modified ASME B31G find a maximum values of the limit pressure compared with the other codes, in the other hand; the RSTRENG method have a conserved method.

Table III.7.- Limit pressure calculated by different methods and different crack depth values with and without hydrogen embrittlement for API X52 steel.

Depth ratio	Gas	B31G	$B31G_{mod}$	DNV RP F101	SHELL92	RSTRENG	Choi's	Netto method
0.1	NG	17.34	18.25	16.05	14.18	14.18	14.51	17.29
	H_2	16.66	17.63	15.43	13.63	13.63	13.95	16.62
0.2	Air	17.33	18.24	16.05	14.18	12.61	14.36	17.16
	H_2	16.66	17.63	15.42	13.63	12.12	13.80	16.50
0.3	Air	17.33	18.23	16.04	14.17	11.04	14.22	16.95
	H_2	16.65	17.62	15.42	13.62	10.61	13.67	16.29
0.4	Air	17.31	18.21	16.03	14.14	9.48	14.09	16.64
	H_2	16.63	17.60	15.41	13.59	9.11	13.54	16.00
0.5	Air	17.28	18.17	16.01	14.08	7.92	13.93	16.25
	H_2	16.60	17.56	15.38	13.54	7.62	13.38	15.62

The second part represent a numerical analysis of cracked pipeline, an internal semi-elliptical crack at pipeline with a/t=0.1, 0.2, 0.3, 0.4 and 0.5, with a/c=0.5 and pressure variation to the limit pressure P_L given by modified ASME B31G [35].

Figure 37 represent the stress intensity factor distribution for a semi-elliptical crack ratio a/t=0.5. The maximum stress intensity factor localized at the phi=90°. For an applied pressure P=17 MPa and for the natural gas pipeline, the stress intensity factor was less than 20% of the fracture toughness. In the other hand; the hydrogen pipeline case, the stress intensity factor was great than the fracture toughness (Fig.37 (a)). In figure37 (b) showing the stress intensity factor $K_{I,\phi=90}$ variation for different apply applied pressure values, we observed an increasing linearly to the pressure value P=14 MPa, after this value we observe a nonlinear increasing, this transformation caused by the plastic strain.

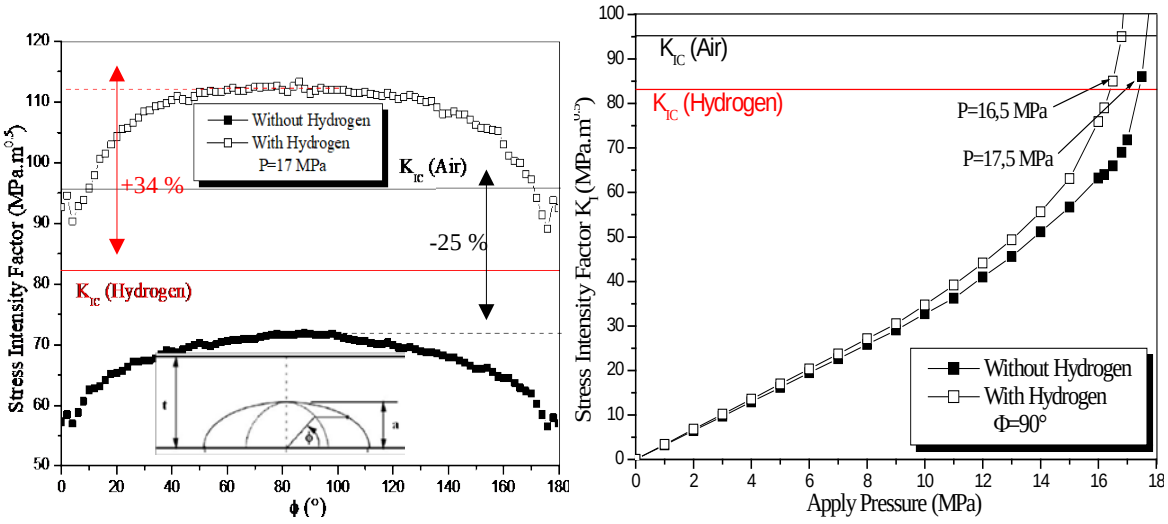

(a) (b)

Figure III.37- Stress intensity factor distribution for P=1MPa to 17 MPa and a/t=0.5 for a natural gas and hydrogen transportation (a) at crack tip and (b) at ϕ=90°.

The maximum stress intensity factor with and without hydrogen was presented at the figure 36(b), we observed an approximately of the maximum stress intensity factor value, with and without hydrogen for an apply pressure less than 14 MPa, however; the hydrogen case was increasing of stress intensity factor then 20%. The Figure 38 showed the two methods used to determine the failure pressure with the CDF and the FAD approaches. The two methods give the same result for a brittle material (Lr≈0).

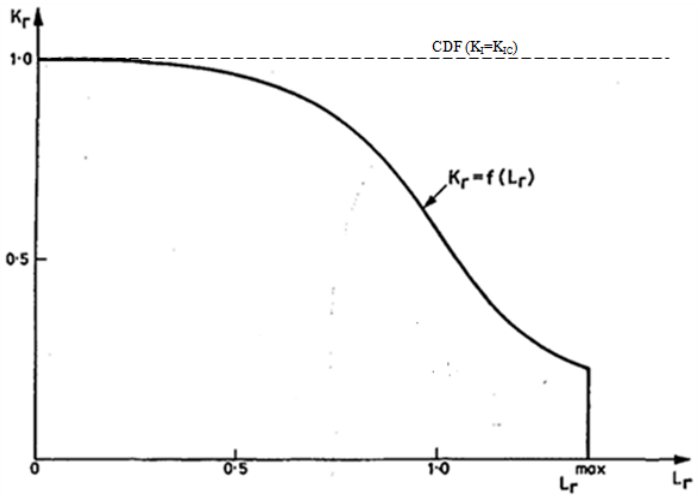

Fig.38 - Diagram representation of the two safety curves using in the FAD and the CDF approaches.

The figure 39 showed the FAD with and without hydrogen effect, for different applied pressure and for a/t=0.5.

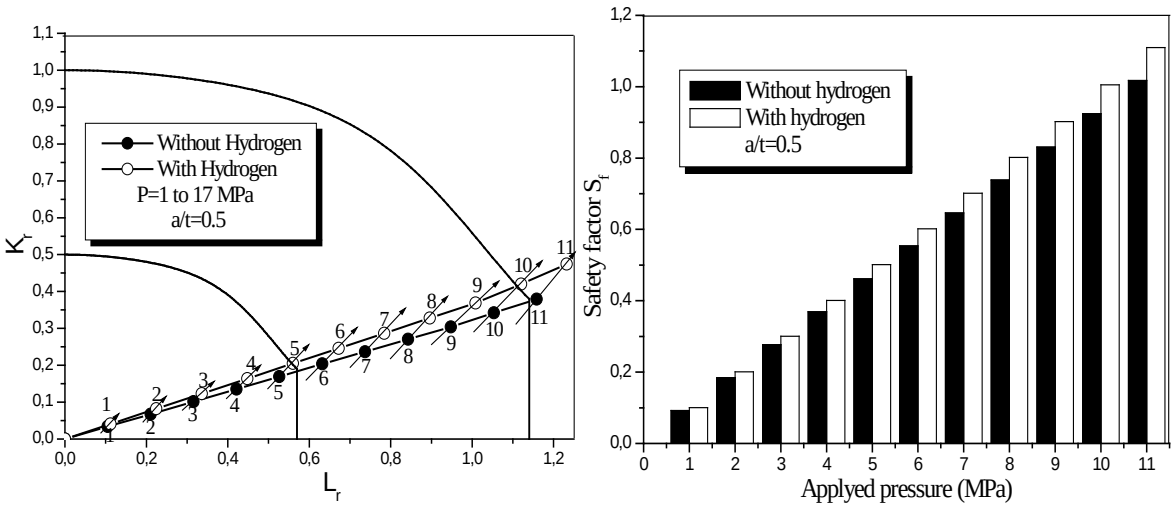

(a) (b)

Fig. 39 - FAD with and without hydrogen function as applied pressure and a/t=0.5, (a) Assessment points, (b) Safety factor.

By using the crack driving force (CDF) approach, the critical pressure supported P_c=16.13 MPa and P_c=17.64 MPa with and without hydrogen respectively. In the another hand; the FAD approach uses the comparison of the crack tip driving force with the material's fracture toughness and with the plastic load limit analysis at the same time.

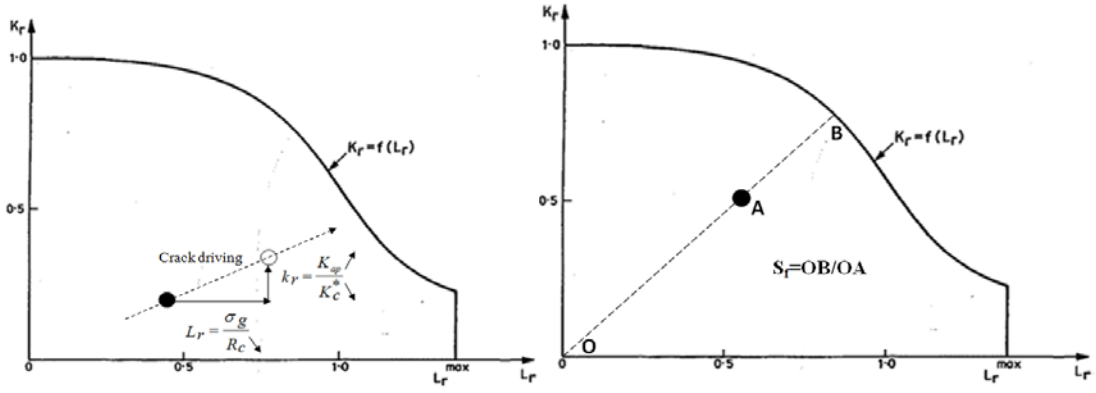

(a) (b)

Fig. 40 – Failure assessment diagram representation. (a) hydrogen embrittlement effect on the assessment point, (b) safety factor calculation method.

The critical pressure supported $P_c \approx 11$ MPa and $P_c \approx 10$ MPa with and without hydrogen respectively. However; the hydrogen effect presented by the increasing of the non dimensional loading parameter (L_r) and the crack tip driving force (K_r), because the increasing of the applied stress intensity factor (K_I) and the flow stress (σ_g), in the same time because de decreasing of and the middle stress ($R_c=(\sigma_y+\sigma_u)/2$) (Figure 40).

These results demonstrate that of hydrogen embrittlement of the pipeline has a slight effect on the safety of pipeline. The results were complete at the Table 5, for different depth ratios compared with the failure pressure calculate by the modified ASME B31G.

Table III. 8 - Limit pressure comparisons for different methods: ASME $B31G_{mod}$, Crack driving force (CDF) and failure assessment diagram (FAD) and for different crack depth ratio with and without hydrogen.

	Methods	$B31G_{mod}$		CDF		FAD	
Depth ratio	Pressure	P_L	Diff.(%)	P_L	Diff.(%)	P_L	Diff.(%)
0,1	Air	18.25	3,40	21.52	10,34	19.23	3,80
	H_2	17.63		19.23		18.5	
0,2	Air	18.24	3,34	19.88	3,77	17.1	6,96
	H_2	17.63		18.93		15.91	
0,3	Air	18.23	3,35	18.62	0,42	14.93	8,10
	H_2	17.62		18.54		13.72	
0,4	Air	18.21	3,35	17.83	1,79	12.85	8,87
	H_2	17.6		17.51		11.71	
0,5	Air	18.17	3,36	17.64	8.56	10.79	8,15
	H_2	17.56		16.13		9.91	

A small decreasing of the failure pressure has been noted (4%) in the table 8. These results were proved the possibility of hydrogen transportation using the natural gas pipeline. The next figure represent the failure assessment diagram for different depth ration (a/t=0.1, 0.2, 0.3, 0.4 and 0.5) and different applied pressure values (P=5 and 11 MPa).

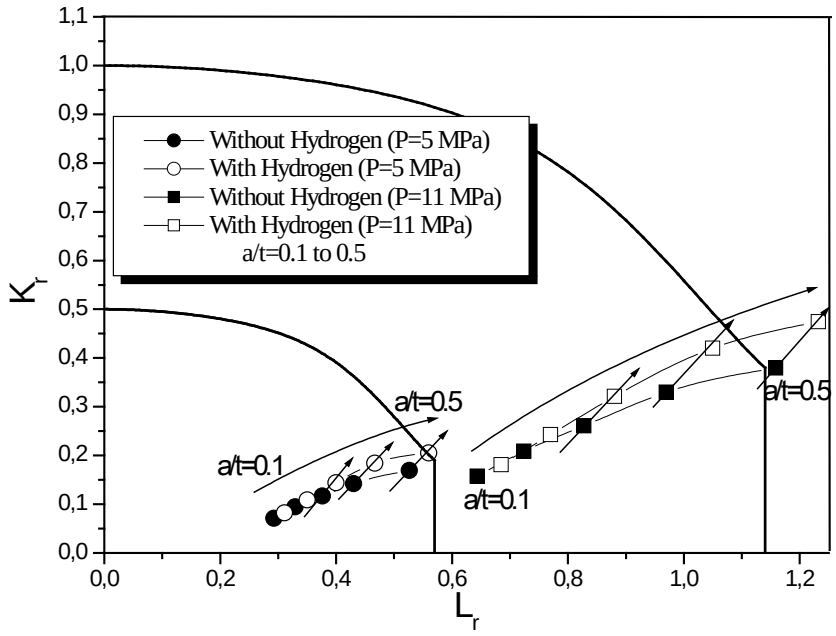

Fig. 41 - Failure assessment diagram for different crack depth and applied pressure P=5 and 11 MPa.

The result showing that; there is a significance transition of the assessment points, of the inside to the outside of the safety zone, this changing because the semi-elliptical crack depth increasing. We observed an important effect of hydrogen embrittlement for a/t=0.3 to 0.5.

In the table 9 and the figure 42 represent the safety factor (S_f) values comparisons for different crack depths ratio, with and without hydrogen and for different pressures. The safety factor (S_f) calculation method is presented in the fig 40(b).

Table III.9.- Safety factor (S_f) values comparisons for different crack depths ratio (a/t=0.1 to 0.5), with and without hydrogen and for different pressures (P=5 MPa and 11 MPa).

S_f	P=5 MPa			P=11 MPa		
a/t	Without H_2	With H_2	Diff. (%)	Without H_2	With H_2	Diff. (%)
0.1	0.26	0.27	3.85	0.56	0.60	7.14
0.2	0.29	0.31	6.90	0.64	0.68	6.25
0.3	0.33	0.36	9.09	0.73	0.79	8.22
0.4	0.38	0.43	13.16	0.85	0.96	12.94
0.5	0.46	0.50	8.70	1.02	1.12	9.80

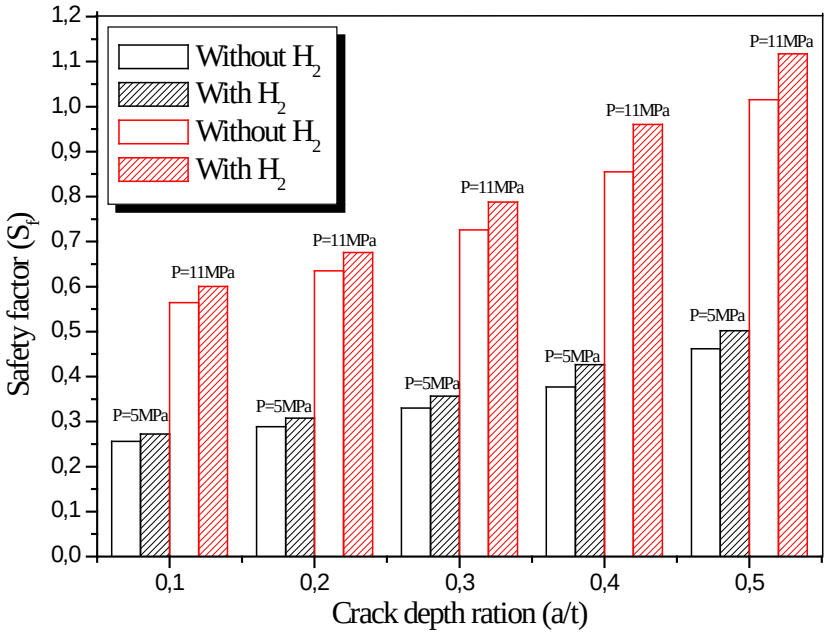

Fig. 42 - Safety factor (S_f) values comparisons for different crack depths ratio (a/t=0.1 to 0.5), with and without hydrogen and for different applied pressures (P=5 and 11 MPa).

In the figure 42 the maximum difference compared with the safety factor is 13.16 and 12.94 for P=5MPa and P =11 MPa respectivelly and for a/t=0.4. the results proved the possibility of hydrogen transportation using the natural gas pipeline using API X52 steel.

The aim of this paper is to verify the possibility of hydrogen transportation using the natural gas pipeline, taking into account the hydrogen embrittlement effect on the failure pressure. The result proved that the decreasing of yield stress at 4% due of the hydrogen embrittlement (168 hours) have decreasing of the limit pressure with 4% too in the modified ASME B31G. In other hind; the CDF and FAD gives a limit pressure decreasing of >10%. These results conclude that the hydrogen transportation using the natural gas pipeline is possible if we use a design factor f_F < 0.72 (for the natural gas transportation f_F=0.72). The hydrogen effect has an decreasing of the pressure by 3.4 %, as the safety factor of f_F=0.69 is purpose for the hydrogen transportation the natural gas pipeline using API 5L X52 steel.

III.5.Conventional Blade Repair

There are a number of challenges that are faced when inspection of turbine blades is carried out before it can be repaired:

- Turbine blades are rather expensive samples with complex inner cooling structures.
- High inspection accuracy: both the freeform aerofoil surface of blades as well as specific features require accurate verification. In addition, internal walls thickness is subject to tight geometric deviations.
- Dense material: inspection of dense material requires powerful x-ray source that allows x-rays to travel through the blade.
- X-ray scattering: the inspection of dense materials potentially leads to x-ray scattering, which may cause inferior image quality.
- Fast inspection: turbine blades are inspected at different stages in the prototyping and production process: after concluding moulding and specific machining and finishing steps.
- Fast CT reconstruction: in a production environment, it is important to quickly obtain inspection results.
- Larger specimens: turbine blades are somewhat larger in size and require an inspection cabinet that offers sufficiently space.

Traditionally, turbine blades or film radiography are verified through touch sensors based on Coordinate Measuring Machines [25].

III.5.1Coupon Repair

Sometimes, vanes experience damage in service that requires restoration of the airfoil leading edge. When this happens, the most effective way to restore the area is by physically removing the damaged section and replacing it with a pre-manufactured leading edge section, otherwise referred to as a “coupon” [23].

The leading edge coupon repair technique is used to replace severely burned, eroded, or impacted leading edges of vanes that would otherwise be scrapped or require lengthy repairs. The basic concept is to produce a portion of the leading edge airfoil identical to the original airfoil, remove the damaged area of the airfoil from the vane segment, and join the new portion to the original vane segment.

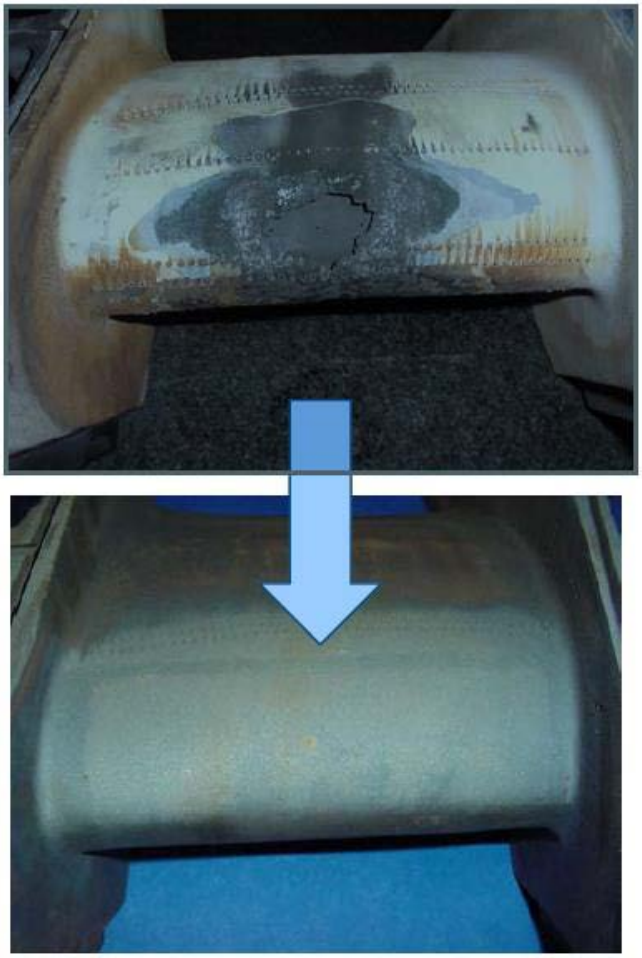

Figure III. 43: Turbine vane leading edge, before and after coupon repair [26]

III.5.2.Penetrant Testing [27]

The blade is pre-cleaned following which penetrant solution is applied to the surface of the component. The liquid is pulled into the surface breaking defects by capillary action. Excess penetrant material is carefully cleaned from the surface. A developer is applied to pull the trapped penetrant back to the surface where it is spread out and forms an indication. This indication is relatively easier to spot and gives an account of where the defect has occurred (Figure III.44) [28].

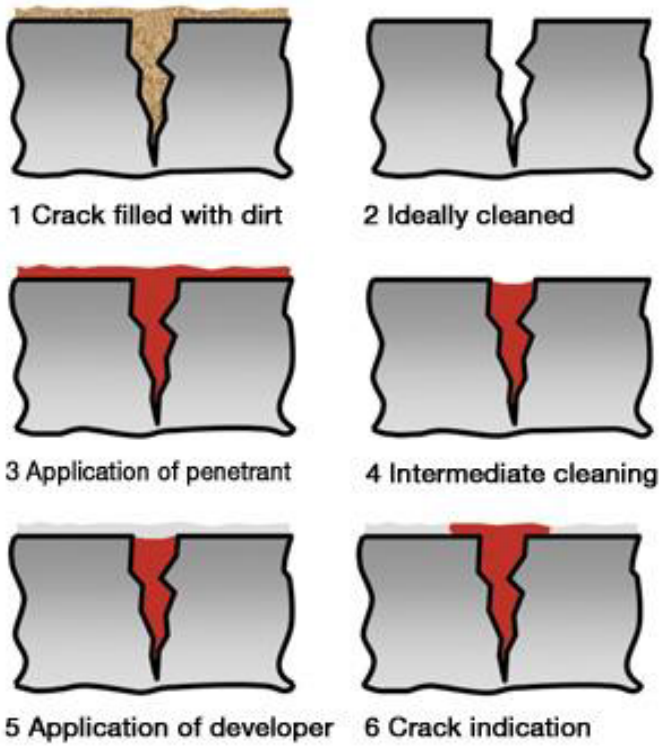

Figure III.44: Penetrant testing steps

III.5.3.Braze restoration of Cracks

Brazing in general is used for the repair of hot gas path components. It involves the use of materials with a lower melting point than the base metal to be repaired, frequently mixed in various ratios with powders close to base material composition. The brazing process offers a number of major potential benefits, compared to the more commonly used weld repair processes. The uniform heating of the whole part can lead to a reduced risk of dimensional deviation. The braze process features a high repeatability rate. The access to the area to be repaired is not limited and the throughput is only limited by the furnace size. Moreover, a rejuvenation heat treatment of the base material can be incorporated into the brazing heat treatment. Brazing can be employed for the repair of nickel as well as Cobalt-based alloys [26].

There are two types of brazing

1. Overlay brazing- for surface restoration
2. Narrow gap brazing - to restore small thermal fatigue cracks.

The narrow gap brazing process itself is performed similarly to the overlay brazing process. While in the latter a sluggish braze–base material mixture is preferred, the narrow gap brazing

process relies on the presence of a liquid mixture that gives the opportunity for the capillary forces to fill the cavity (Figure III.45).

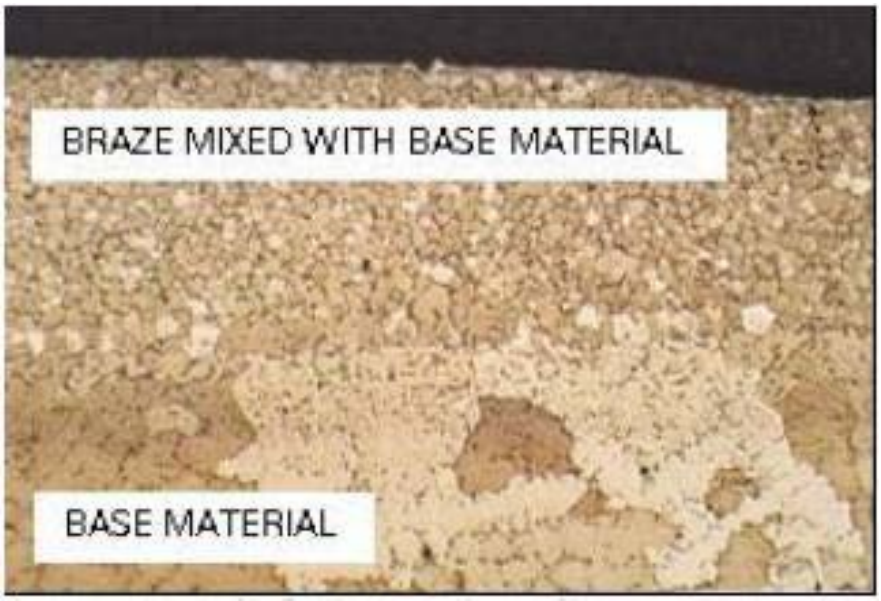

Figure III.45: Overlay brazed Nickel-based Alloy

III.5.4.Similarities between vane and blade repair technology

The latest methods of blade repair are now being transferred for vane repair also as the latest vanes are largely being built in the same material as the turbine blades which are the nickel based alloys since they are also influenced by high thermal stress. Both blades and vanes share the same methods of repair in elevated temperature welding and braze repair.

Reference

[1] Bunsch, A., J. Kowalska, and M. Witkowska. "Influence of die forging parameters on the microstructure and phase composition of Inconel 718 alloy." Archives of Metallurgy and Materials 57 (2012): 929-935. DOI: 10.2478/v10172-012-0102-8

[2] S.A. Moshizi , A. Madadi, M.J. Kermani.” Comparison of inviscid and viscous transonic flow field in VKI gas turbine blade cascade”, Alexandria Engineering Journal (2014) 53, 275–280. doi.org/10.1016/j.aej.2014.03.007

[3] Wang Pei1, Du Qiang, Yang Xiao Jie1, Zhu Jun Qiang.” Heat Transfer and Aerodynamics of Complex Shroud Leakage Flows in a Low-Pressure Turbine”, Article ID: 1003-2169(2013)05-0447-12, Journal of Thermal Science Vol.22, No.5 (2013) 447 458

[4] HivaRashidzadeh, Seyed Mostafa Hossein alipour, and Alireza Mohammad zadeh.” The SGT-600 industrial twin-shaft gas turbine modeling for mechanical drive applications at the steady state conditions”, DOI 10.1007/s12206-015-0946-8, ww.springerlink.com/content/1738-494x(Print)/1976-3824(Online)

[5] American Petroleum Institute,” General-Purpose Steam Turbines for Petroleum, Chemical, and Gas Industry Services”API standard 611 fourth edition,USA june 1997.

[6] Rolls-Royce plc 1986 Fifth edition Reprinted 1996 with revisions, ISBN 0902121 235.

[7] V. G. Rybalkoand al (Analysis of the Causes of Fracture of Turbine Blades in a Gas Compressor) Unit Russian Academy of Sciences 2014 .doi.org/10.1134/S0036029515100146

[8] Jack A .Heller, Rose L. Whitney, and Richard H. Cavicchi “experimental investigation of a conservatively designed turbine at f our rotor-blade solidities”, NACA RM EM52C17, July - 17, 1952, Declassified February 15, 1957.

http://naca.central.cranfield.ac.uk/reports/1952/naca-rm-e52c17.pdf

[9] Westergaard H M (1934): Stresses at a crack, size of the crack and the bending of reinforced concrete, Proc. American Concrete Institute, 30, 93-102 .doi.org/10.1007/1-4020-3153-X_2

[10] université de batna, faculté de technologie, département de mécanique, mémoireprésenté pour l’obtention du diplôme de magistèreenmécanique,option : science des matériaux,parklaaeftikhar, « Conception d’uneaube de turbine à gazenmatériaux composites », Soutenu le : 14/ 09/ 2015.

[11] Toshio, Nakamura, and David M. Parks. "Determination of elastic T-stress along three-dimensional crack fronts using an interaction integral." International journal of solids and structures 29.13 (1992): 1597-1611.

[12] Mohamed HadjMeliani et al, Two Parameter Engineering Fracture Mechanics: Calculation of the Relevant Parameters and Investigation of Their Influence on the Surface Notch,book: integrity of pipelines tnsporting hydrocarbons, ISBN 978-94-007-0594-4 (PB),ISBN 978-94-007-0587-6 (HB),ISBN 978-94-007-0588-3 (e-book),DOI 10.1007/978-94-007-0588-3.

[13] V. G. Rybalko and al (Analysis of the Causes of Fracture of Turbine Blades in a Gas Compressor) Unit Russian Academy of Sciences 2014 doi.org/10.1134/S0036029515100146

[14] Alexander Staroselsky (Chapter Two Damage and cracking morphology) United Technologies Research Center, USA 2005 doi: 10.2495/1-85312-836-8/02

[15] http://www.energy.siemens.com/us/pool/hq/power-generation/steam turbines/downloads/Big%20SST_overview.pdf Consulted in 26/01/2020

[16] M. Hadj Meliani, Z. Azari, Yu. G. Matvienko, G. Pluvinage 'The Effect of Hydrogen on the Master Failure Curve of APL 5L Gas Pipe Steels' Procedia Engineering 10 (2011) 942–947, doi:10.1016/j.proeng.2011.04.155.

[17] Elazzizi A, et al., The master failure curve of pipe steels and crack paths in connection with hydrogen embrittlement, International Journal of Hydrogen Energy (2015). doi.org/10.1016/j.ijhydene.2014.12.040

[18] G. Razzini, M. Cabrini, S. Maffi, G. Mussati, B.L. Peraldo, Effect of the heat-affected zones on hydrogen permeation and embrittlement of low-carbon steels, Materials Science Forum 289-292 (1998) 1257-1266. doi.org/10.4028/www.scientific.net/MSF.289-292.1257

[19] Cheolho Park, Namhyun Kang, Stephen Liu. 'Effect of grain size on the resistance to hydrogen embrittlement of API 2W Grade 60 steels using in situ slow-strain-rate testing' Corrosion Science (2017), http://dx.doi.org/10.1016/j.corsci.2017.08.032.

[20] R. Capriotti, M. Colavita, F. De Paolis, P. Silvestri. 'Hydrogen Embrittlment Detection on High-Strength Steel by Means of XRD Residual Stress Determination Technique' http://www.ndt.net/article/wcndt00/papers/idn017/idn017.htm

[21] BELLAHCENE Tassadit. 'Etude de la nocivite de defauts dans les canalisations sous environnement hydrogene' Doctoral Thesis, Mouloud Mammeri university of Tizi-Ouzo-Algeria, 2015.

[22] Mehdi Javidi, Arash Ghassemi & Mohammad Mehdi Lalehparvar. 'Amine corrosion and amine cracking of API 5L X52 carbon steel in the presence of hydrogen sulphide and carbon dioxide' Corrosion Engineering, Science and Technology, The International Journal of Corrosion Processes and Corrosion Control, 2017.

[23] A. Ya. Krasovs'kyi, O. E. Gopkalo, I. O. Makovets'ka, and O. O. Yanko." A study of the causes of the service fractureof turbine rotor blade of compressor station gas-turbine unit ",UDC 539.4, Strength of Materials, Vol. 45, No. 4, July, 2013

[24] M. Hadj Meliani, O. Bouledroua, A. Alhussein, Y.G. Matvienko, G. Pluvinage. 'Some Aspects Sandblasting and Hydrogen on The Material Master Failure Curve in Engineering Fracture Mechanics' Anales de Mecánica de la Fractura (Vol. 32), 2015.G. V. D. D. R. A. A. B. Julie McGraw, "Advancements in gas turbine vane repair," in PWR2006, Atlanta, 2006.

[25] CHARLES, Amal Prashanth et GONZALEZ TAYLOR, Claudio Alexander. Development of amethod to repairgas turbine bladesusingelectronbeammelting additive manufacturingtechnology. 2017.

[26] D. S. C. SisirSagar, "Case Study on Advanced Manufacturing and Quality Control of Compressor Blades," International Journal of Emerging Technology and Advanced Engineering, vol. 4, no. 10, pp. 444-448, 2014.

[27] Karl Deutsch, "Karl Deutsch," [Online]. Available: http://www.karldeutsch.de/KD_GENERAL_KnowledgeBase_PT_EN_M1.html.

[28] D. S. C. Sisir Sagar, "Case Study on Advanced Manufacturing and Quality Control of Compressor Blades," International Journal of Emerging Technology and Advanced Engineering, vol. 4, no. 10, pp. 444-448, 2014.

[29] Capelle, J., Gilgert, J., Dmytrakh, I., Pluvinage, G., Sensitivity of pipelines with steel API X52 to hydrogen embrittlement, International Journal of Hydrogen Energy, 33, Issue 24, (2008), 7630-7641

[30] Hadj Meliani M, Matvienko YuG, Pluvinage G. Corrosion defect assessment on pipes using limit analysis and notch fracture mechanics. Engng Failure Analysis 2011; 18: 271-283.

[31] Firooz Tabkhi . 'Optimisation de Réseaux de Transport de Gaz', Doctoral Thesis, National Polytechnique De Toulouse, 2007

[32] E. Shashi Menon. 'Transmission Pipeline Calculations and Simulations Manual', Libarty of Congress Cataloging in Publication Data, Elservier, ISBN: 978-1-85617-830-3.

[33] Nenad Gubeljak, Jožef Predan. 'Procedures for Structure Integrity Assessment', Security and Reliability of Damaged Structures and Defective Materials, Cooperation With Nato Public Diplomacy Division, Springer, 2009.

[34] American National Standard Institute (ANSI)/American Society of Mechanical Engineers (ASME). Manual for determining strength of corroded pipelines, ASME B31G; 1984.

[35] ASME B31G-2009: Manual for Determining the Remaining Strength of Corroded Pipelines[S]. American Society of Mechanical Engineers, New York (2009)

[36] DNV RP-F101 (2) DNV-RP-F101: Corroded pipelines. Det Norske Veritas; 1999.

[37] A. C. Reddy, Reliability assessment of corrosion cracks in cold rolled 302 stainless steel pipes based on SHELL-92 criterion, National Conference on Advances in Design Approaches and Production Technologies (ADAPT-2005), Hyderabad, 22-23rd August 2005, 232-234.

[38] A. C. Reddy, Trustworthiness judgment of corrosion cracks in cold rolled 305 stainless steel pipes based on RSTRENG criterion, National Conference on Advances in Design Approaches and Production Technologies (ADAPT-2005), Hyderabad, 22-23rd August 2005.

[39] Netto TA, Ferraz US, Estefen SF. The effect of corrosion defects on the burst pressure of pipelines. J Constr Steel Res 2005;61: 1185–204.

[40] Choi JB, Goo BK, Kim JC, Kim YJ, Kim WS. Development of limit load solutions for corroded gas pipelines. Int J Pres Ves Piping 2003;80(2):121–8.

Conclusions and perspectives

Conclusions and perspectives

The importance of gas turbine in the world is due to maintain and continue the economy and international service. As any material, blades of gas turbine occurred to different failures such as pitting corrosion. In this thesis, numerical analyses were investigated to the influence of semi-elliptical cracks in order to predict the propagation of crack path. Due to the complexity and difficulty of CFD simulation with fracture mechanics, we separated the two domains. Firstly, CFD models were examined in the Fluent to obtain the pressure distribution using Navier-Stokes equations. In the other part, the results which obtained from CFD were imported to APDL software to examine the fracture domain of semi-elliptical cracks. At the end of the thesis, this part addresses an overview of this study aiming to provide a general conclusion and prospects.

From the results and other discussion of preceding chapters, the following conclusion can be made

1. Blades may be considered to be the heart of turbine. Without blades there would be no power and the slightest fault in blading would mean a reduction in efficiency and costly repairs. In the gas turbine the transformation of energy reborn from the impacts of the exhausts gases with the blades that's rotate the wheel of turbine that provide a driving power for the shaft that turn with them the compressor . The Air is compressed and the pressure and temperature will rise. In each single turbine section there are blades holded by a disk or hub, and this last are connected with compressor with a shaft to determine the stage in gas turbine we must know the two types of blades one fixed and the other mobile. And the number of stages has effects on the blade structure and design. Turbine blades are the parts which undergo the most damaging solicitations. Because they are subjected to high temperature, high pressure and centrifugal forces that's make the defects grow rapidly and taking into account the hydrogen embrittlement effect on the failure pressure.
2. In our study, FEM (ANSYS®) was used to estimate the effect of pre-crack path on blade gas turbine with coupling between fluid and structure analysis. In the stress analysis for structural model, the pressure have obtained from the CFD analysis. In the second step, crack was created and the SIF and equivalent SIF value were analyzed, plotted and compared to theory of westergard solutions. The most stress intensity factor was dominated on the opening mode (KI) along of the contour for

different angle on the semi elliptical crack. T-stress was calculate on the aim to estimate the crack path by the way to compare the different values. The second parameter on the Williams equation give more information's along of the ligament and for different orientation on the contour to estimate the crack path and the failure by computing of the equivalent stress intensity factor.

3. The experimental and numerical analysis of hydrogen embrittlement on pipeline steel were presented instead the blade material made of Inconel 718 ALLOY. As mentioned before, this material is not available in Algerian industry – hence- API X52 pipeline steel replaced instead it. The analysis are used to verify the possibility of hydrogen transportation using the natural gas pipeline, taking into account the hydrogen embrittlement effect on the failure pressure. The result proved that the decreasing of yield stress at 4% due of the hydrogen embrittlement (168 hours) have decreasing of the limit pressure with 4% too in the modified ASME B31G. In other hind; the CDF and FAD gives a limit pressure decreasing of >10%. These results conclude that the hydrogen transportation using the natural gas pipeline is possible if we use a design factor $f_F < 0.72$ (for the natural gas transportation $f_F=0.72$). The hydrogen effect has an decreasing of the pressure by 3.4 %, as the safety factor of $f_F=0.69$ is purpose for the hydrogen transportation the natural gas pipeline using API 5L X52 steel.

Finally, the blade maintenance and repair methods are the only remaining step to complete this project due to the absence and difficulties of experimental tests. In order to resolve this, a general overview has been performed on the conventional Blade Repair in the end of this thesis